

120
A FINITE ELEMENT METHOD SOLUTION
FOR FLUID FLOW IN JOINTED ROCK

BY

Shun-Lung Su

B.S. Chun-Yuan University

Taiwan R.O.C.

A MASTER'S THESIS

submitted in partial fulfillment of the

requirement for the degree

MASTER OF SCIENCE

Department of Mechanical Engineering

KANSAS STATE UNIVERSITY

Manhattan, Kansas

1988

APPROVED BY:

Daniel Siverson

TABLE OF CONTENTS

List of Figures	iii
Acknowledgements.	Vii

CHAPTER

1.0 INTRODUCTION	1
1.1 - Hot Dry Rock concept.	1
1.2 - Recent developments in the HDR program	1
1.3 - Previous work	3
1.4 - Objectives	5
2.0 FLUID-FLOW NETWORK MODEL	9
2.1 - Derivation of flow model	9
2.2 - One-Dimensional finite element model.	14
2.2.1 The differential fluid element.	14
2.2.2 Quadratic one-D element formulation	15
2.2.3 Galerkin's method	16
2.3 - One-Dimensional tracer model	19
3.0 DESCRIPTION OF FLUCRK	26
3.1 - User interaction	26
3.1.1 Automated mesh generation	26
3.1.2 Interactive problem specification	26
3.2 - Connection between structure Elements and fluid Elements.	28
3.3 - Active/nonactive element	29

LIST OF FIGURES

1.1	Schematic drawing of Phase II Reservoir	7
1.2	Schematic drawing of HDR Reservoir simulation	8
2.1	Fluid flow between two parallel plates	23
2.2	One-Dimensional Quadratic element	23
2.3	Differential fluid element	24
2.4	Differential tracer element	24
2.5	Example of tracer mixing at a joint	25
3.1	Flow chart of FLUCRK	34
3.2	Flow chart of DR	35
3.3	Connection between structure element and fluid element.	36
4.1	Verification problem one	41
4.2	Flowrate of input element (problem one)	42
4.3	Flowrate of output element (problem one).	42
4.4(a)	Tracer at input node (problem one)	43
4.4(b)	Tracer at middle of crack (problem one).	43
4.4(c)	Tracer at output node (problem one)	44
4.5	Flowrate of input element (problem two).	44
4.6	Flowrate of output element (problem two)	45
4.7(a)	Pressure at middle of crack (problem two).	45
4.7(b)	Flowrate at middle of crack (problem two).	46
4.8(a)	Tracer at input node (problem two)	46
4.8(b)	Tracer at middle of crack (problem two).	47
4.8(c)	Tracer at output node (problem two).	47
4.9	Verification problem three	48

4.10	Flowrate of input element (problem three).	49
4.11	Flowrate of output element (problem three)	49
4.12(a)	Pressure at middle of crack (problem three)	50
4.12(b)	Flowrate at middle of crack (problem three)	50
4.12(c)	Velocity at middle of crack (problem three)	51
4.13(a)	Tracer at input node (problem three).	51
4.13(b)	Tracer at middle of crack (problem three)	52
4.13(c)	Tracer at output node (problem three)	52
4.14	Pressure plot of problem three.	53
4.15	Tracer plot of problem three	53
4.16	Verification problem four	54
4.17	Far field boundary condition.	55
4.18	Flowrate at left end of fluid element	55
4.19	Flowrate at right end of fluid element.	56
4.20(a)	Pressure at left end (problem four)	56
4.20(b)	Pressure at input node (problem four)	57
4.20(c)	Pressure at right end (problem four).	57
5.1	Mesh plot of application problem one.	64
5.2(a)	Material property of material type one.	65
5.2(b)	Material property of material type two.	65
5.3(a)	Flowrate at input node.	66
5.3(b)	Flowrate at output node	66
5.4	The pressure of a far field node No.30	67
5.5	Kinetic Energy vs No of Iteration plot	67
5.6	Pressure plot of application problem one.	68

5.7	Flowrate plot of application problem one.	68
5.8	Far field condition of application problem two.	69
5.9(a)	The input flowrate of application problem two	70
5.9(b)	The output flowrate of application problem two.	70
5.10(a)	The pressure at a far field node No.30	71
5.10(b)	The flowrate at a far field node No.30	71
5.11	Kinetic Energy vs No of Iteration plot	72
5.12	Pressure plot of application problem two.	73
5.13	Flowrate plot of application problem two.	73
5.14	Far field condition of application problem three.	74
5.15(a)	Flowrate at input node (problem three).	75
5.15(b)	Flowrate at output node (problem three)	75
5.16	Pressure at a far field node No.30 which has no flow leakage	76
5.17(a)	Tracer at input node (problem three).	76
5.17(b)	Tracer at middle of crack (problem three)	77
5.17(c)	Tracer at output node (problem three)	77
5.18	Kinetic Energy vs No of Iteration plot	78
5.19	Pressure plot of application problem three.	79
5.20	Flowrate plot of application problem three.	79
5.21	Velocity plot of application problem three.	80
5.22(a)	Tracer plot at 4×10^4 seconds	80
5.22(b)	Tracer plot at 9×10^4 seconds	81
5.22(c)	Tracer plot at 1.5×10^5 seconds	81
5.23	Material property of material type three	82

5.24(a)	Input flowrate of application problem four.	83
5.24(b)	Output flowrate of application problem four	83
5.25(a)	Tracer at input node (problem four)	84
5.25(b)	Tracer at middle of crack (problem four).	84
5.25(c)	Tracer at output node (problem four).	85
5.26	Kinetic energy vs No of Iteration plot	85
5.27	Pressure plot of application problem four	86
5.28	Flowrate plot of application problem four	86
5.29	Velocity plot of application problem four	87
5.30(a)	Tracer plot at 1×10^4 seconds	87
5.30(b)	Tracer plot at 4×10^4 seconds	88
5.30(c)	Tracer plot at 6×10^5 seconds	88
5.31	Application problem five.	89
5.32(a)	Material property of material type one.	90
5.32(b)	Material property of material type two.	90
5.33(a)	Flowrate at input node of application problem five. .	91
5.33(b)	Flowrate at output node of application problem five .	91
5.34(a)	Pressure plot at 4×10^4 seconds.	92
5.34(b)	Flowrate plot at 4×10^4 seconds.	92
5.35(a)	Pressure plot at 6×10^5 seconds.	93
5.35(b)	Flowrate plot at 6×10^5 seconds.	93
5.36(a)	Pressure plot at 1.2×10^7 seconds.	94
5.36(b)	Flowrate plot at 1.2×10^7 seconds.	94

ACKNOWLEDGEMENTS

I wish to express my deep felt gratitude to my major professor Dr. Daniel V. Swenson, for suggesting this area of research, and for his advice and encouragement. His untiring help, patience, and understanding are appreciated. His intensive attitude for research not only encouraged me to accomplish this work, but also showed me the great spirit of devotion in engineering area.

Appreciation is extended to members of the supervisory committee, Dr. C. L. Huang and Dr. Robert L. Gorton. I am grateful for their support. I am also thankful to the Department of Mechanical Engineering for the creative enviroment which I learned and enjoyed a lot during these years of study.

To my parents, brother and sisters for their love and moral support, how thankful I am.

Partial funding for this project was given by NSF grant EET - 8708823, George K. Lea program official.

CHAPTER I

INTRODUCTION

1.1 Hot Dry Rock Concept

Increased demand for versatile energy supplies after the energy crisis has led to a corresponding interest in geothermal energy. The source is located within the earth's crust and methods used for the production can be considered geothermal extraction.

In conventional geothermal systems the convecting medium for extracting the available thermal energy to surface conversion facilities is the in-situ geothermal fluid (Palen and Narasimhan, 1981). Thus conventional systems depend on the location of geothermal fluid reservoirs. Unfortunately, they only represent a small fraction of geothermal energy in this world.

The Hot Dry Rock (HDR) concept does not require the presence of an in-situ fluid reservoir but is dependent only on the presence of a high geothermal gradient and an adequate supply of a working fluid, such as water. It is based on closed-loop circulation of pressurized water through a man-made fracture system, created by hydraulically fracturing hot rock between two wellbores. The useful heat from superheated water is recovered at the surface through heat exchangers, and the cooled water is reinjected to recirculate through the underground loop (Los Alamos annual report, 1984).

1.2 Recent Development In HDR Program

The Hot Dry Rock concept originated at Los Alamos National Laboratory in 1970. The major project effort during the past several

years has been to develop a commercial size underground reservoir by hydraulic fracturing. The program is now largely centered on the Fenton Hill Project near Los Alamos. The site is located on an extinct volcano in the Jemez Mountains of northern New Mexico, USA. The Phase II engineering system in Fenton Hill has a pair of wells. EE-2 is the injection well and EE-3 is the production well of the system (Los Alamos annual report, 1984). Figure 1.1 shows a schematic drawing of the reservoir.

From December 6 to 9, 1983, a total of $21,300 \text{ m}^3$ water was injected into EE-2 in 61 hours. This experiment was terminated by fatigue failure of hardware equipment. The resulting rapid vent returned to the surface about 54% of the water that had been injected and delivered thermal energy to the surface at rates estimated from 100 MW initially to an average of 30 MW over the 3.3 day period of rapid venting. The volume and rate of fluid return indicated that the fracture system was tightly contained and well connected; the high rate of energy production indicated the heat was extracted effectively from the fractured reservoir rock back through well EE-2 (Franke and Nunz, 1985). Despite the disappointment of hardware failures preventing satisfactory connection between two wellbores, the result at least indicated that a thermal reservoir extensive enough to be commercially useful had been opened.

During May and June 1986, a one month flow test of this Phase II heat extraction loop was conducted. A total of 37854 m^3 (10 million gallons) of water at 20°C was injected into an 243.8 m (800 feet) long section at depths around 3657.6 m (12,000 feet), where the

initial rock temperature was about 240 °C. Under a pumping pressure $2.76 \times 10^7 \text{ N/m}^2$ (4000 psi), the injection rate was $0.0179 \text{ m}^3/\text{sec}$ (285 gpm). The rate of fluid flow from the production well increased with time to $0.0148 \text{ m}^3/\text{sec}$ (235 gpm). The temperature of the produced water rose to 190 °C. The rate of heat production could be converted to about 1500 to 2000 KW of electrical power. The rate of water loss was initially very high, in part because of leakage through damaged casing in the production well, but it decreased with time to a final value of 26%. Much of this "loss" was water stored temporarily in fractures that were outside of the circulation paths and a large fraction of it was recovered later when the system was vented (Los Alamos annual report, 1985).

In December, 1987, experiment No. 2074 lasted eight days. The pumping pressure was $2.2 \times 10^7 \text{ N/m}^2$ (3200 psi) and the outlet pressure was $1.7 \times 10^6 \text{ N/m}^2$ (250 psi). The input flowrate was 96 gpm and the output flowrate rose from 0 gpm at the start to 60 gpm at the end of the test. The input flow loss is believed to be due to far field leakage and storage of the fluid (Brown, 1980). The thickness of the flow paths between the two wells is believed to be approximately 100 m, giving a flow rate of about 1 gpm for a unit depth of one meter. This is the test we modeled in the application problems (Chapter V).

These tests demonstrated that a Hot Dry Rock system can be constructed and operated to produce superheated water at temperatures suitable for generating electricity. However, commercial power plants require higher rates of heat production, reduced water losses and a credible basis for predicating useful lifetime of the heat source.

1.3 Previous Work

Wilson and Witherspoon (1970) have reviewed the work on fluid flow through fractured rocks, in the field of both groundwater hydrology and petroleum engineering. Their work includes an extensive set of references that is essentially complete to 1970. In this report, following the convention of Wilson and Witherspoon, the term "fracture" is used for most discontinuities within a rock mass. The word "joint" will be generally employed in connection with the finite element joint model.

The general approach to analysis of fluid flow through fractures has been to model fluid flow through fractures assuming viscous, incompressible flow between smooth parallel plates (Snow, 1965). The validity of the cubic law for laminar flow of fluids through open fractures consisting of parallel planar plates has been established by Witherspoon (1980) and Thomas (1987) in laboratory work. In an "open" fracture the planar surfaces remain parallel, and thus are not in contact at any point.

Deviations from the parallel plate model are expected because real joint surfaces are rough and contact each other at discrete points. In this thesis, realistic rough surfaces were considered using a factor of roughness. It has been discussed by Brown (1987) and Witherspoon (1980).

Witherspoon and Noorishad developed a finite element model of discrete fracture systems. The model coupled stress and fluid flow behavior in fractured rock masses. Direct application is to fluid flow problems in hydraulically fractured reservoirs and naturally fractured rocks (Noorishad, Ayatollahi and Witherspoon, 1982).

A two dimensional finite element model of fluid flow in fractured rock masses was developed by Hilber and Taylor (1979). The discontinuities are deformable and constitute the flow paths. The model includes interaction between the fluid and the fracture motions as well as inertia effects. They developed a computer code based on this theory. It determines the hydrodynamic state of the fluid, the displacement, strain and stress response histories of the rock masses, the change of the kinetic and the potential energy of the rock, and the amount of energy dissipated during slip.

A continuum approach has been developed for modeling mass transport in fractured rocks by Schwartz' and Smith (1988). It involves a new application of a particle tracking method in which physical transport is simulated in terms of velocity and the variations in velocity. This model successfully duplicates patterns of anisotropic dispersion predicated by de Josselin de Jong (1972). Applications demonstrate that the de Josselin de Jong approach for estimating dispersivities for idealized networks cannot generally be applied to networks formed from sets of finite, irregularly-spaced fractures. This model does not include rock deformation effects.

1.4 Objectives

Our goal is to develop a finite element fluid model to simulate flow through fractured rock. This model is the first step in developing a completely coupled flow/rock deformation/heat transfer model of the Hot Dry Rock reservoir. Figure 1.2 shows a schematic of the Hot Dry Rock reservoir. Discrete flow paths are used for the analysis, forming a fracture network connecting the two wells. We

model a plane section of the network, consisting of flow paths and blocks of rock masses. Two types of joints are present, shear joints that are closed and tension joints that are initially open. Fluid can be stored in the open joints.

We recognize that the density and viscosity of the fluid are functions of temperature. In the present model, we assume they are constant, as assumed by Hilber and Taylor (1979) in their model. We also assume the rock is not deformable and that the joint openings are constant. In the future development of this model, the coupling between rock deformation and heat transfer will be included.

The fluid model extends previous work by using a solution scheme applicable to nonlinear problems with a large number of unrestrained rock masses. Another important feature is the capability to model fluid storage in open joints. These joints are filled as fluid is pumped into the reservoir. The model includes the capability to simulate the use of tracers where tracers are pumped into the input well and the time history at the output is monitored.

In this thesis, we discuss only the fluid model. However, the fluid model was developed as part of a larger structural model, with the intent of coupling the two models. After the coupling, these features can give the engineer a tool to simulate flow and to check the results using interactive computer graphics. The engineer can observe flow paths develop as injection is started and will be able to follow the flow until it exits from the production wellbore. This tool will aid in understanding and predicting the fluid behavior of the Hot Dry Rock reservoir.

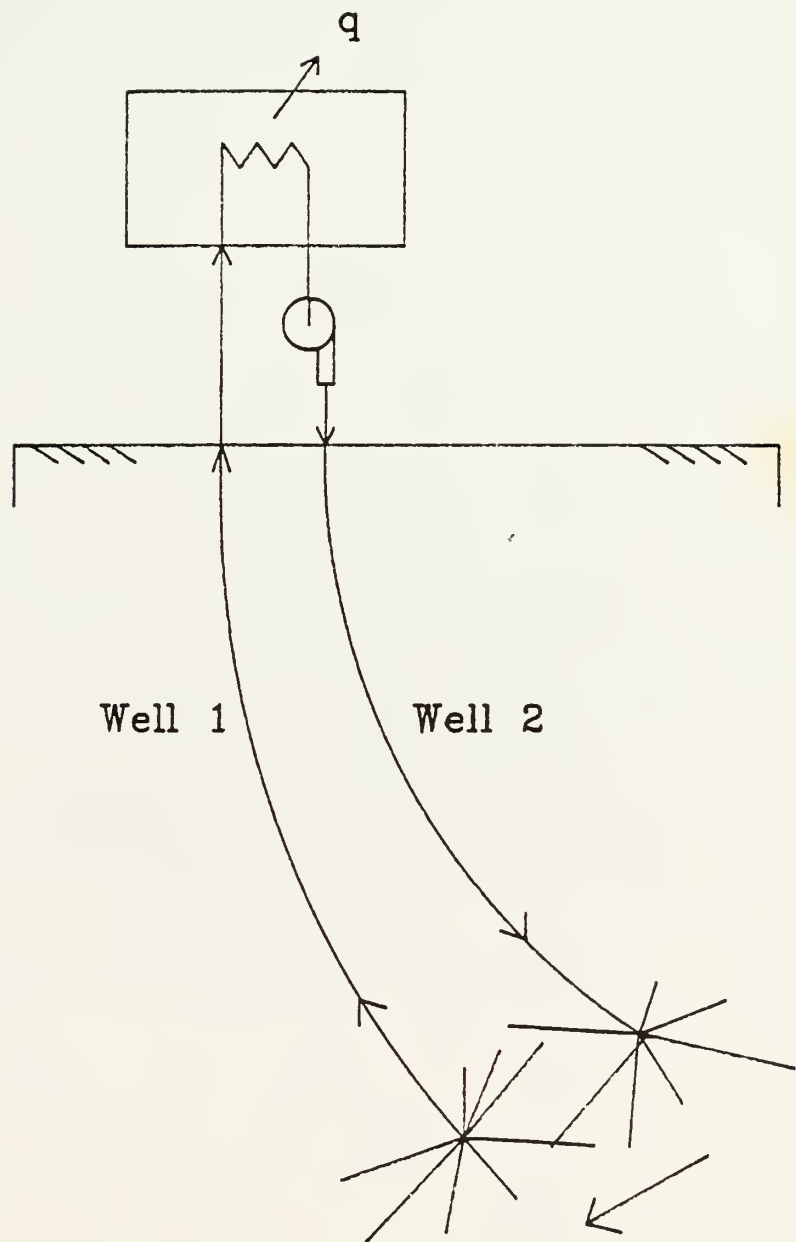


Figure 1.1: Schematic drawing of Phase II HDR Reservoir

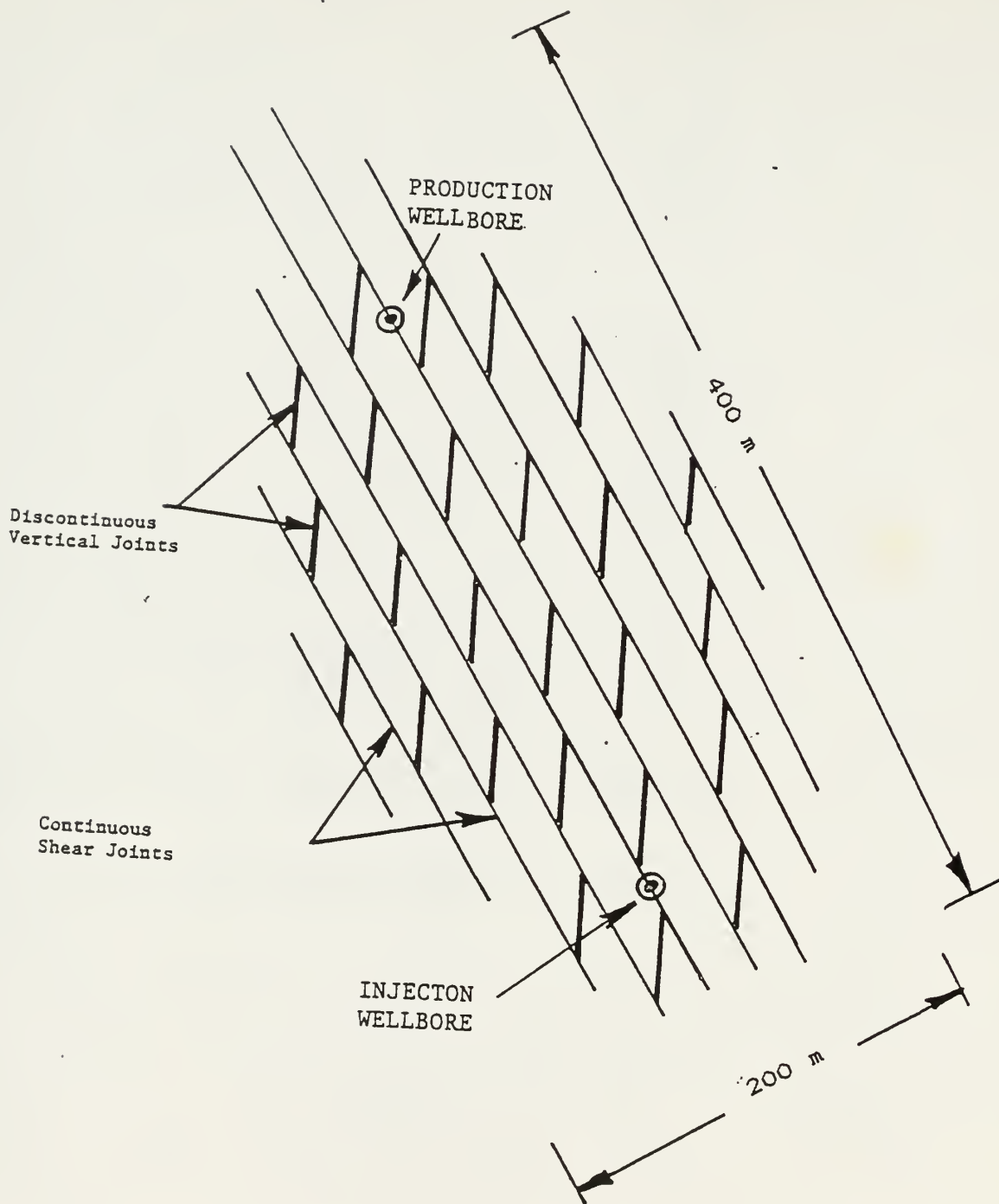


Figure 1.2: Schematic drawing of HDR Reservoir simulation

CHAPTER II

FLUID-FLOW NETWORK MODEL

In this chapter, we develop a model for fluid flow through non-porous rock masses. The fluid flow model is similar to the one discussed by Hilber and Taylor (1979). First we derive the relation between pressure gradient and flow rate for flow between parallel plates (cubic law).

2.1 Derivation of flow model

We first consider the fully-developed laminar flow between infinite parallel plates. The plates are separated by a distance a , as shown in Figure 2.1. The plates are considered infinite in the Z direction, without variation of any fluid parameter in this direction. The flow is further assumed to be steady and incompressible.

Because of the non-slip condition at the wall, the X component of velocity is zero at both the upper and lower plates. These two boundary conditions are as follow:

$$\begin{array}{lll} \text{at } y = +a/2 & u=0 & (2.1) \\ y = -a/2 & u=0. & \end{array}$$

Since the flow is fully developed, the velocity can not vary with X and is a function of Y only, $u = u(y)$. There is no component of velocity in either Y or Z directions, $v = w = 0$.

A differential control volume of size $dV = dXdYdZ$ is selected (Fig.2.1) and applied to the X component of the momentum equation:

$$\begin{array}{ccccc} F_{Sx} & + & F_{Bx} & = & \frac{\partial}{\partial t} \int_{cv} u \rho dV + \int_{cs} \vec{u} \rho \vec{v} \cdot d\vec{A} \\ (1) & & (2) & & (3) \qquad \qquad (4) \end{array} \quad (2.2)$$

F_{Sx} represents surface force and F_{Bx} represents body force. Term

(4) indicates the momentum flux through the control surface area $d\vec{A}$. Term (3) represents the rate of change of momentum. For steady flow, all fluid parameters are independent of time and term (3) equals zero. The net momentum flux through the control surface is zero as a result of fully-developed flow and term (4) equals zero. We assume there is no body force in X direction, thus term (2) equals zero. Finally, the momentum equation reduces to,

$$F_{sx} = 0 \quad (2.3)$$

We now sum the forces acting on the control volume in the X direction. There are normal forces (pressure forces) acting on the left and right faces; there are tangential forces (shear forces) acting on the top and bottom faces.

Suppose the pressure at the left face of the element is p , then the force on the left face is

$$p \, dydz \quad , \quad (2.4)$$

and the force on the right face is

$$- \left(p + \frac{dp}{dx} dx \right) dydz \quad . \quad (2.5)$$

Similarly for the shear stress τ_{yx} , the shear force on the bottom

face is

$$- \tau_{yx} dx dz, \quad (2.6)$$

and the shear force on the top face is

$$\left(\tau_{yx} + \frac{d\tau_{yx}}{dy} dy \right) dx dz. \quad (2.7)$$

Summing the forces acting on each face of the control volume, we can simplify the equation to

$$- \frac{dp}{dx} + \frac{d\tau_{yx}}{dy} = 0 \quad (2.8)$$

or

$$\frac{d\tau_{yx}}{dy} = \frac{dp}{dx} = \text{constant}. \quad (2.9)$$

Integrating this equation, we obtain

$$\tau_{yx} = \frac{dp}{dx} y + C_1. \quad (2.10)$$

Using the definition of Newtonian fluid $\tau_{yx} = \mu (du/dy)$ where

μ is the dynamic viscosity, gives

$$\mu \frac{du}{dy} = \frac{dp}{dx} y + C_1 \quad (2.11)$$

and

$$u = \frac{1}{2\mu} \frac{dp}{dx} y^2 + \frac{C_1}{\mu} y + C_2. \quad (2.12)$$

Applying boundary conditions, gives

$$C_1 = 0, \quad (2.13)$$

$$C_2 = - \frac{1}{\mu} \frac{dp}{dx} \frac{a^2}{8}, \quad (2.14)$$

and

$$u = \frac{1}{2\mu} \frac{dp}{dx} \left(y^2 - \frac{a^2}{4} \right). \quad (2.15)$$

We calculate the average velocity \bar{u}

$$\int_{-a/2}^{a/2} \bar{u} dy = \int_{-a/2}^{a/2} \frac{1}{2\mu} \frac{dp}{dx} \left(y^2 - \frac{a^2}{4} \right) dy, \quad (2.16)$$

and obtain

$$\bar{u} = - \left(\frac{a^2}{12\mu} \right) \frac{dp}{dx}. \quad (2.17)$$

The volumetric flowrate is given by

$$Q = \int_A \vec{V} \cdot d\vec{A}. \quad (2.18)$$

For a unit depth 1 in the Z direction

$$Q = \int_{-a/2}^{a/2} \bar{u} l dy, \quad (2.19)$$

or

$$\frac{Q}{1} = \int_{-a/2}^{a/2} \frac{1}{2\mu} \left(\frac{dp}{dx} \right) \left(y^2 - \frac{a^2}{4} \right) dy. \quad (2.20)$$

Thus the volumetric flowrate per unit depth, (q) is:

$$q = - \left(\frac{a^3}{12\mu} \right) \left(\frac{dp}{dx} \right). \quad (2.21)$$

In real applications, especially for those small apertures, fracture walls are not strictly smooth and surface roughness can cause turbulence or a boundary layer in the flow (Ryan and Kimbrell, 1987). To approximate this, we include a factor of roughness which can cause an apparent reduction in flow,

$$q = - \left(\frac{a^3}{12\mu f} \right) \left(\frac{\partial p}{\partial x} \right) . \quad (2.22)$$

According to the investigations of Witherspoon (1980) and Sundaram (1987), the factor f varies from 1.04 to 1.78 which depends on the mechanical properties of fractures and rock. According to the investigations of Louis (1969) and Wilson (1970), turbulence only exists in a small portion of the network which has large hydraulic gradients. Louis (1969) states the effect of turbulence is only small within the fluid system, and that the assumption of laminar flow can be considered a good approximation. Only when large portion of the fluid network is turbulent, the total flow will be significantly over estimated by the laminar flow. The validity of the cubic law for laminar flow through open fractures consisting of parallel plates has been established with apertures ranging down to a minimum of 0.2 μm (Witherspoon et al., 1980).

Defining $K_p = a^3/12\mu f$ as the joint permeability, we obtain the relation between flowrate and pressure gradient,

$$q = - K_p \left(\frac{dp}{dx} \right) . \quad (2.23)$$

2.2 One Dimensional finite element model

2.2.1 The differential fluid element

We now derive the differential equation for one dimensional fluid flow. The differential fluid element with a unit depth is shown in Figure 2.3. The density of the fluid is assumed to be constant. The size of joint opening will change the volume of the differential element, so it must be included in the formulation. It is assumed that ρ is the fluid density, u is the average velocity of fluid and a is the joint opening. From the law of conservation of mass:

$$\rho ua - \left[\rho ua + \frac{\partial}{\partial x} (\rho ua) dx \right] = \frac{\partial}{\partial t} (\rho a) dx, \quad (2.24)$$

we obtain

$$- \frac{\partial}{\partial x} (\rho ua) = \frac{\partial}{\partial t} (\rho a). \quad (2.25)$$

Since $\rho = \text{constant}$,

$$- \frac{\partial}{\partial x} (ua) = \frac{\partial a}{\partial t}. \quad (2.26)$$

From the definition of volumetric flowrate $Q = ual$ (l is depth)

define the volumetric flowrate per unit depth as $q = ua$

$$\frac{\partial q}{\partial x} + a = 0, \quad (2.27)$$

where the derivative with respect to time is indicated by $(\dot{})$.

Assuming the flow rate is proportional to the pressure gradient (equation 2.23), where K_p is the joint permeability,

we obtain;

$$\frac{\partial}{\partial x} \left(K_p \frac{dp}{dx} \right) - \dot{a} = 0 . \quad (2.28)$$

2.2.2 Quadratic one-dimensional element formulation

The interpolation equation for the one-dimensional quadratic element (Figure 2.2) is

$$\phi(\xi) = a_1 + a_2\xi + a_3\xi^2 . \quad (2.29)$$

The shape functions for the one-dimensional quadratic element relative to the ξ - coordinate system are

$$\begin{aligned} N_1(\xi) &= (\xi/2)(\xi-1) \\ N_2(\xi) &= -(\xi-1)(\xi+1) \\ N_3(\xi) &= (\xi/2)(\xi+1) \end{aligned} \quad (2.30)$$

so

$$X(\xi) = N_1(\xi) X_1 + N_2(\xi) X_2 + N_3(\xi) X_3 . \quad (2.31)$$

The Jacobian of the transformation is

$$\frac{dx(\xi)}{d\xi} = \xi(X_1 - 2X_2 + X_3) + \frac{X_3 - X_1}{2} . \quad (2.32)$$

Assuming node 2 is at the middle point of the element,

$$X_1 - 2X_2 + X_3 = 0 \quad (2.33)$$

and

$$\frac{dX(\xi)}{d\xi} = \frac{L}{2} \quad (2.34)$$

where $X_3 - X_1 = L$, the element length.

The row vector $[D]$ contains the derivatives of element shape functions with respect to X written in terms of the ξ - natural coordinate system,

$$[D] = \left(\frac{dN_1}{dX}(\xi) \quad \frac{dN_2}{dX}(\xi) \quad \frac{dN_3}{dX}(\xi) \right) . \quad (2.35)$$

We use the chain rule to obtain,

$$\frac{dN_1}{d\xi} = \frac{dN_1}{dX} \frac{dX}{d\xi} , \quad (2.36)$$

giving

$$[D] = \frac{2}{L} \left\{ \left(\xi - \frac{1}{2} \right) \quad -2\xi \quad \left(\xi + \frac{1}{2} \right) \right\} . \quad (2.37)$$

2.2.3 Galerkin's method

The weighted residual integral is the line integral along the X direction. We will assume the weighting function for the S th node, W_s , consists of the shape functions associated with the S th node (Segerlind, 1984). Therefore $[W_s] = [N_s]$, $[N]$ is the row vector containing the element shape functions. Defining a column vector $\{R\}$, each component of $\{R\}$ represents a residual equation,

$$\{R\} = \int_L [N]^T \left\{ \frac{\partial}{\partial x} \left(Kp \frac{dp}{dx} \right) - \dot{a} \right\} dx , \quad (2.38)$$

separating the terms inside the integral

$$\{R\} = \int_L [N]^T \frac{\partial}{\partial x} (Kp \frac{\partial p}{\partial x}) dx - \int_L [N]^T a dx . \quad (2.39)$$

Integrating by parts, gives

$$\{R\} = [N]^T Kp \frac{\partial p}{\partial x} \Big|_{L_1}^{L_2} - \int_L Kp \frac{dp}{dx} \frac{\partial [N]^T}{\partial x} dx - \int_L [N]^T a dx . \quad (2.40)$$

The integration over the body in equation (2.40) is performed dividing the body into elements and summing the integration over each element. For each element, we have,

$$\frac{\partial p}{\partial x} = [D] [P] . \quad (2.41)$$

We can obtain

$$\{R\} = [N]^T q \Big|_{L_2}^{L_1} - \int_L Kp [D] [P] [D]^T dx - \int_L [N]^T a dx . \quad (2.42)$$

Because $\dot{a} = [N] [\dot{a}]$ and both $[P]$ and $[\dot{a}]$ are constant with respect to the integration,

$$\{R\} = [N]^T q \Big|_{L_2}^{L_1} - \int_L Kp [D] [D]^T dx [P] - \int_L [N]^T [N] dx [\dot{a}] . \quad (2.43)$$

From the element matrix formulation equation (2.37), we expand $[D]^T [D]$ to obtain,

$$[D]^T [D] = \frac{4}{L^2} \begin{vmatrix} (\xi-1/2)^2 & -2\xi(\xi-1/2) & (\xi^2-1/4) \\ -2\xi(\xi-1/2) & 4\xi^2 & -2\xi(\xi+1/2) \\ (\xi^2-1/4) & -2\xi(\xi+1/2) & (\xi+1/2)^2 \end{vmatrix}$$

$$= \frac{4}{L^2} [B] . \quad (2.44)$$

We use the shape functions to describe the fracture opening in equation 2.23, $K_p = a^3/12\mu f$

$$= \{[N] [a]\}^3/12\mu f \quad (2.45)$$

substitute (2.44) and (2.45) into equation 2.43, gives,

$$\{R\} = [N]^T q \int_{L_2}^{L_1} - \frac{4}{12\mu L^2 f} \int_L \{[N] [a]\}^3 [B] dx [P] - \int_L [N]^T [N] dx [a] \quad (2.46)$$

(3)
(2)
(1)

Integration is done numerically by transforming to the natural element coordinate system. We can transform term (1) from the global coordinate system X to the natural coordinate system ξ by,

$$\frac{L}{2} \int_{-1}^1 [N] [N]^T d\xi [a] = [S] [a] , \quad (2.47)$$

where $[S]$ is the storage matrix due to crack opening velocities.

Similarly, transforming the stiffness matrix,

$$\frac{1}{3\mu L^2 f} \int_L \{[N] [a]\}^3 [B] dx = \frac{1}{6\mu L f} \int_{-1}^1 \{[N] [a]\}^3 [B] d\xi . \quad (2.48)$$

Using the shape functions in terms of the natural coordinates, we obtain for the stiffness matrix,

$$[K] = \frac{1}{6\mu Lf} \int_{-1}^1 \left[\left(\frac{a_1}{2} - a_2 + \frac{a_3}{2} \right) \xi^2 + \left(\frac{a_3}{2} - \frac{a_1}{2} \right) \xi + a_2 \right]^3 [B] d\xi, (2.49)$$

Finally we get,

$$\{R\} = \{Q\} - [K]\{P\} + [S]\{\dot{a}\}. (2.50)$$

Setting $\{R\} = \{0\}$

$$[K]\{P\} = \{Q\} + [S]\{\dot{a}\}, (2.51)$$

where $[K]$ is the permeability (stiffness) matrix, $\{P\}$ is the column vector containing nodal pressures, $\{Q\}$ is a vector of specified flow rates, $[S]$ is the storage matrix due to the opening of the gap, and $\{\dot{a}\}$ is the gap opening velocity at the nodes. We can solve equation (2.51) for nodal pressures.

2.3 One Dimensional Tracer Model

Tracer are used to track the motion of fluid in the system of fractures and can provide important information on the fractures system. Typically, the tracer is a chemical or radioactive material that is mixed with the injected fluid and the concentration is monitored at the output. In Fenton Hill experiments, engineers have used sodium fluorescein dye, sodium bromide and sodium nitrate to estimate the volumes of fractured systems.

The first derivation of the tracer model is for an active element already filled with fluid. The differential tracer element with a unit depth is shown in figure 2.4. The fluid is assumed incompressible. The concentration of tracer is denoted by c , u is the

average velocity of fluid and a is the gap opening. From the law of conservation of mass:

$$cua - \left[cua + \frac{\partial}{\partial x} (cua) dx \right] = \frac{\partial}{\partial t} (ca) dx . \quad (2.52)$$

Differentiating the right side,

$$- \frac{\partial}{\partial x} (cua) = \frac{\partial c}{\partial t} a + \frac{\partial a}{\partial t} c . \quad (2.53)$$

The differential form becomes

$$\frac{\partial c}{\partial t} = \frac{1}{a} \left(- \frac{\partial}{\partial x} (cua) - c \frac{\partial a}{\partial t} \right) . \quad (2.54)$$

We solve equation 2.54 using a simple finite difference scheme. It is assumed that a fluid element is divided into three sections. For each section, the current tracer is going to next section and will be replaced by the new coming tracer. The movement depends on the direction of fluid velocity. Equation(2.54) gives the rate of change of concentration in each section of fluid element.

$$\frac{\partial c}{\partial t} = \frac{c_{\text{new}} - c_{\text{old}}}{\Delta t} \quad (2.55)$$

and

$$\frac{\partial}{\partial x} (cua) = \frac{cua|_{\text{in}} - cua|_{\text{out}}}{\Delta x} \quad (2.56)$$

$$\frac{\partial a}{\partial t} = \frac{a_{\text{new}} - a_{\text{old}}}{\Delta t} \quad (2.57)$$

$$c_{\text{new}} = c_{\text{old}} + \frac{\Delta t}{a} \left(\frac{c_{\text{ua}}|_{\text{in}} - c_{\text{ua}}|_{\text{out}}}{\Delta x} - c \frac{a_{\text{new}} - a_{\text{old}}}{\Delta t} \right) \quad (2.58)$$

Equation(2.58) shows the relationship between current tracer and the new coming tracer.

In the fluid system network, mixing of the tracer occurs at the connecting nodes of fluid elements. The calculation of tracer mixing is illustrated in Figure 2.5, where there are two branches of fluid flowing into a fluid element. At node I the calculation of concentration of input tracer is a weighted average of the input concentration,

$$c_{\text{input}} = \frac{u_1 c_1 + u_2 c_2}{u_1 + u_2} \quad (2.59)$$

The output concentration is the current concentration at the node. For nonactive fluid elements, the calculation of mixing of tracer is as follows (refer to Figure 2.5). The input node for any inactive element may be connected to several other active or nonactive elements. The active elements give the total flow into the node. The flow into each inactive element is distributed using the permeabilities of the inactive elements.

In Figure 2.5, there are three inactive elements at the input node. The input to element number 23 is then:

At node I

$$q_{in} = (q_1 + q_2) \frac{K_{pi}}{K_{pi} + K_{p1} + K_{p2}} \quad (2.60)$$

and

$$c_{in} = (c_1 + c_2) \frac{K_{pi}}{K_{pi} + K_{p1} + K_{p2}} \quad (2.61)$$

The concentration of tracer in this element becomes

$$c_{old} = \frac{c_i Q_i \Delta t + c_k Q_k \Delta t + c_{old} V_{filled}}{Q_i \Delta t + Q_k \Delta t + V_{filled}} \quad (2.62)$$

K_p indicates the conductivity of fluid element, q is the flowrate in the active element, and c is the concentration of tracer. V_{filled} means the volume of the element which is already filled with fluid.

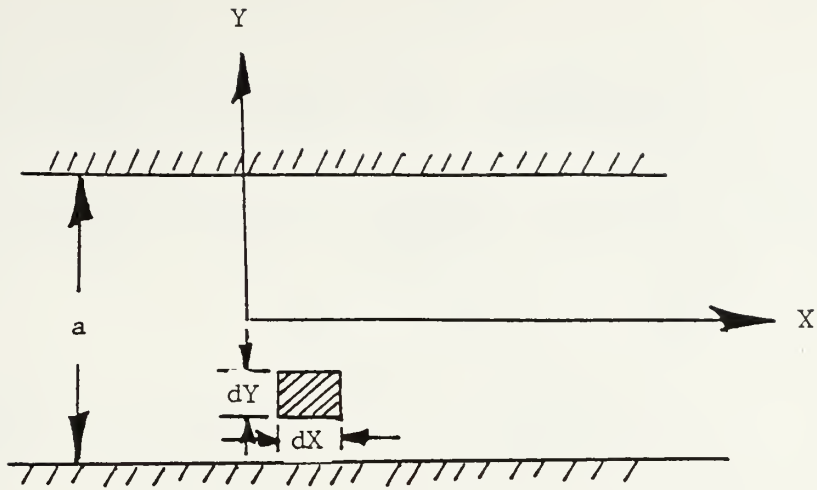


Figure 2.1: Fluid flow between two parallel plates

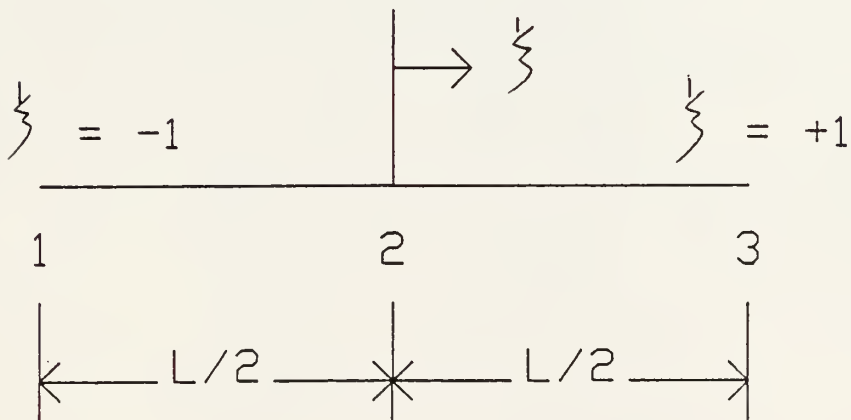


Figure 2.2: One-Dimensional Quadratic element

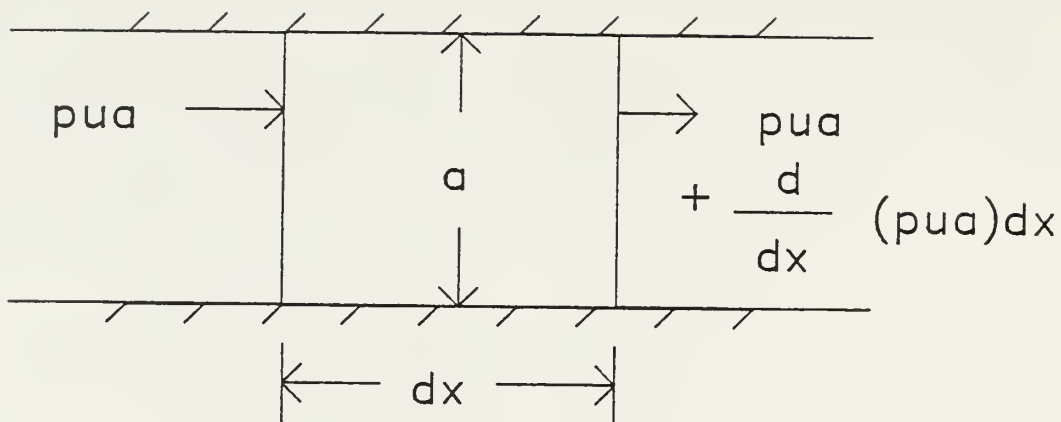


Figure 2.3: Differential fluid element

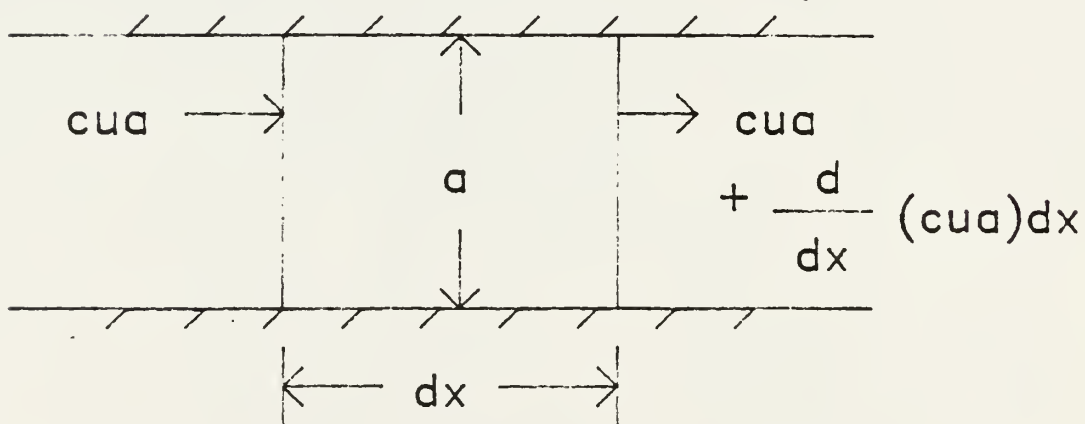


Figure 2.4: Differential tracer element

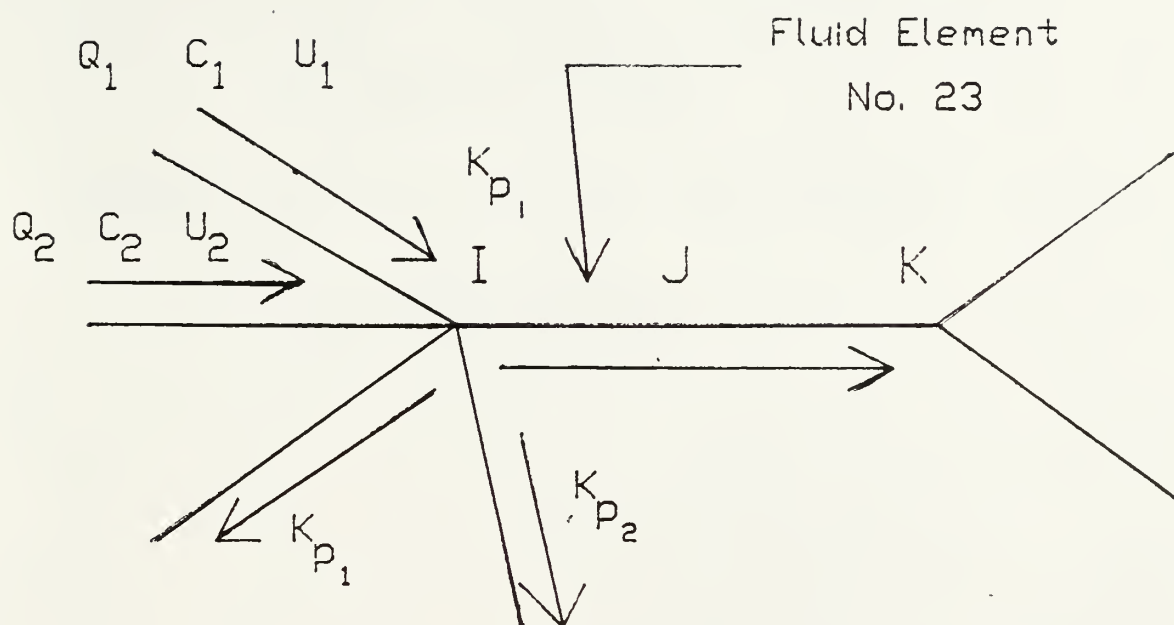


Figure 2.5: Example of tracer mixing at a joint

CHAPTER III

DESCRIPTION OF FLUCRK

This chapter provides a brief description of FLUCRK. Significant features of the implementation include the use of dynamic relaxation, the connection between the structure model and fluid model, the use of active/nonactive elements to model storage, and the use of interactive computer graphics to specify the problem and examine the results. The flow chart of FLUCRK is shown in Fig.3.1.

3.1 User Interaction

3.1.1 Automated mesh generation

Before executing FLUCRK, the user must generate a mesh. A short program called "AU-MESH" allows the user to generate simple symmetric meshes interactively. The program automatically creates an output geometry file which can be read by FLUCRK. This program was used to generate the meshes used in application calculations (chapter V).

3.1.2 Interactive Problem specification

After the geometry file has been read into FLUCRK, the problem specification is performed interactively. The user can modify the mesh by deleting or adding elements. The user can enter the FLUID MAT COND page to examine and change material properties interactively. The FLUID BC page allows the user to specify boundary conditions (either pressure vs time or velocity vs time) at arbitrarily picked nodes. The far field boundary conditions (Section 3.4) are specified using a flowrate vs pressure curve. In the ANALYSIS PARAMETER page

the user can set the start time, the end time, the time intervals to store analysis results, restart data, and plot data. Parameters controlling the solution are specified in the FLUID page.

Besides these parameters, the user can also specify the gap opening used to flag whether an element is active. Elements with large initial openings accumulate fluid until they are filled, elements with smaller gaps are assumed filled and initially active.

At the MAIN page, there are two options used to manually save problem data. These are the SAVE RESTART and SAVE PLOT functions. SAVE RESTART saves all problem data at the present time in a restart file. The user can then retrieve all the problem data to rerun the analysis. SAVE PLOT will save plot data for the current time.

Once a problem is finished, the user can always return to change parameters or boundary conditions and execute the problem using the RESTART function or examine the results by entering the PLOTS page.

In the FLUID PLOT page, there are nine functions to examine results already obtained. These functions are divided into two parts. One is color plots of a specified parameter (pressure, flowrate, velocity or tracer) at a chosen time step. Another is time history plots (pressure, flowrate, velocity, tracer or kinetic energy). Quantities are displayed as a function of time at a specified node or element.

3.2 Connection Between Structure Elements and Fluid Elements

This finite element model was developed as part of a large structural code, CRACKER (Swenson, 1985), which can solve both dynamic and static problems. CRACKER uses six noded triangular elements to model the continuum and includes interface elements to model contact between bodies. We added a third element type, a one dimensional fluid element. As illustrated in Figure 3.3, each fluid element lies between two structural elements and has six nodes. However, only three nodes per element are required to represent the network of fluid elements. To save storage in the fluid solution, a fluid model numbering system is used that is independent of the structural nodes. The fluid numbering system (P_1 , P_2 , P_3 , etc) is invisible to the user, but is automatically generated when the fluid solver is entered.

We create two array listings to define the connection between the fluid and structure elements. The first array is called a connectivity list and indicates the node numbers of the structure and fluid nodes in each fluid element. We use the following storage, where ELEM indicates the fluid element number,

CONN(1-6,ELEM) : STRUCTURE NODE NUMBERS

CONN(7,ELEM) : ELEMENT TYPE

CONN(8,ELEM) : MATERIAL NUMBER (SPECIFIED BY USER)

CONN(9-11,ELEM): FLUID NODE NO.

This array allows the program to go from the fluid elements to the fluid nodes.

Another array listing which we call the inverse connectivity list stores the number of all fluid elements connected to each fluid node.

This array gives the program pointers from the fluid nodes to elements. The array is used when calculating net flow into any node. For a fluid node, FLUID, this data is stored as,

FLOW_CON(1,FLUID) : NO. OF FLUID ELEMENTS CONNECT TO THE NODE

FLOW_CON(2,FLUID) : POINTER TO ELEMENT NUMBER LIST

FLOW_PT(FLUID) : ELEMENT NUMBER LIST

The above data storage scheme eliminates the need for repeated searching to identify connectivity.

3.3 Active/Nonactive Element

Conceptually, the joint network includes joints that are initially open. These joints must be filled with fluid before we can assume that conservation of mass applies for that joint. Until the open joints are filled, they are called nonactive. The pressure at the nodes of nonactive elements are assumed zero and they are not included in the solution of equation (2.51). Instead, they supply boundary conditions to this equation. Once it is full, the element is turned active and included into the pressure calculation.

For all initially inactive elements, the initial empty volume is calculated. In each time step, the flow into the inactive elements is calculated and the new empty volume obtained. The total flow into the empty joint is calculated and used to obtain the new empty volume,

$$v_{\text{empty}}^{\text{new}} = v_{\text{empty}}^{\text{old}} - (\text{Total flow rate in}) * \text{TSTEP} ,$$

where TSTEP is the time increment. If V_{empty} is smaller than or equal to zero, that means the fluid element is filled with fluid. It is automatically turned on to active status and included into the flow calculation.

In general, several active/nonactive elements may connect at one node. Total flow into the node is obtained using all active elements. If more than one nonactive element is connected to a node, the flow is proportioned to the nonactive elements using their conductivities.

If an element fills in the middle of a time step, all additional flow into that element is lost to the calculation. It is important to choose the time step small enough that this loss is minimized.

3.4 Far Field Boundary Condition

The finite element model can not extend to infinity, including all flow paths between the wells. Instead, we can include only a finite region around the two wells. We call this boundary around the problem the far field boundary. In the real problem, flow leaks out of this boundary into the infinite system. As a first approximation, we assume the leakage is a function of pressure at the far field boundary nodes. The user can specify a nonlinear relation of pressure vs flowrate. As will be discussed in chapter V, we examine the sensitivity of the solutions to the far field boundary conditions.

3.5 Solution Technique

Dynamic relaxation (Day, 1965; Underwood, 1983; Papadrakakis, 1981) is the technique used to obtain the solution to equation 2.51.

Dynamic relaxation (DR) is an explicit iterative method for the static solution of simultaneous equations. It is based on the fact that a system undergoing damped vibration excited by a constant force ultimately comes to rest in the displaced position of static equilibrium of the system. It has been extensively used for both linear and nonlinear structure analysis (Frieze, Hobbs and Dowling, 1978; Pica and Hinton, 1980). This method is derived from the dynamic equilibrium equation:

$$[M]\ddot{[P]} + [C]\dot{[P]} + [K][P] = [Q] , \quad (3.1)$$

where $[M]$ is a mass matrix, $[C]$ is a damping matrix, $[K]$ is the stiffness matrix, $[P]$ is the fluid pressure vector, $[Q]$ is the flowrate vector and the dot represents differentiation with respect to time.

Using the method of central difference, we can get $\dot{[P]}$, $\ddot{[P]}$ and $[P]$ as follows :

$$\ddot{P} = \frac{[Q] - C \dot{P} - K P}{M}$$

$$\dot{P}_{\text{new}} = \dot{P}_{\text{old}} + \ddot{P} h , \quad (3.2)$$

$$P_{\text{new}} = P_{\text{old}} + \dot{P} h$$

where h is a fixed time increment. To preserve the explicit form of the central difference integrator $[M]$ must be diagonal and the damping matrix $[C]$ has the form $[C] = c [M]$.

To obtain the static solution from the equation, we should select the damping coefficient c , the time increment h , and the mass matrix $[M]$ to converge rapidly. Physically, the damping, time increment and mass are selected so that the transient response will reach the steady state under the applied load Q . Only P and Q must represent the physical problem and c and M do not need to represent the physical structure (Underwood 1983).

The pseudo mass matrix $[M]$ here being used is derived from Gerschgorin's theorem :

$$m_{ii} = \frac{1}{4} h^2 \sum |K_{ij}|, \quad (3.3)$$

where m_{ii} are the diagonal elements of the pseudo mass matrix and K_{ij} are the elements of the stiffness matrix K . Underwood (Underwood 1983) suggested evaluating $[M]$ for $h = 1.1$ and iterating with $h = 1$ to ensure stability. We found it was necessary to use $h = 0.5$ for stability.

The damping matrix coefficient is computed at each iteration from Rayleigh's quotient as (Underwood, 1983) :

$$C = 2 \sqrt{[P]^T [K] [P] / [P]^T [M] [P]} \quad (3.4)$$

The flow chart of dynamic relaxation is shown in Figure 3.2.

We have tested two different convergence criteria. The first uses the maximum kinetic energy during the solution. At each iteration, the current kinetic energy is compared to the maximum kinetic energy times a factor. If the current energy is smaller, we assume that the system is converged. The difficulty with this criteria is that

pressure boundary conditions can lead to a large initial kinetic energy, and convergence is not obtained unless a very small factor is used. Under this condition, the result is not reliable. The second criteria checks the difference between the previous pressures and current pressures divided by previous pressures. If the difference is smaller than the tolerance specified by the user, we assume the pressures are converged. The reasonable tolerance is picked by a series of trial and error tests.

The main advantage of dynamic relaxation lies in its basic simplicity and the straightforward algorithms which can be written for complicated problems. In the implementation, no global matrices are actually formed. Instead, equation 3.1 is solved by looping in all elements and accumulating the unbalanced forces. There is no required numbering scheme for the elements or nodes, which is ideal for the present application, that includes active and inactive elements that change during the analysis. An additional advantage is the exceptional robustness of this solution scheme for nonlinear problems, such as when the structural model is coupled to the fluid model and fluid flow becomes a cubic function of joint opening (equation 2.22).

The main disadvantage of this method is the relatively long solution time compared to direct solution methods for a linear system of equations.

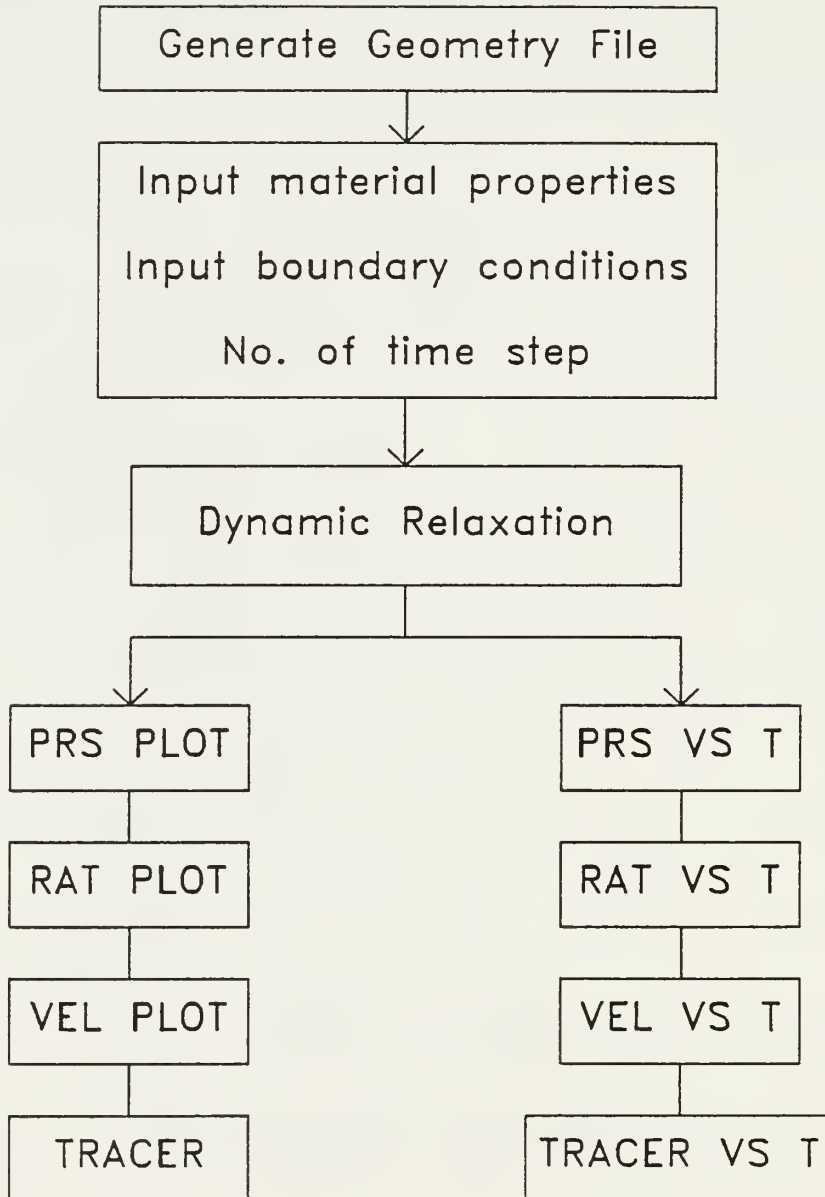


Figure 3.1: Flow chart of FLUCRK

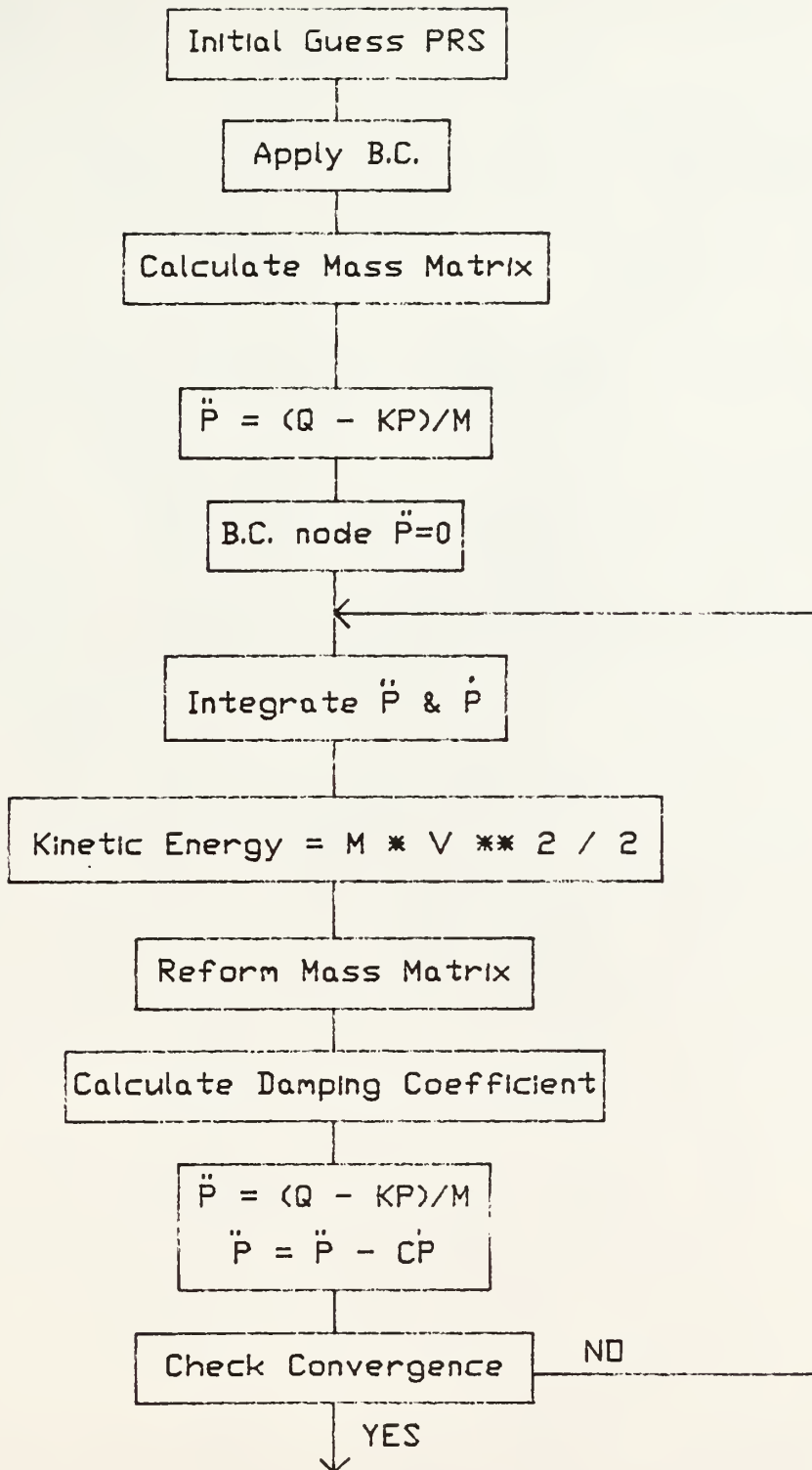


Figure 3.2: Flow chart of DR

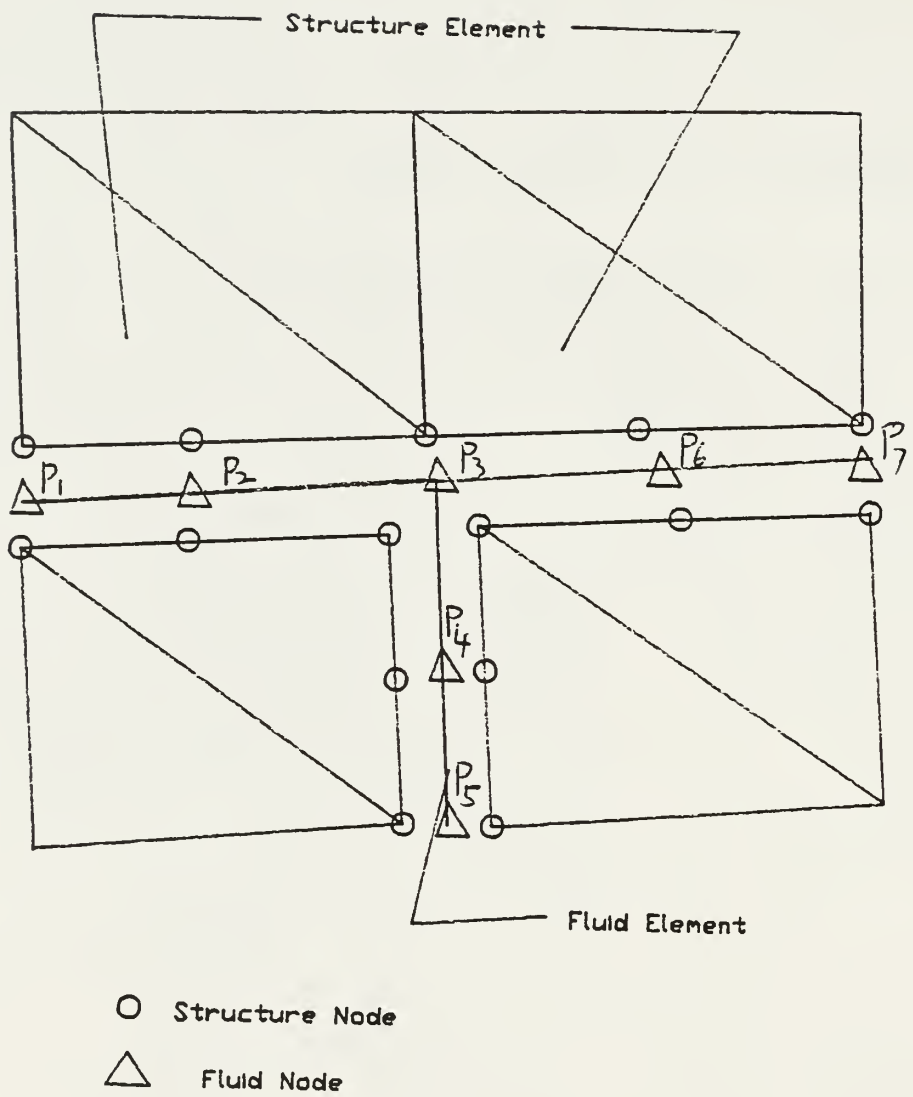


Figure 3.3: Connection between structure element and fluid element

CHAPTER IV

VERIFICATION PROBLEMS

A number of verification problems have been solved to test the computer program and to demonstrate the method of analysis described in chapter II. Problems one and two are designed to test the effect of fluid flow while all fluid elements are active (problem one) and nonactive (problem two) at the beginning. They use the same mesh with a straight flow path that includes 25 fluid elements. Tracer was pumped into the flow path in these two problems to verify the motion of tracer through time. Problem three demonstrates the mixing of fluid flow and the change of concentration of tracer in multiple flow paths. Problem four tests the specification of nonlinear far field boundary conditions.

4.1 Problem One - Flow in Crack

This problem is a simple one dimensional problem (Figure 4.1). Fluid flow was pumped into the left side under constant pressure and output from the exit in right side. Twenty five fluid elements construct a straight flow path and they are all filled with fluid at the beginning. The problem was solved for 25 time steps of 1 sec each.

All elements had the same dynamic viscosity $\mu = 0.15 \times 10^{-5} \text{ N-s/m}^2$ and gap opening $a = 0.03 \text{ m}$, as shown in Figure 4.1. The input pressure was 20 Pa and output pressure was 0 Pa. Both were kept constant during the analysis.

The calculated flowrates at the input and output elements are shown in Figure 4.2 and Figure 4.3. They both are identical in every time step and correspond to the expected values.

To demonstrate calculations using the tracer option, we injected tracer as a pulse from 2 through 5 sec. The input concentration was 100%. Time history plots of the tracer at the input, center, and output nodes are shown in Figure 4.4. The flow of the tracer from the input to output is clearly seen, with the pulse travelling at the velocity of the fluid. Some numerical diffusion of the tracer is seen to occur.

This example shows the pressure decreased linearly from the input to output pressure, and flowrates and velocities are constant through the problem. It also demonstrates that the tracer calculation works correctly.

4.2 Problem Two - Flow in Empty Crack

Problem two uses the same geometry and mesh as problem one. The only differences are that all fluid elements (except those connected to the input and output nodes) are initially nonactive and the gap opening is 0.05 m. This example demonstrates filling of empty elements.

The specified input pressure was 2 N/m^2 and the output pressure was 0 N/m^2 . Flowrates of the input element and output element are displayed in Figure 4.5 and Figure 4.6. Initial flowrates are high due to the empty elements next to the input elements. As the flow progressively fills the elements, the resistance to flow increases and the flow rate drops. Figure 4.7 demonstrates the pressure and

flowrates at middle of the flow path. The middle element turned on after fluid flow filled it after 9 time steps. After twenty two time steps, all fluid elements were filled with fluid, pressures decreased linearly between input and output, and flowrates were constant everywhere.

The expected flowrate is:

$$Q = \frac{a^3}{12\mu f} \frac{dp}{dx} , \quad (4.1)$$

$$= 0.14 \text{ m}^3 / \text{sec}$$

which is identical to Figure 4.6.

Figure 4.8 displays the motion of tracer at input, middle and output locations of this crack system.

4.3 Problem Three - Flow in Simple Network

Problem three has ten fluid elements initially active with a gap opening of 0.01 m as shown in Figure 4.9. Fluid was pumped into two entries in the left side at 5 N/m^2 and output from two exits in the right side at 0 N/m^2 . The calculated flowrates at the entry and exit are displayed in Figure 4.10 and Figure 4.11. Figure 4.12 shows the fluid properties at middle flow path where the pressure equals half of the input pressure and the flowrate equals the sum of two input flowrates.

The motion of tracer is shown in Figure 4.13. Tracer was pumped into one entry at a concentration of 100%. The concentration of

tracer at the middle of flow path is only 50% because of the mixing of the two input flows. When the flow splits at the output, the concentration remains at 50%. Because of the relatively coarse mesh used, diffusion of the tracer occurs at the output. Figure 4.14 shows the pressure plot. The pressure decreased linearly from the input to the output within each element. The overall tracer plot is displayed in Figure 4.15, which shows the reduction in concentration of tracer after mixing.

4.4 Problem Four - Far Field Boundary Conditions

This problem tests the option to specify a pressure-flowrate relation at the far field boundary conditions (Figure 4.16). It is assumed the far field condition is a nonlinear relation between pressure and flowrate as shown in Figure 4.17. The input flowrate boundary condition at fluid node 5 is between fluid element 2 and 3. The value of the input flowrate is $1 \text{ m}^3/\text{sec}$.

Figure 4.18 and Figure 4.19 show the results of flowrates of fluid elements 2 and 3, with the absolute sum of them equal to the input flowrate $1 \text{ m}^3/\text{sec}$. Pressures at both ends and input node are displayed in Figure 4.20.

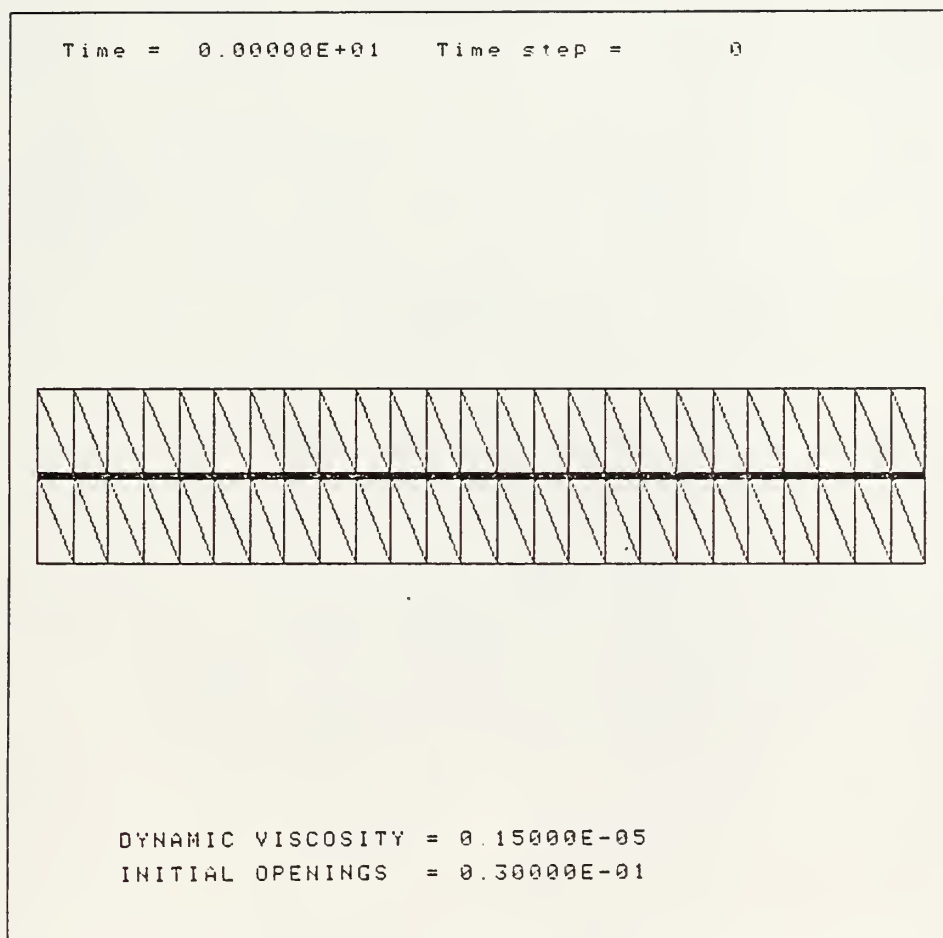


Figure 4.1: Verification problem one

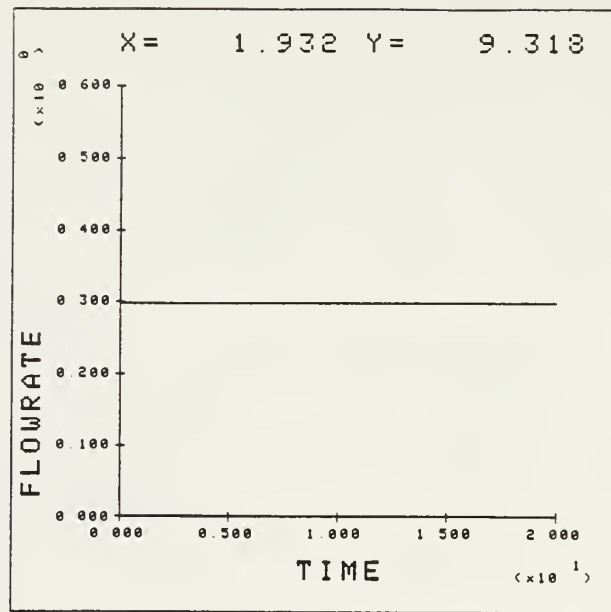


Figure 4.2: Flowrate of input element (problem one)

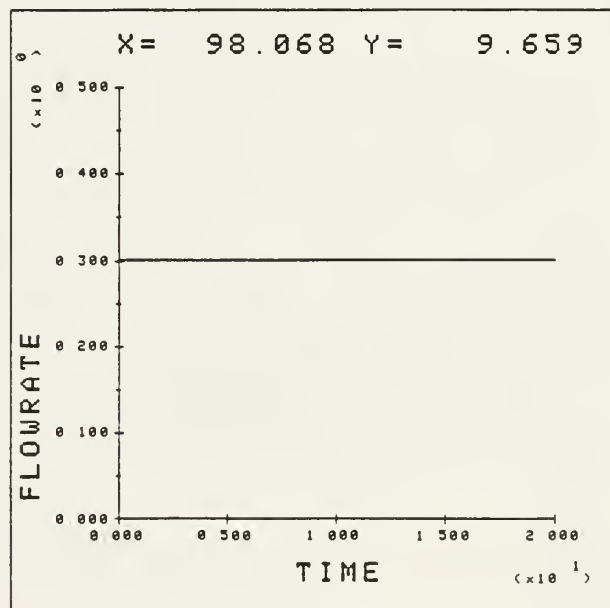


Figure 4.3: Flowrate of output element (problem one)

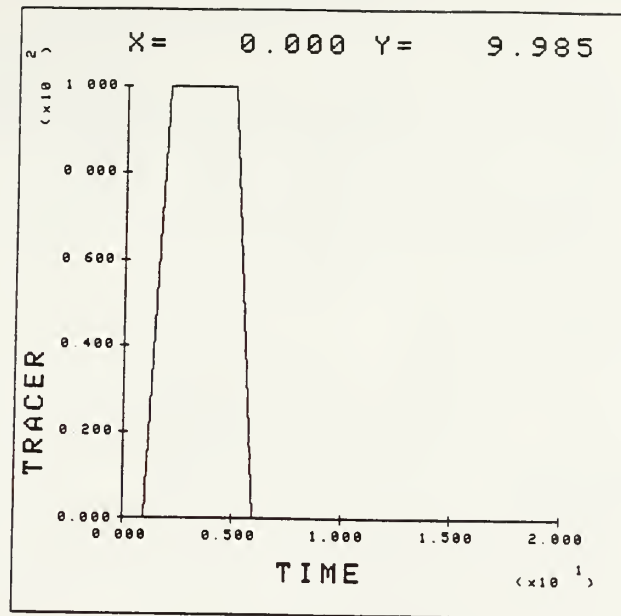


Figure 4.4(a): Tracer at input node (problem one)

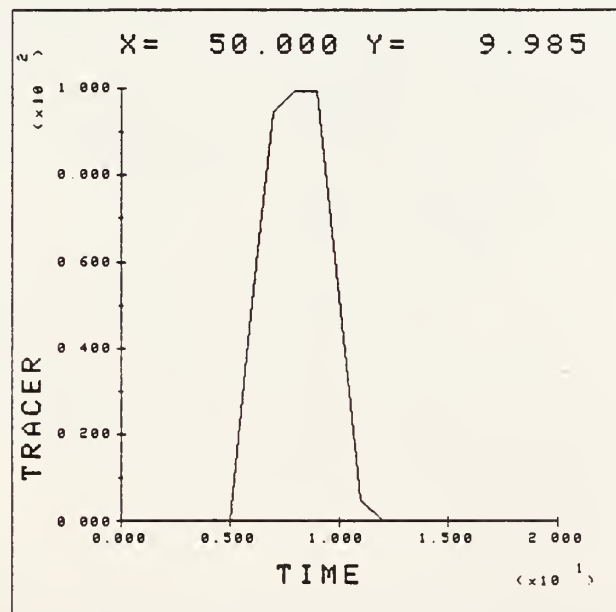


Figure 4.4(b): Tracer at middle of crack (problem one)

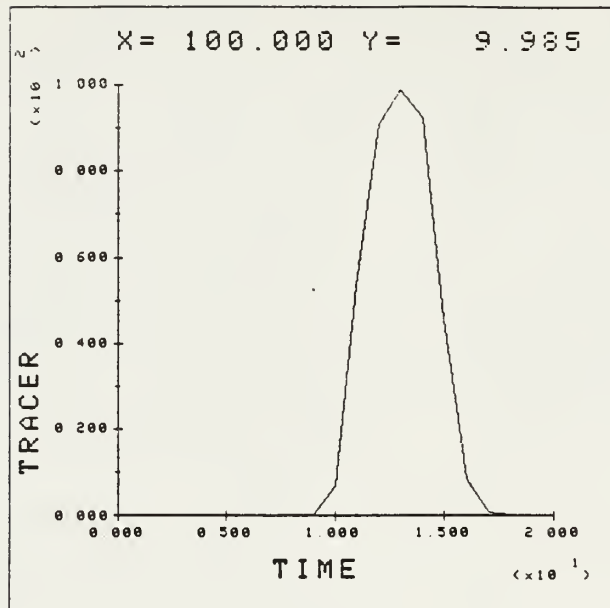


Figure 4.4(c): Tracer at output node (problem one)

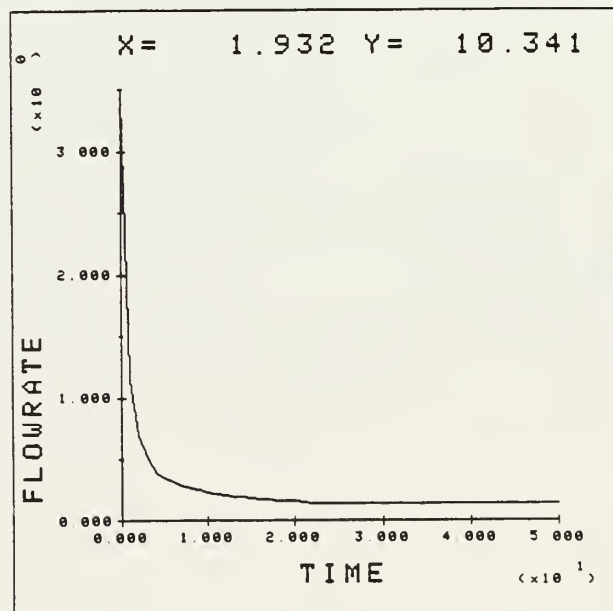


Figure 4.5: Flowrate of input element (problem two)

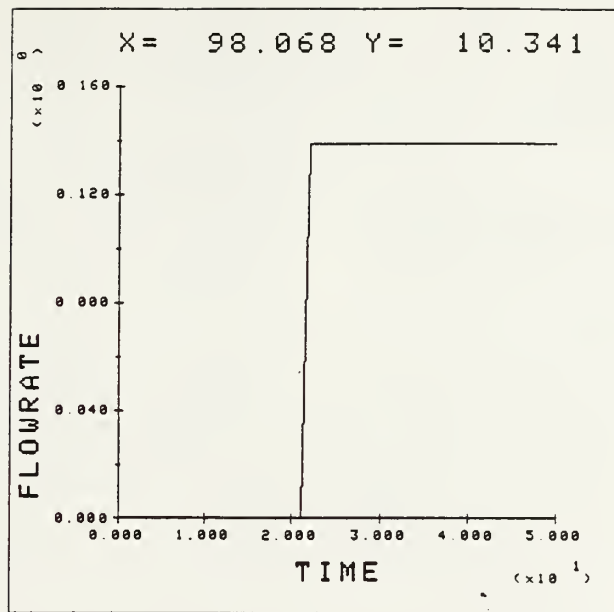


Figure 4.6: Flowrate of output element (problem two)

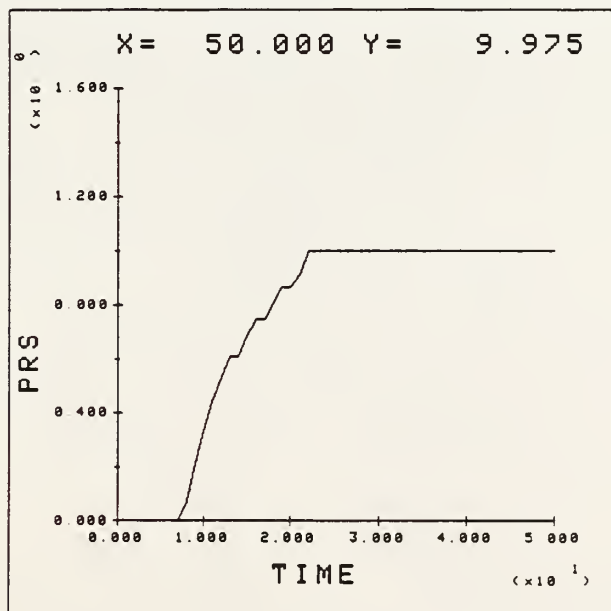


Figure 4.7(a): Pressure at middle of crack (problem two)

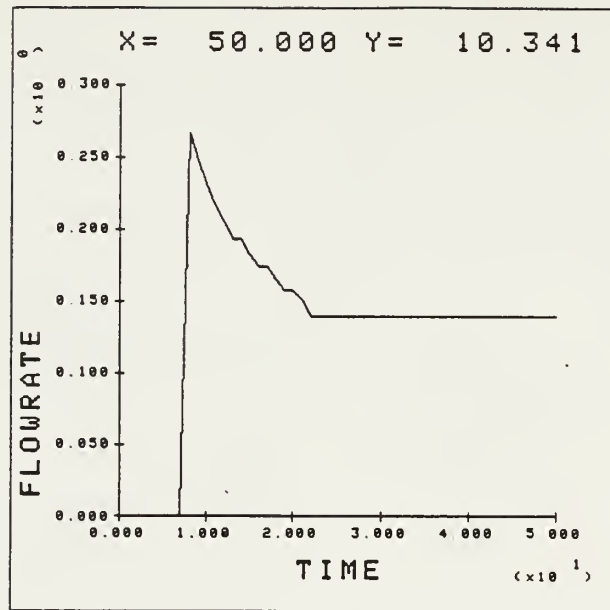


Figure 4.7(b): Flowrate at middle of crack (problem two)

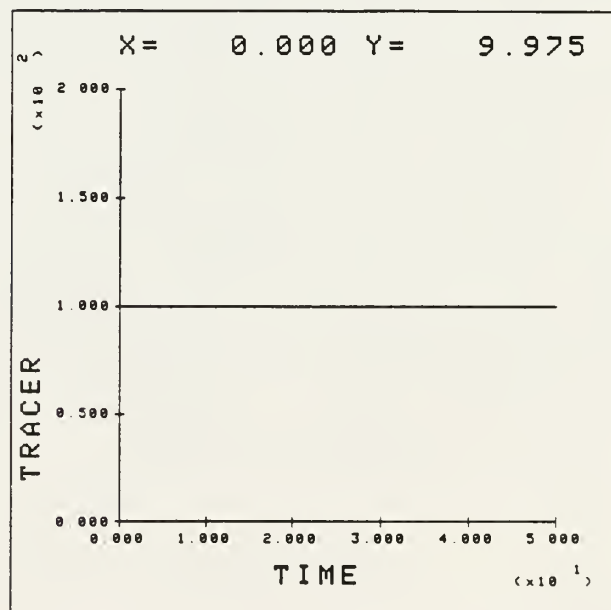


Figure 4.8(a): Tracer at input node (problem two)

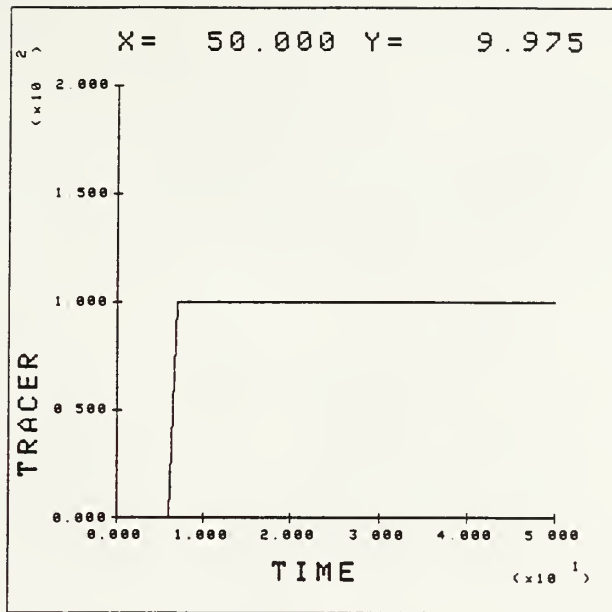


Figure 4.8(b): Tracer at middle of crack (problem two)

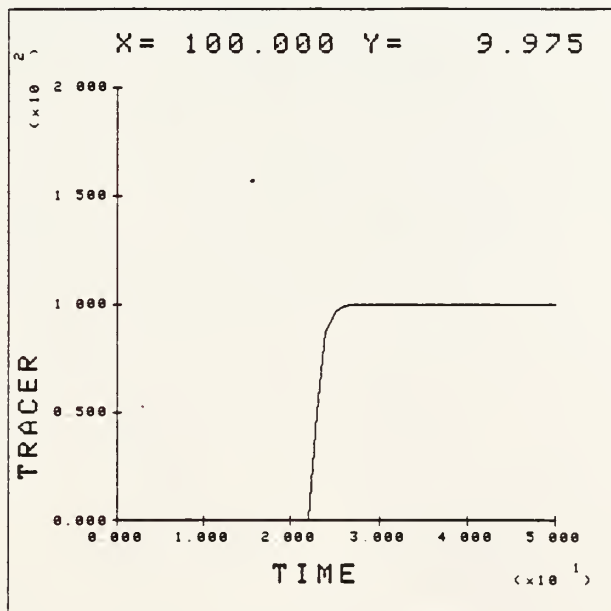


Figure 4.8(c): Tracer at output node (problem two)

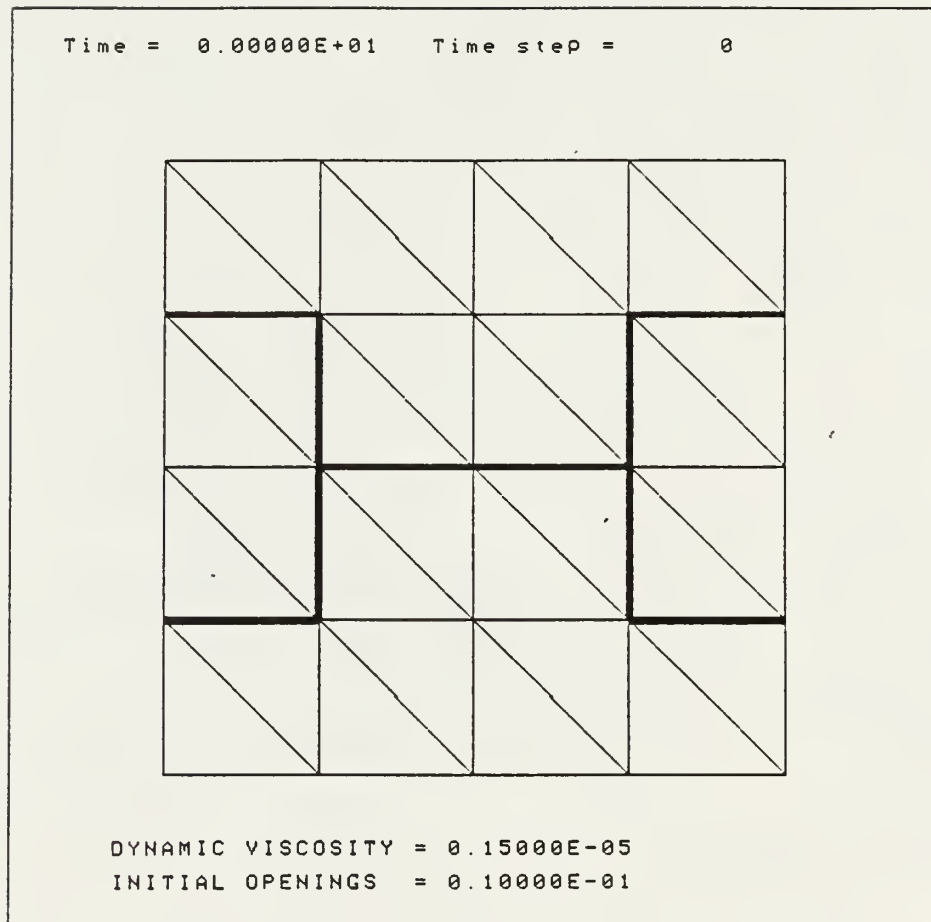


Figure 4.9: Verification problem three

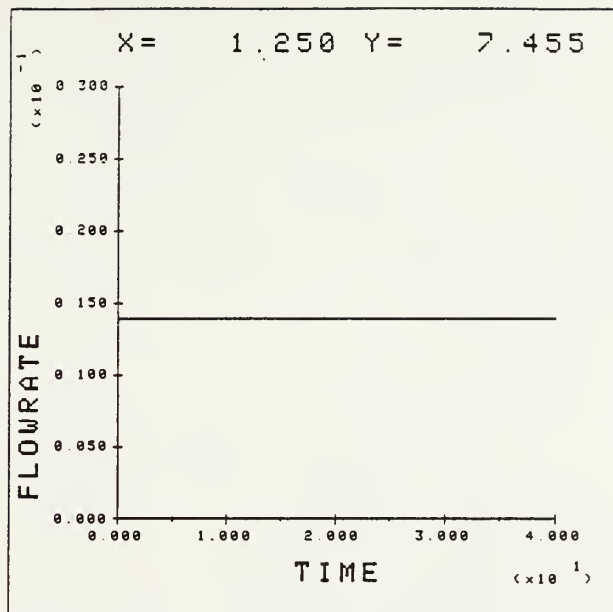


Figure 4.10: Flowrate of input element (problem three)

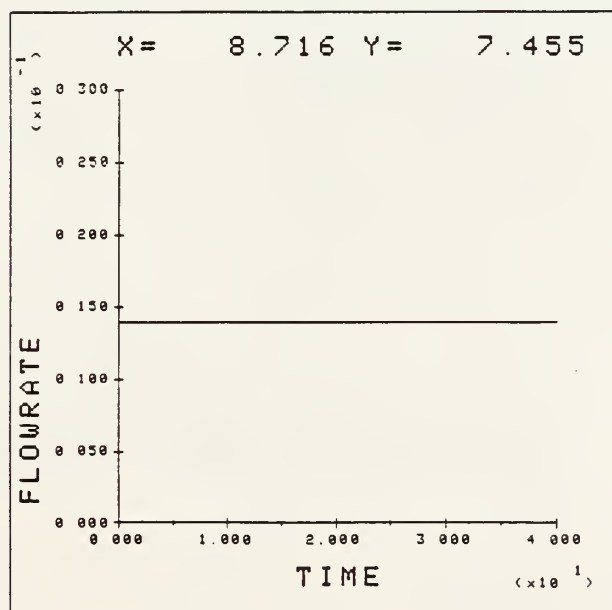


Figure 4.11: Flowrate of output element (problem three)

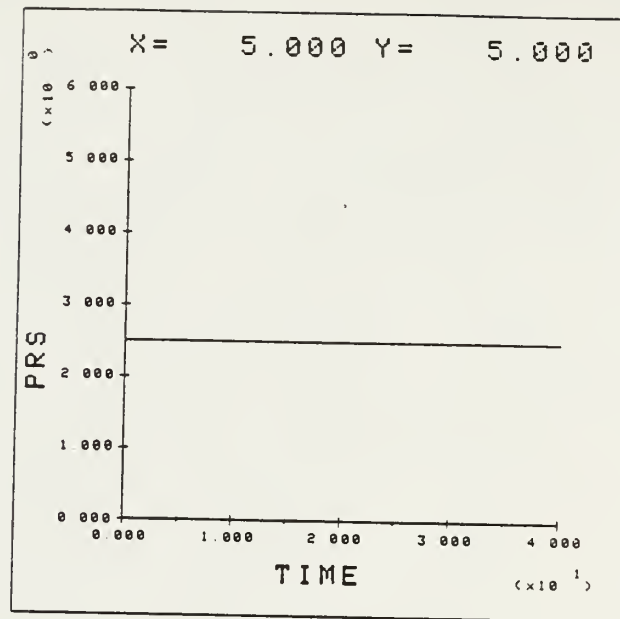


Figure 4.12(a): Pressure at middle of crack (problem three)

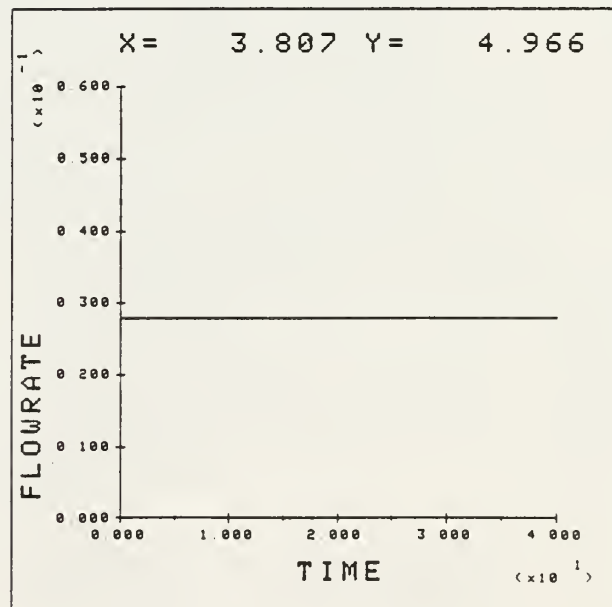


Figure 4.12(b): Flowrate at middle of crack (problem three)

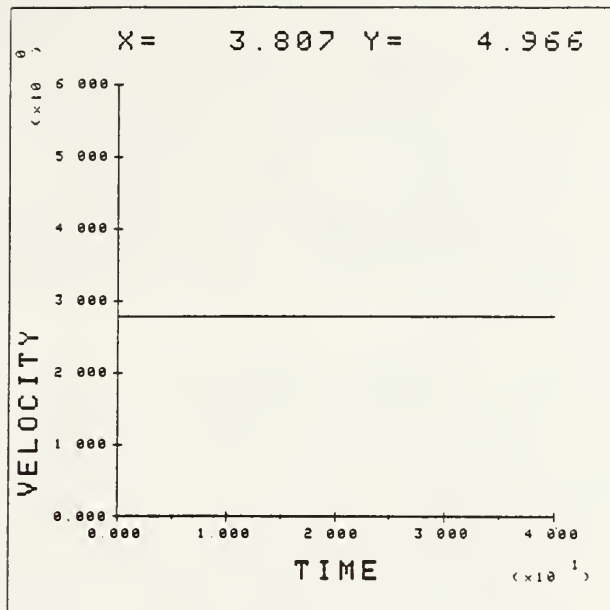


Figure 4.12(c): Velocity at middle of crack (problem three)

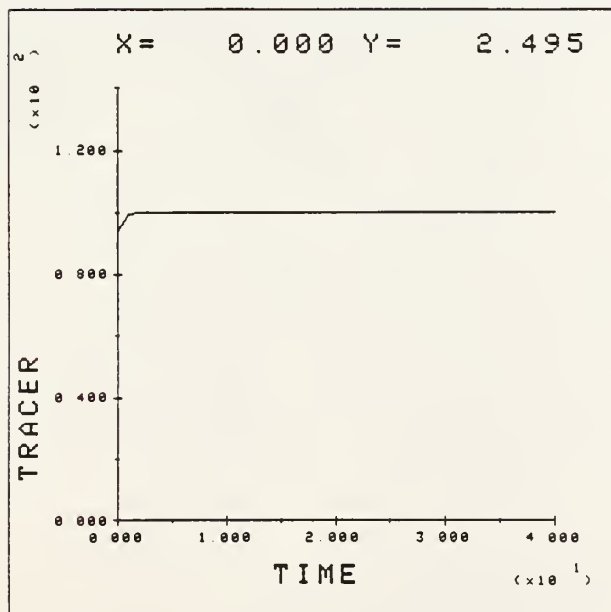


Figure 4.13(a): Tracer at input node (problem three)

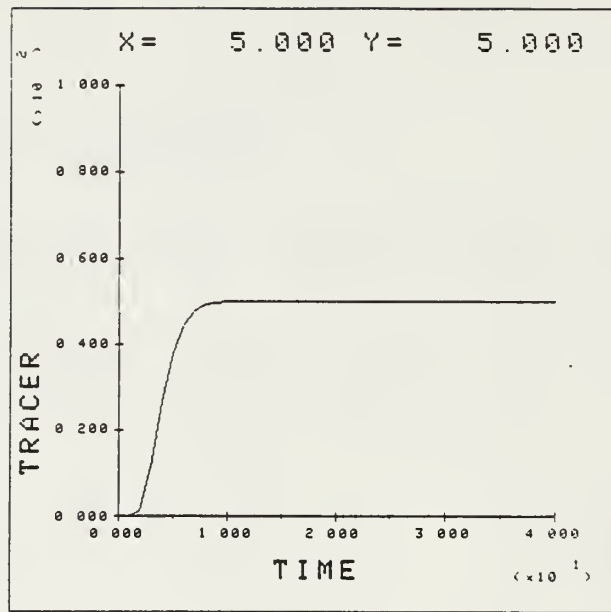


Figure 4.13(b): Tracer at middle of crack (problem three)

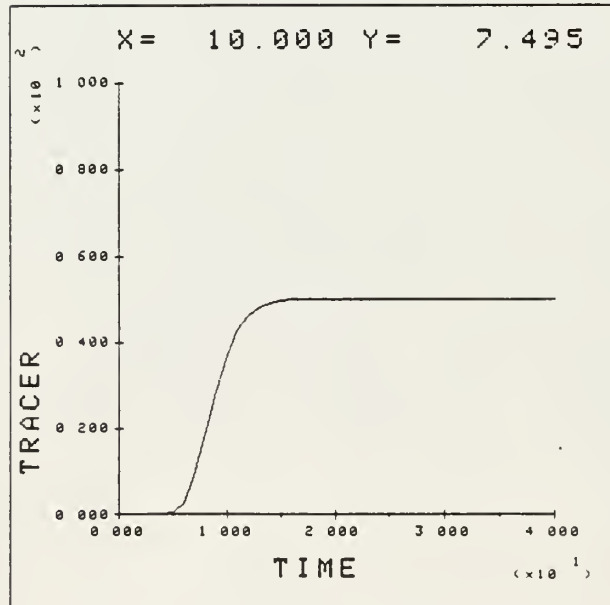


Figure 4.13(c): Tracer at output node (problem three)

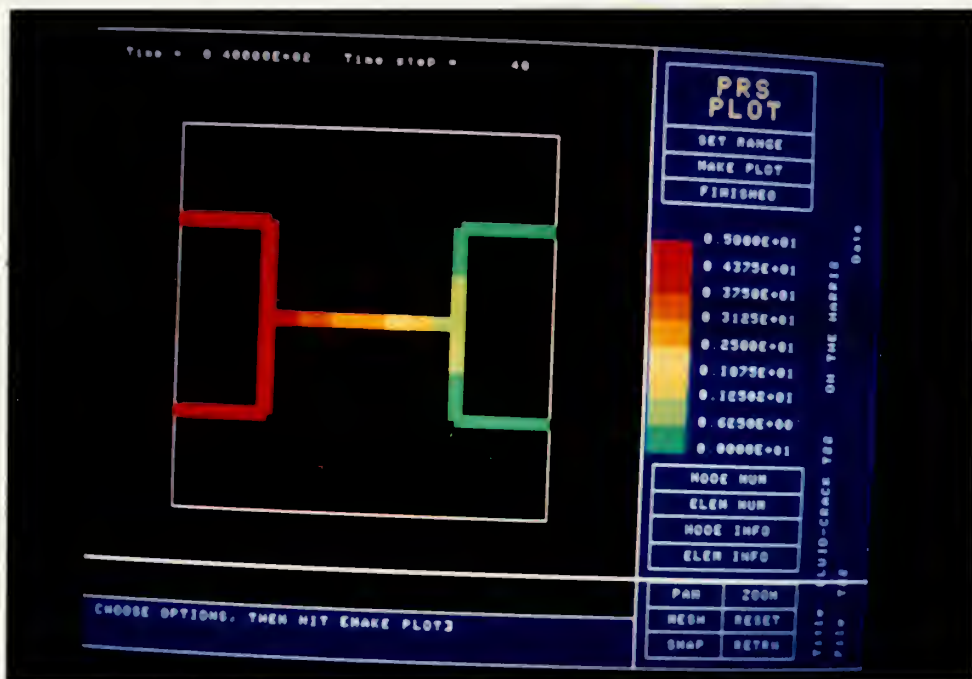


Figure 4.14: Pressure plot of problem three

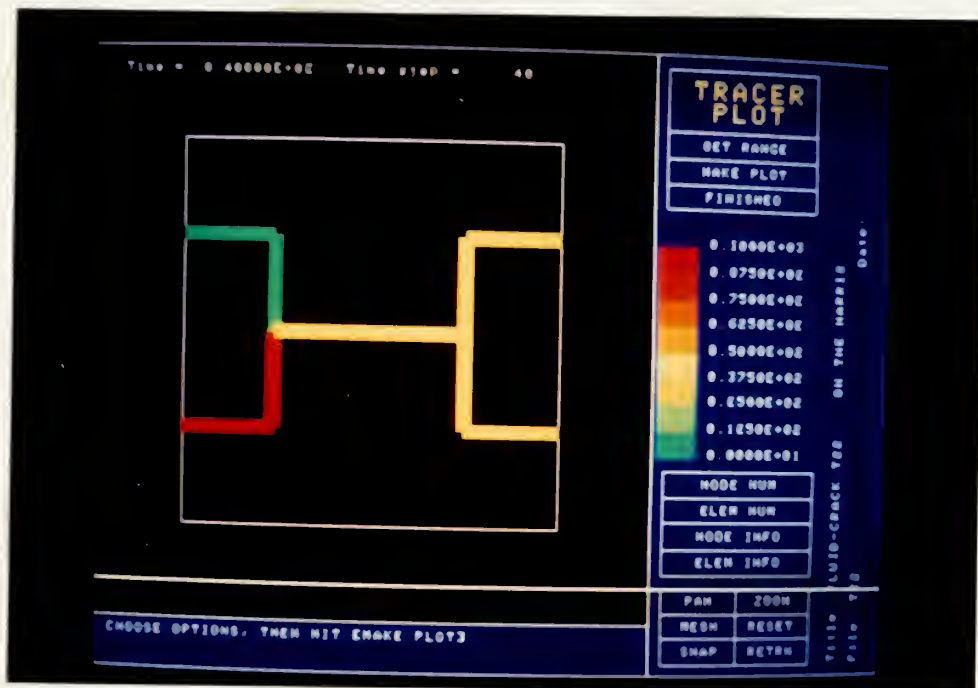


Figure 4.15: Tracer plot of problem three

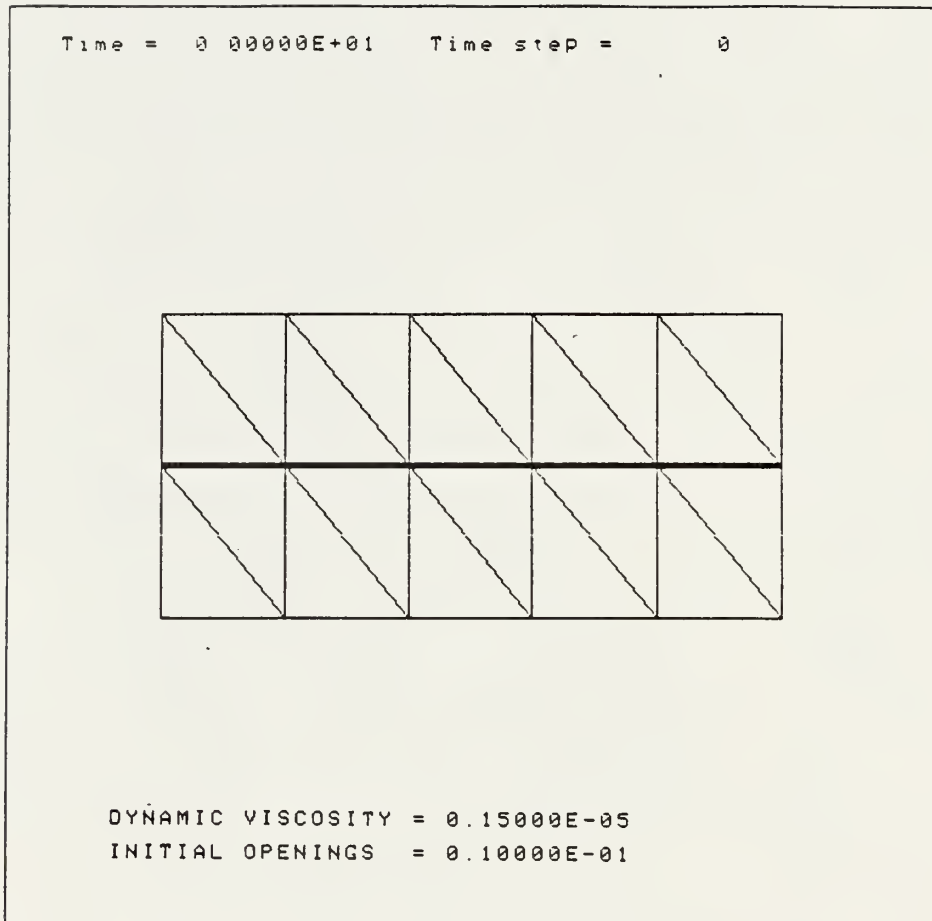


Figure 4.16: Verification problem four

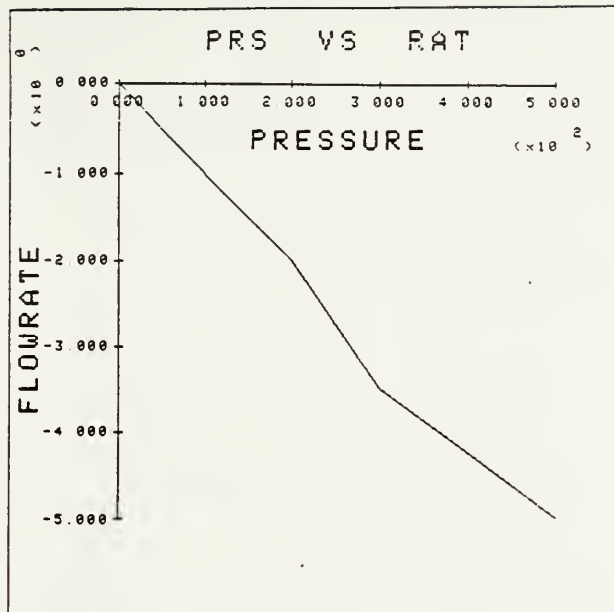


Figure 4.17: Far field boundary condition

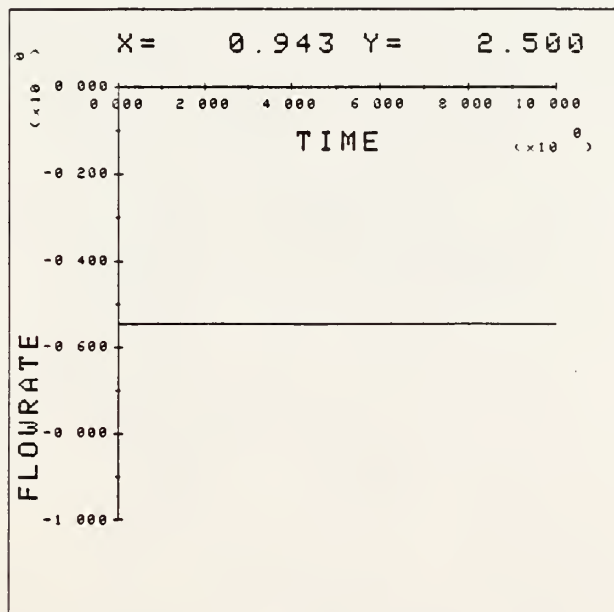


Figure 4.18: Flowrate at left end of fluid element (problem four)

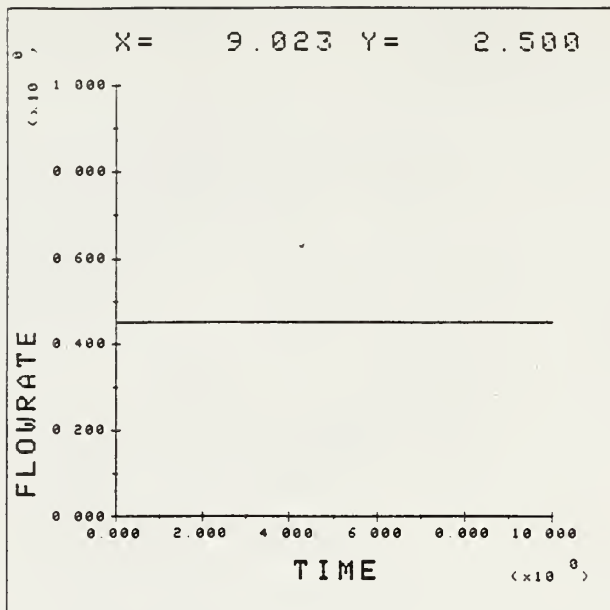


Figure 4.19: Flowrate at right end of fluid element (problem four)

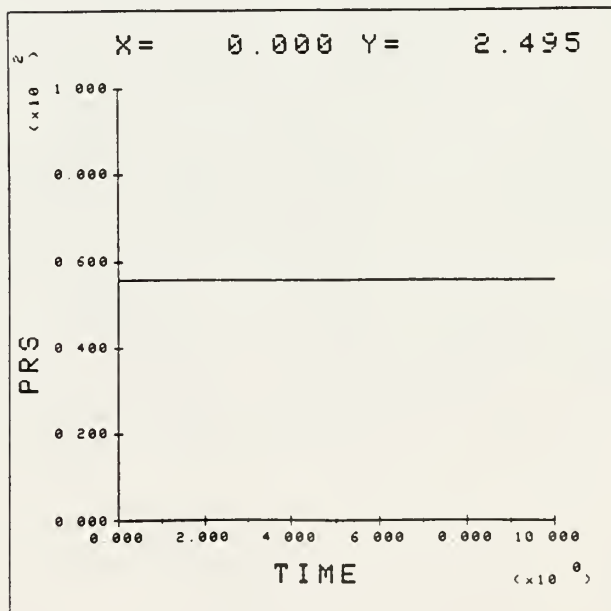


Figure 4.20(a): Pressure at left end (problem four)

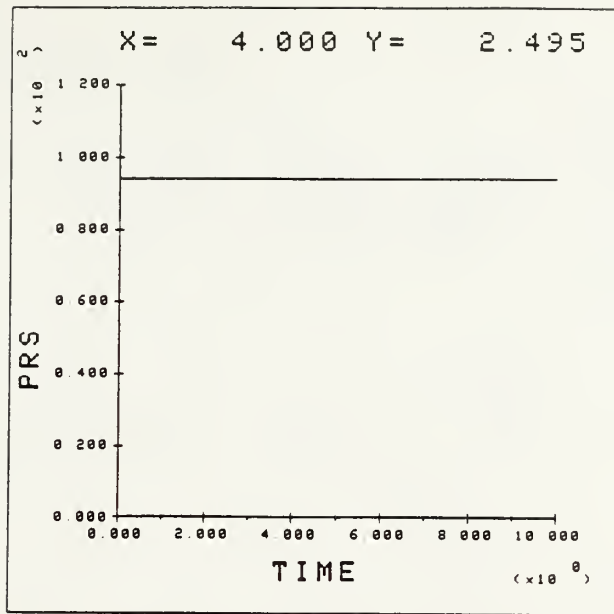


Figure 4.20(b): Pressure at input node (problem four)

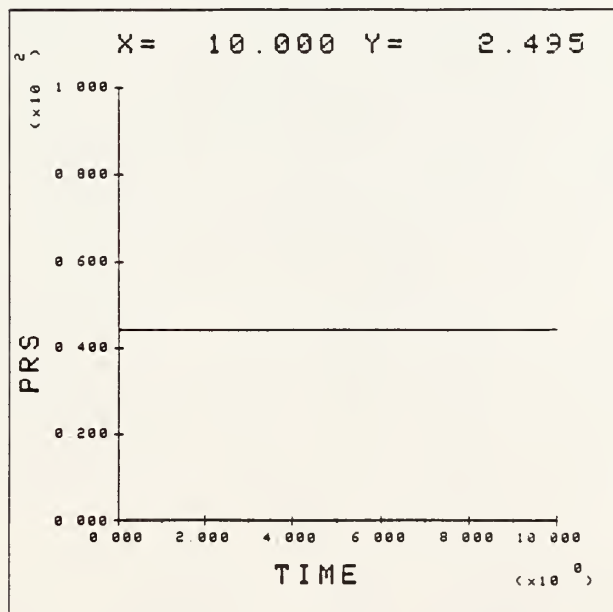


Figure 4.20(c): Pressure at right end (problem four)

CHAPTER V

APPLICATIONS

We analyzed five problems which simulate the Phase II HDR project of Los Alamos national laboratory. Problems one, two, three and four all include 630 fluid elements and 3339 structural nodes. Problem five has 165 fluid elements and 924 solid nodes. Problems one, two and three compare the effect of different far field boundary conditions. All elements are active at the beginning, and there is no flow leakage (problem one) and zero pressures (problem two) in far field. In problem three, a nonlinear pressure/flowrate relation is specified at the far field boundary. In problem four, we examine the effect of an unsymmetric flow path with increased conductivity. The final problem displays the fluid motion in which half of the fluid elements are nonactive initially. The far field conditions of problems three, four and five are all the same, which is shown in Figure 5.14. The input pressure and output pressure are assumed to be $2.034 \times 10^7 \text{ N/m}^2$ (2950 psi) and 0 N/m^2 (0 psi) for all the five application problems, giving the same pressure difference as observed experimentally. Fixing the output pressure at zero helps speed convergence.

The dimensions of Phase II reservoir are about 400 m long and 200 m wide. It is believed, that in a plan view, the joints are spaced at about 10 m horizontally and 10 m vertically. To speed the problem solution, we used a spacing of 20 m between joints. The large joints are assumed to have an opening of 0.004 m and the vertical joints have an opening of 0.0000396 m (Figure 5.2). These values were chosen to

give what we believed to be approximately the correct storage capacity and approximately the observed flowrate. The depth of the flow path between wells is about 100 m and the total flowrate is about $6.3 \times 10^{-3} \text{ m}^3/\text{sec}$ (100 gpm). For one meter depth, the flowrate is $6.3 \times 10^{-5} \text{ m}^3/\text{sec}$ (1 gpm). From the steam tables (Haar and Gallagher, 1984), the dynamic viscosity of water is $1.416 \times 10^{-4} \text{ N}\cdot\text{s}/\text{m}^2$ at 350 bar and 200°C . In our simulation, we included the factor of roughness = 1.5 into the stiffness calculation.

5.1 Problem One - Zero Flow in Far Field

In problem one we assume that there is no leakage in far field.

The input flowrate and output flowrate are both shown in Fig.5.3. After 7500 iterations, the system reached a stable condition and the output flowrate equaled input flowrate at $6.3 \times 10^{-5} \text{ m}^3/\text{sec}$ (1 gpm).

Figure 5.4 shows the pressure at a far field node which has no flow leakage. Figure 5.5 demonstrates the convergence of kinetic energy. Figure 5.6 shows the pressure distribution. The maximum pressure is represented by red and the minimum pressure is represented by green. The pressure decreased from the input node to output node. Figure 5.7 shows the flowrate plot. The arrow indicates the direction of fluid flow. The flowrates of the far field nodes are smaller than 1.0×10^{-11} which approximately equals to zero because of no far field leakage.

5.2 Problem Two - Zero Pressure in Far Field

The only difference between problem one and two is the far field condition. The specified pressure vs flowrate far field boundary condition was chosen to approximate a zero pressure condition. This is shown in Figure 5.8.

Figure 5.9 shows the flow at the input and output wells. The input flowrate is approximately three times the flowrate of problem one due to reduced resistance, because of the added flow paths to the far field. The output flowrate is only 1/4th the output flowrate of problem one, since, due to far field leakage, most flow does not reach the output node.

The pressure and the leakage flowrate at a far field node are shown in Figure 5.10. The pressure is approximately zero. Figure 5.11 shows the convergence of kinetic energy.

Figure 5.12 shows the pressure distribution. Far field pressures are approximately zero. The flowrate plot is shown in Figure 5.13. The arrows of flowrates in far field elements point outward which indicates flow leakage in far field.

5.3 Problem Three - Nonlinear Pressure/Flowrate in Far Field

Problem one and two examined the extremes in far field behavior - zero flow or zero pressure. In reality, it is expected that some leakage occurs, but that the leakage is pressure dependant. We examined this situation by specifying a nonlinear pressure/flowrate relation at the far field boundaries (Figure 5.14). This relation resulted in leakage flow at about one third of the far field nodes.

Flowrates at the input node and output nodes are shown in Figure 5.15. The input flowrate is slightly large than the flowrate

for problem one, which had no leakage. The output flowrate is about $3/4$ of the input, so about one fourth of the flow leaks to the far field. The pressure at a far field node which has no flow leakage is shown in Figure 5.16.

Tracer was pumped into the crack system from time 1×10^5 secs to 9×10^5 secs. The motion of the tracer is shown in Figure 5.17. Diffusion of the pulse occurs between the input and output. We believe that most of this is realistic due to mixing of tracer in the open joints. In addition, the multiple flow paths effectively diffuse the tracer pulse.

Kinetic energy during convergence is displayed in Figure 5.18. Figure 5.19 and Figure 5.20 show the pressures plot and flowrates. Figure 5.21 shows the velocity plot. This clearly indicates the slower flow velocities in the larger joints. In Fig.5.20 and Fig.5.21, the arrows of fluid flow in far field show $1/3$ of far field nodes leak due to the nonlinear relation of pressure vs flowrate.

The tracer motion is shown in Figure 5.22 at three different time steps. The tracer spread into more fluid elements through time history. Because we only pumped the tracer into the well from time 0×10^5 to 9×10^5 sec, Figure 5.22(c) shows that at time 15×10^5 sec the zero concentration of tracer has spread from the input area.

5.4 Problem Four - Reduced Resistance Flow Path

In problem three, we examined flow for a perfectly symmetric situation. In reality, one might expect that there will be preferred flow paths of lower resistance between the wells, in addition to the

more uniform flow paths. We examined this situation in problem four by adding a third material with an gap opening of 0.0000792 m. Eight elements which previously were material type one were changed to material type three. Material type three has twice the gap opening of material type one (Figure 5.23). These eight elements construct a "bridge" between input node and output node which allows fluid flow pass more easily.

Figures 5.24(a) and (b) show the input flowrate and output flowrate. The flow is increased over problem three due to the decreased resistance of the bridge. Because of the nonlinear pressure vs flowrate relation in far field, the leakage of fluid flow causes the output flowrate to be less than the input flowrate.

The motion of tracer is shown in Figure 5.25. The existence of the "bridge" causes the tracer to move faster from input node to output node through the "bridge". Due to the dilution of fluid, the concentration of tracer at the output place is very low at the beginning and then gradually increases. Figure 5.26 shows the kinetic energy plot.

Figure 5.27 shows the pressure plot and Figure 5.28 shows the flowrate plot. The velocity plot is shown in Figure 5.29. Figure 5.28 and 5.29 show clearly the low resistance bridge between input node and output nodes.

The motion of the tracer is shown in Figure 5.30 at three different time steps. The tracer follows the low resistance flow path from input node to output node through time history.

5.5 Problem Five - Initially Empty Fractures

In this problem, we used a spacing of 40 m horizontally and 40 m vertically. The larger joints are assumed to have an opening of 0.008 m (Figure 5.32(a)) and the vertical joints have an opening of 0.00005 m (Figure 5.32(b)). These values were chosen to give approximately the correct storage capacity and approximately the observed flowrate. It is assumed that elements of material type one (Figure 5.32(a)) are active and that of material type two (Figure 5.32(b)) are nonactive initially, except for those elements which connect to the input and output nodes which are assumed to be active.

One time step is specified as 40000 seconds (11.1 hours) which is less than the time that need to fill a empty element. According to the result, it took 640000 seconds (7.5 days) for fluid to travel from the input node to output node. This clearly indicates that the assumed gap of the open joints was too large.

Figure 5.33(a) and (b) show the input flowrate and output flowrate. The output flowrate is less than the input flowrate because of the far field leakage.

Figure 5.34 through Figure 5.36 give pressure and flowrate plots at three different time steps. At each time step, we see that more fluid elements fill with fluid and become active. Because of the nonlinear pressure vs flowrate relation, some far field nodes leak, as shown in Figure 5.36(b).

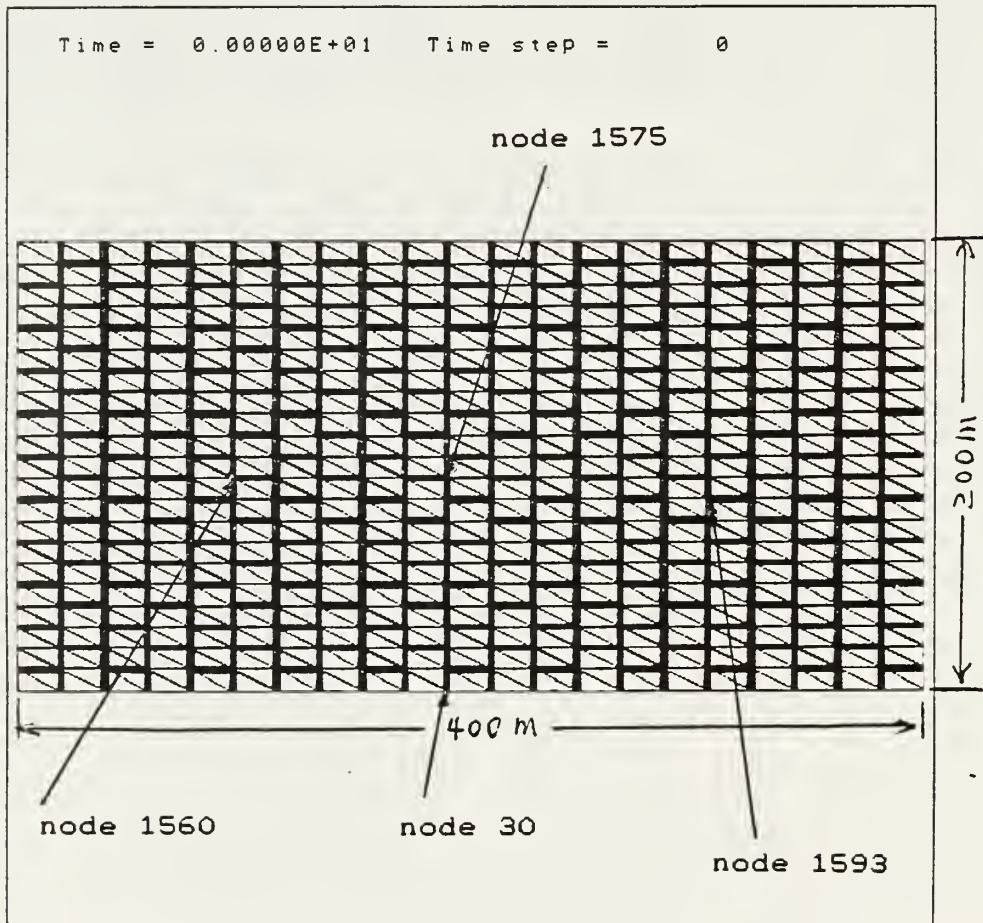


Figure 5.1: Mesh plot of application problem one

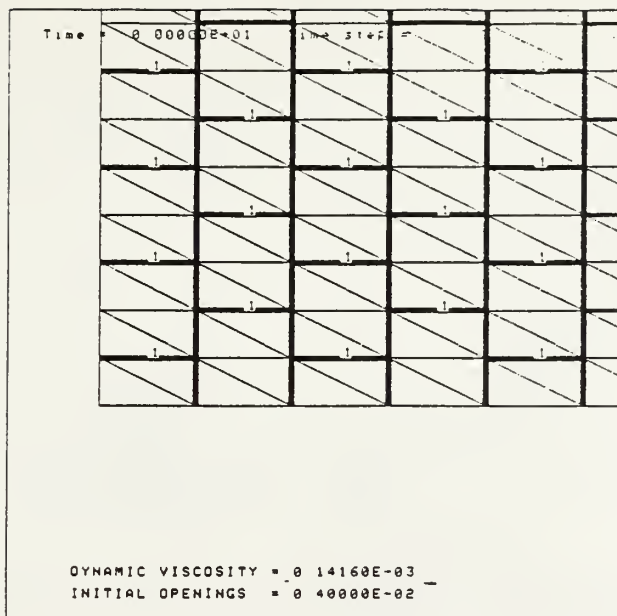


Figure 5.2(a): Material property of material type one

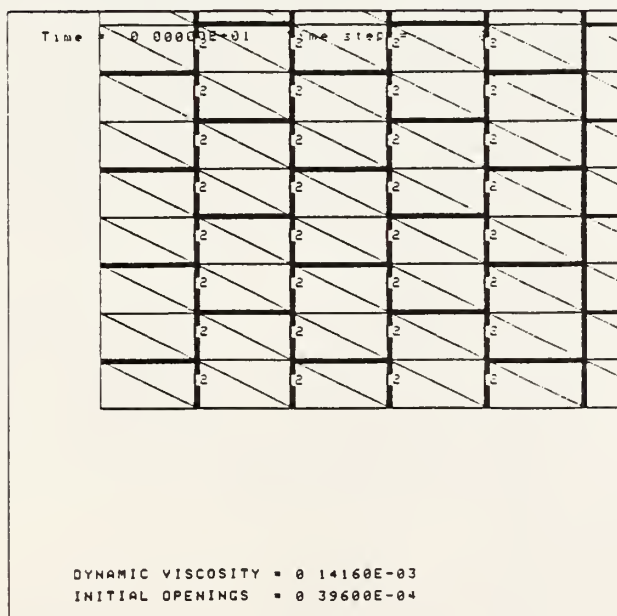


Figure 5.2(b): Material property of material type two

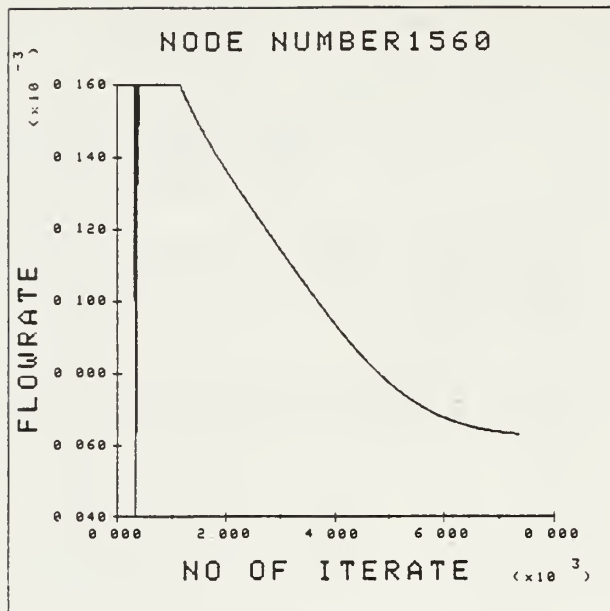


Figure 5.3(a): Flowrate at input node

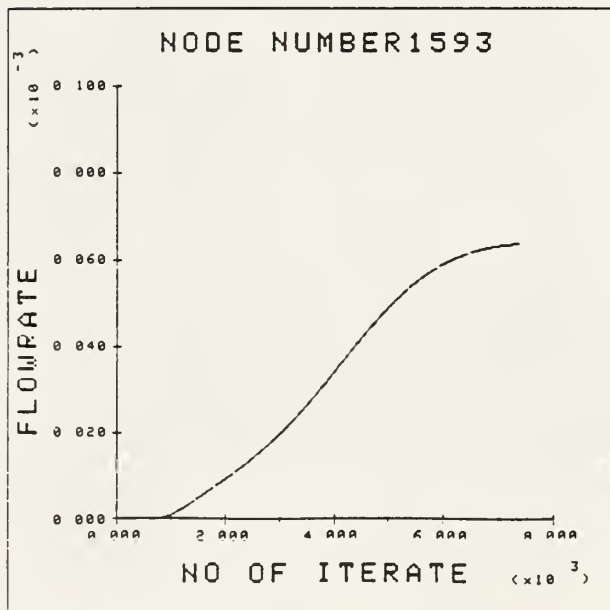


Figure 5.3(b): Flowrate at output node

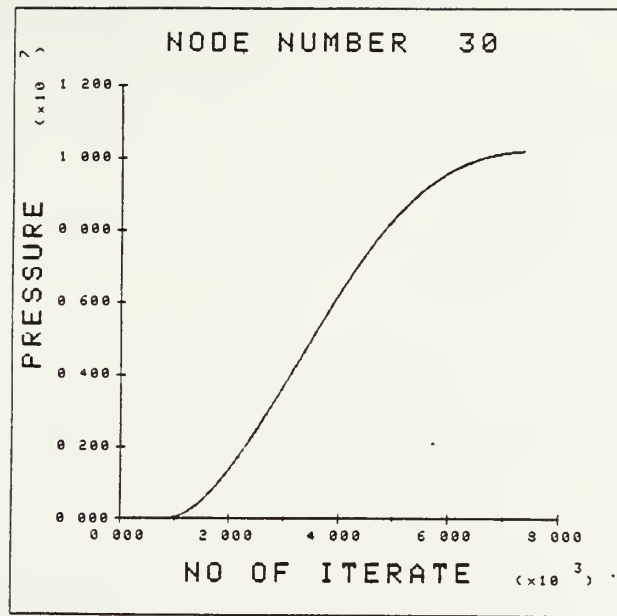


Figure 5.4: The pressure of a far field node No.30

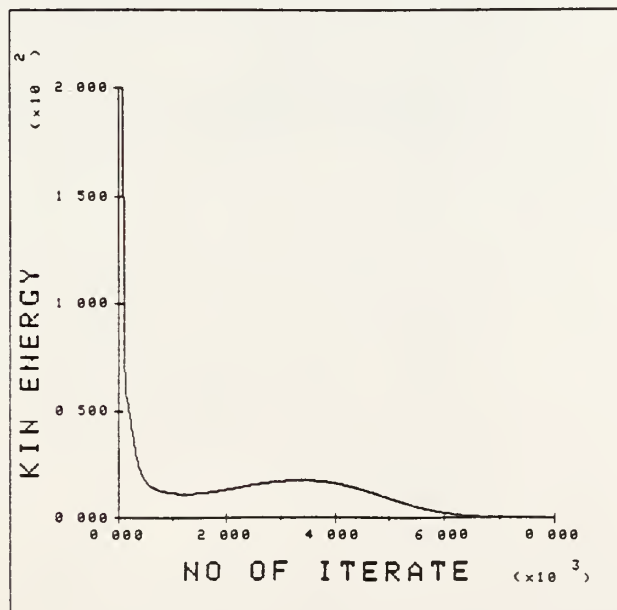


Figure 5.5: Kinetic Energy vs No of Iteration plot

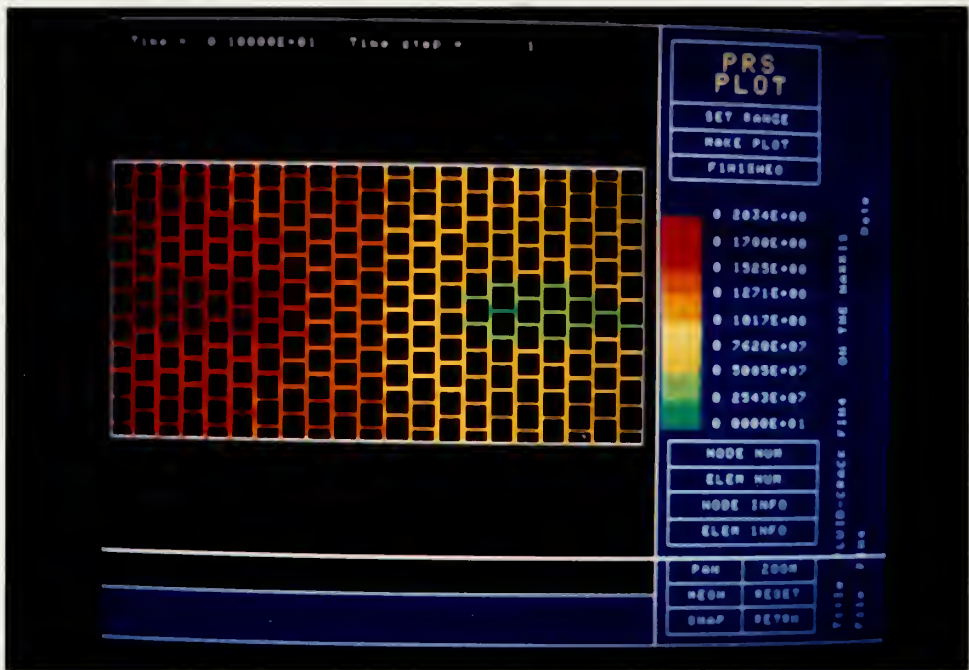


Figure 5.6: Pressure plot of application problem one

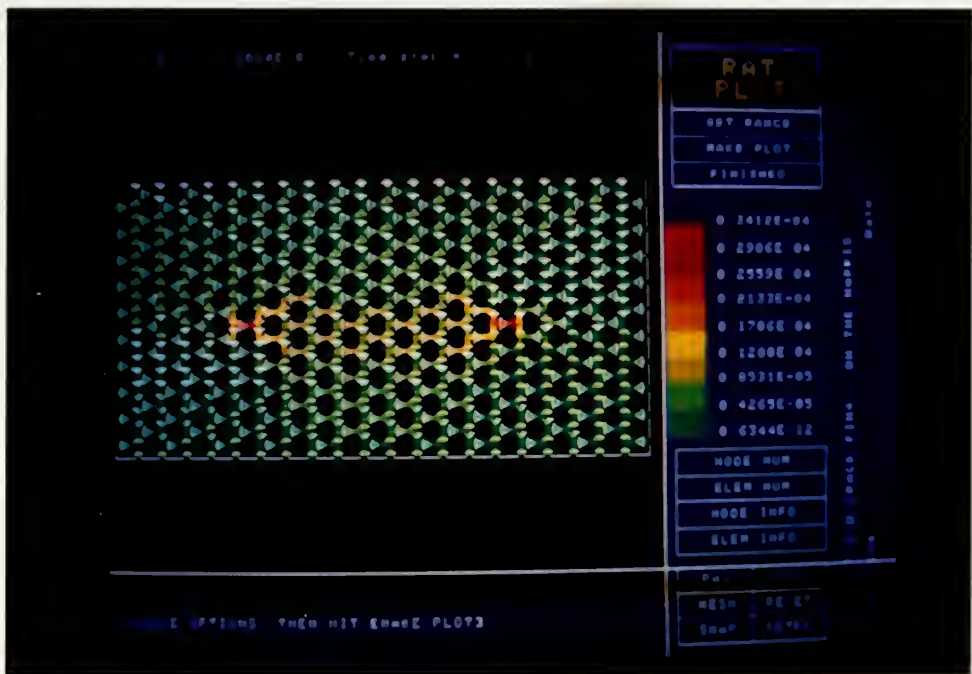


Figure 5.7: Flowrate plot of application problem one

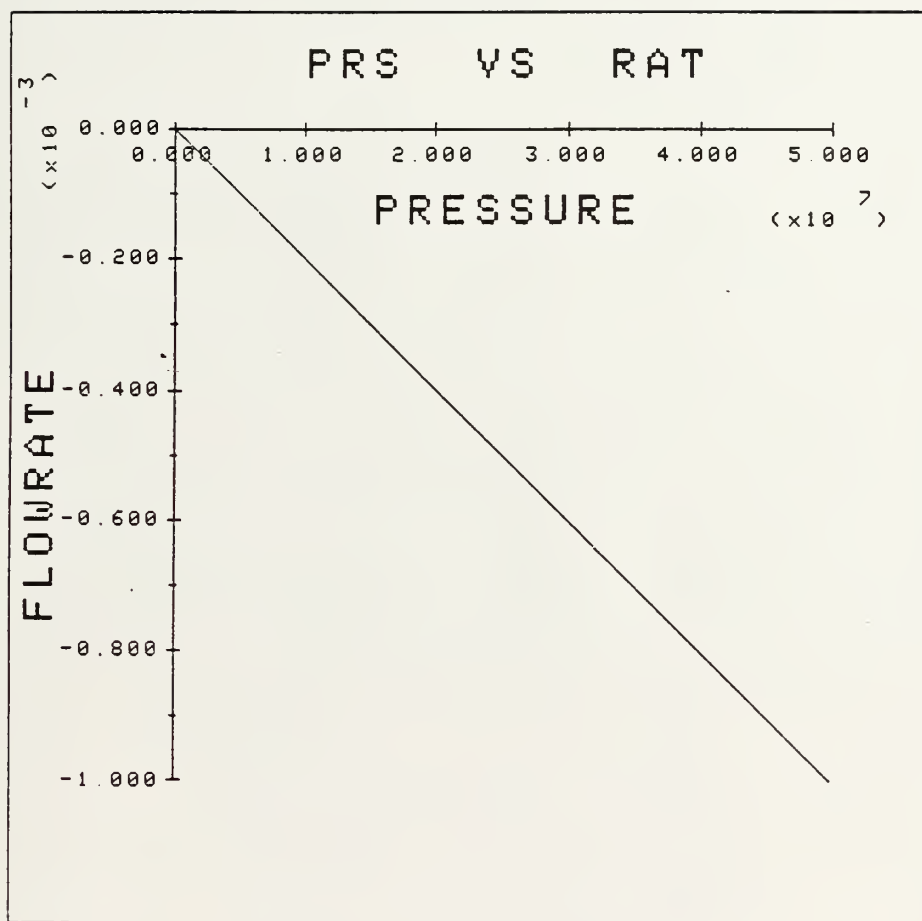


Figure 5.8: Far field condition of application problem two

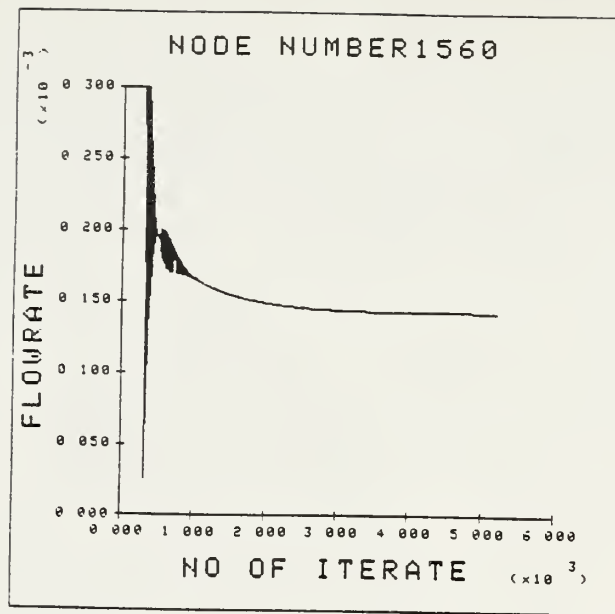


Figure 5.9(a): The input flowrate of application problem two

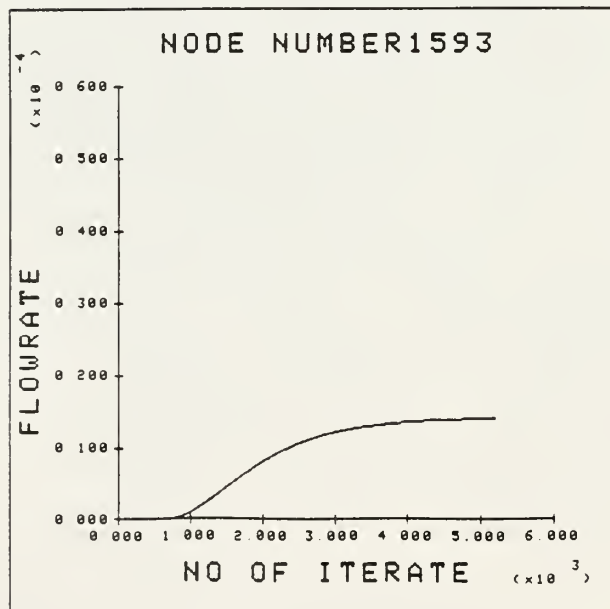


Figure 5.9(b): The output flowrate of application problem two

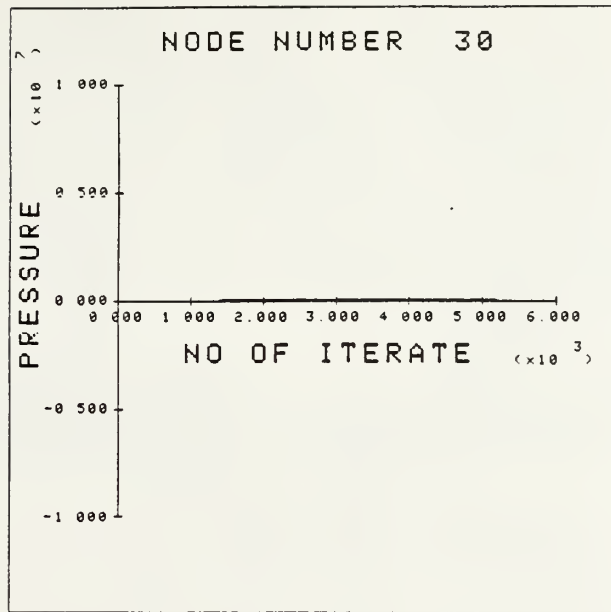


Figure 5.10(a): The pressure at a far field node No.30

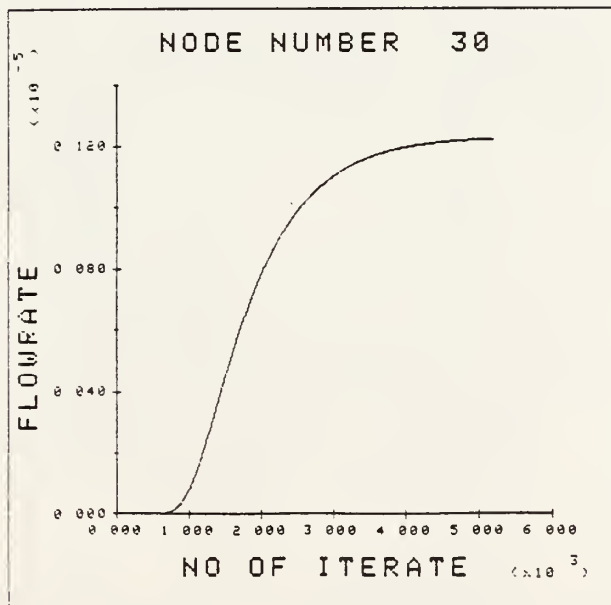


Figure 5.10(b): The flowrate at a far field node No.30 .

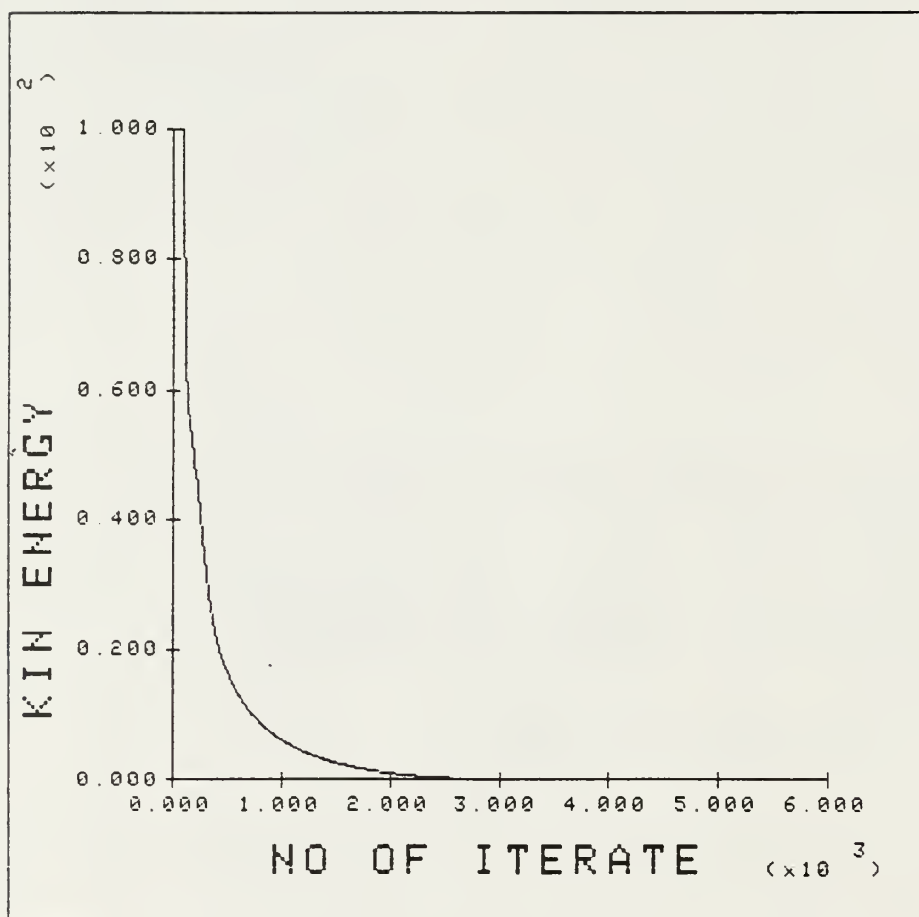
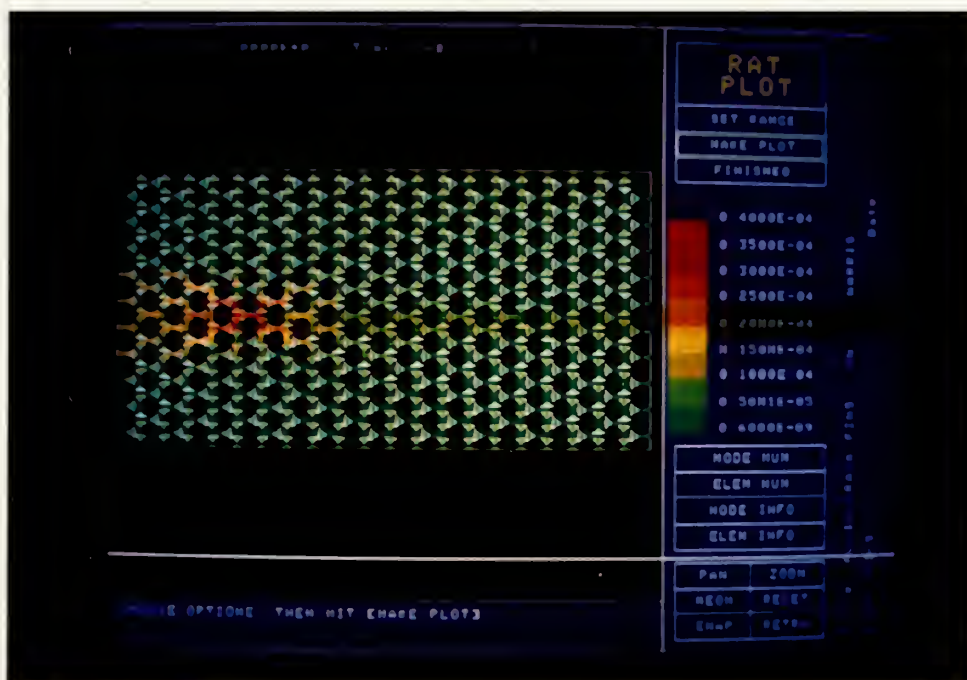
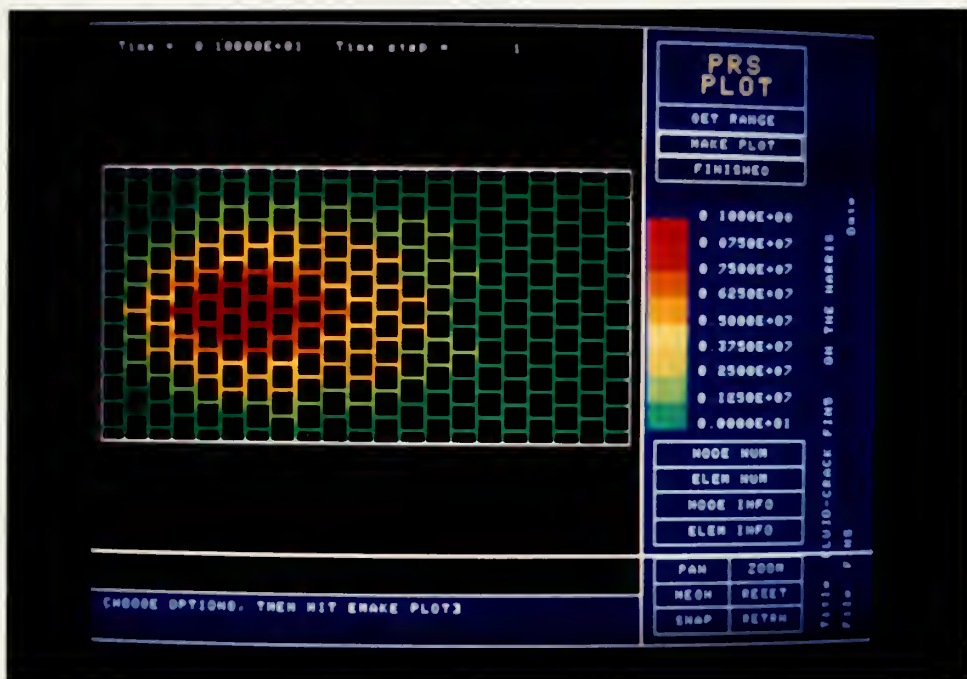


Figure 5.11: Kinetic Energy vs No of Iteration plot



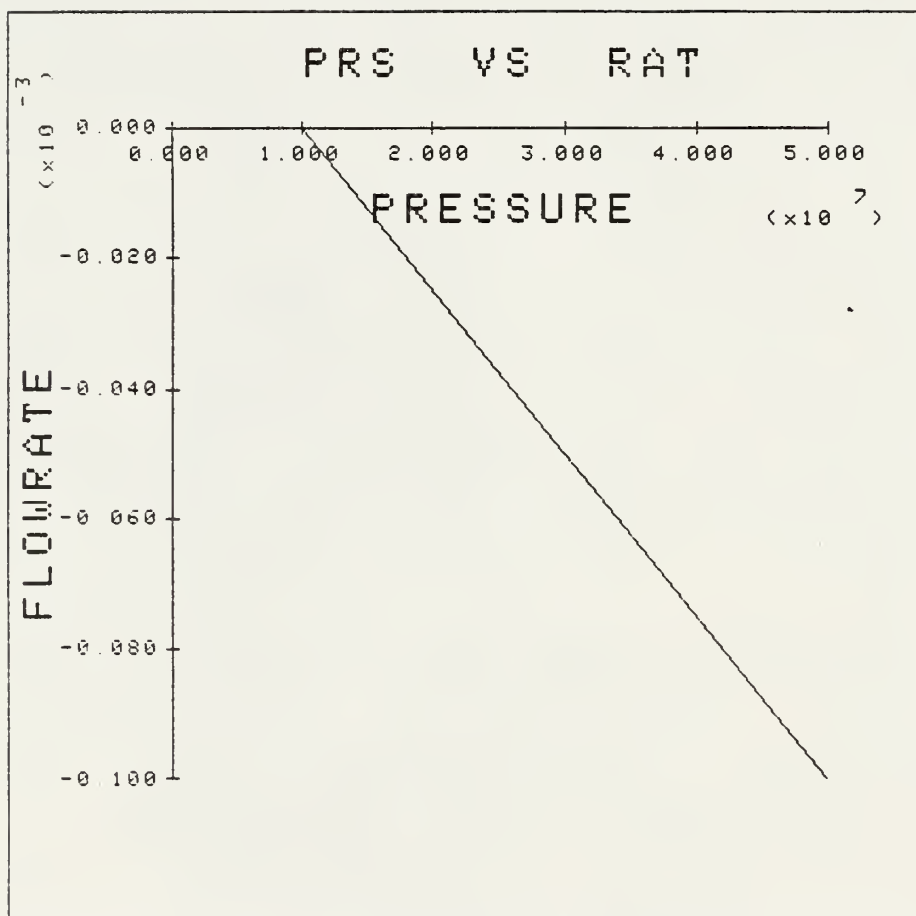


Figure 5.14: Far field condition of application problem three

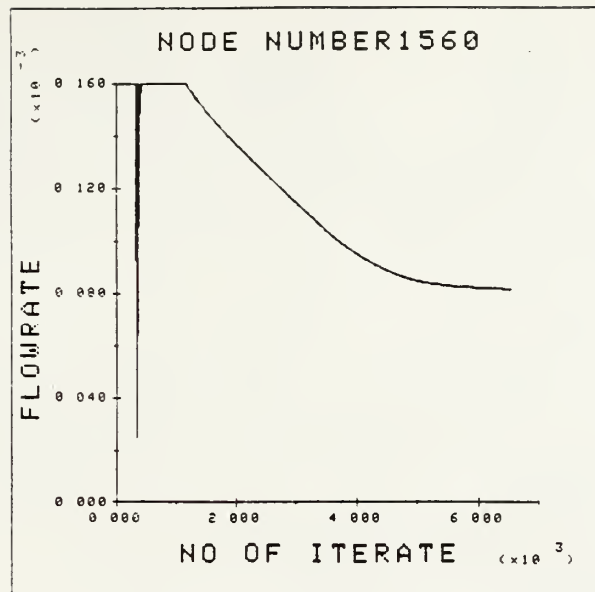


Figure 5.15(a): Flowrate at input node (problem three)

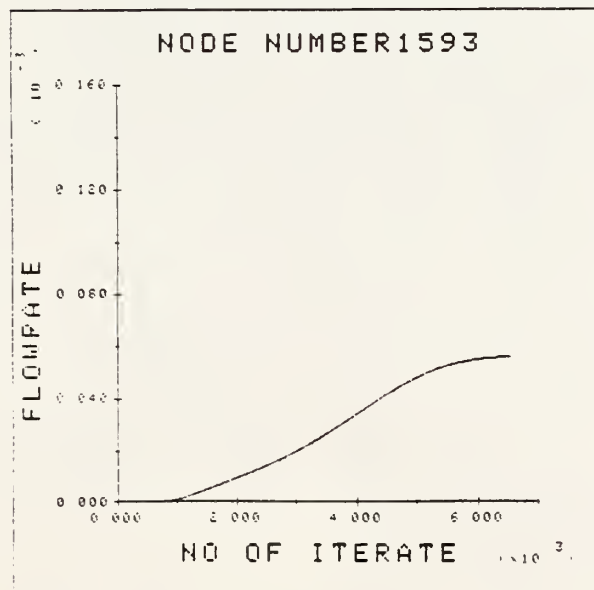


Figure 5.15(b): Flowrate at output node (problem three)

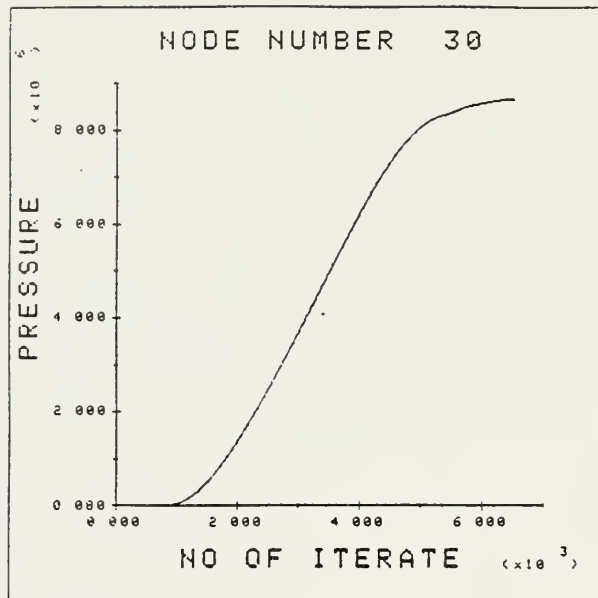


Figure 5.16: Pressure at a far field node No.30 which has no flow leakage

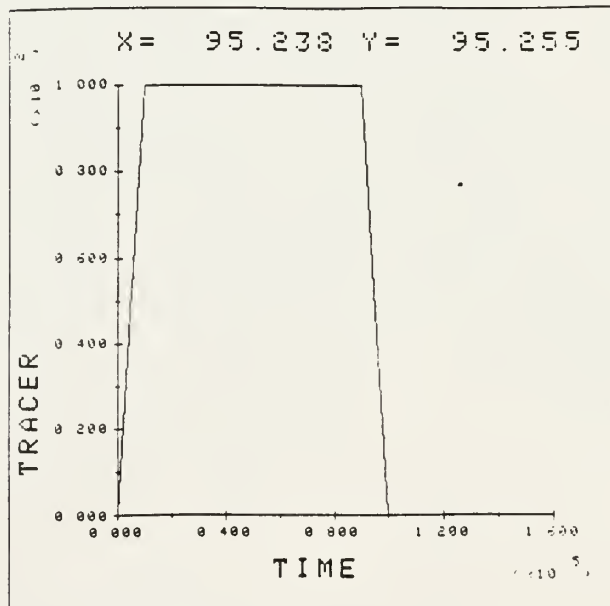


Figure 5.17(a): Tracer at input node (problem three)

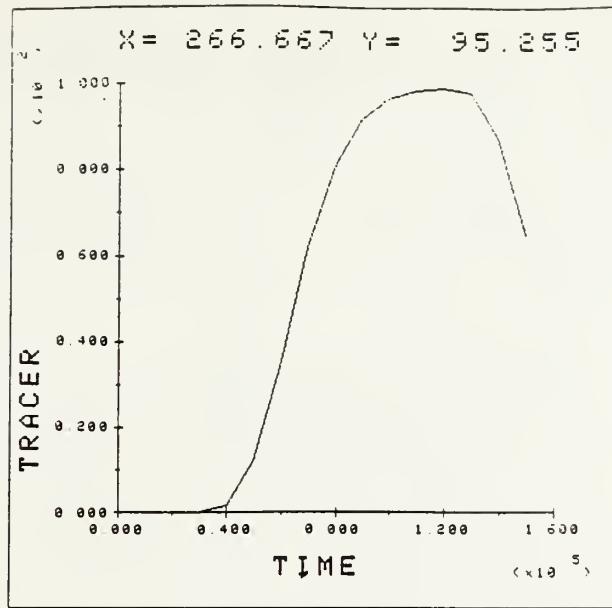


Figure 5.17(b): Tracer at middle of crack (problem three)

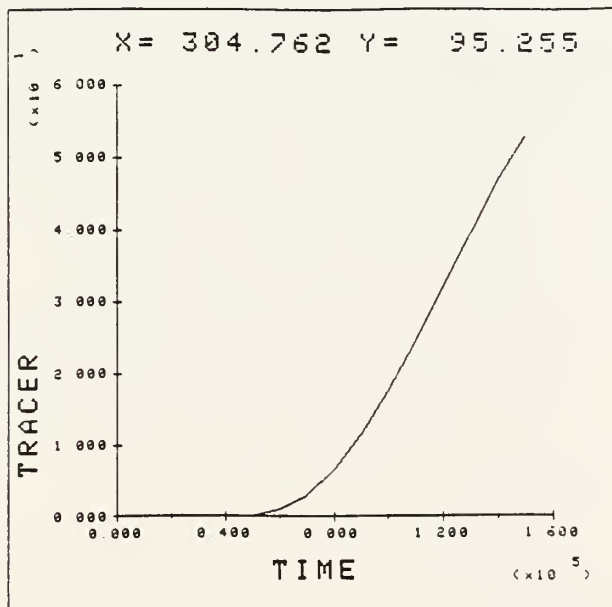


Figure 5.17(c): Tracer at output node (problem three)

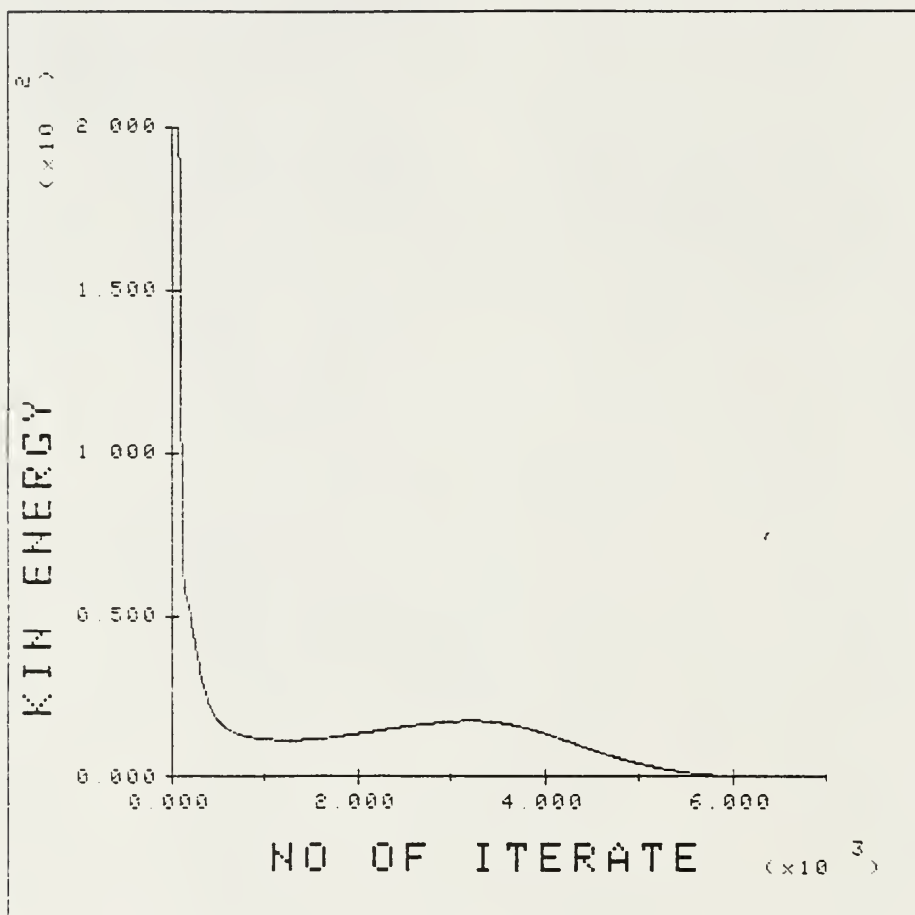


Figure 5.18: Kinetic Energy vs No of Iteration plot



Figure 5.19: Pressure plot of application problem three

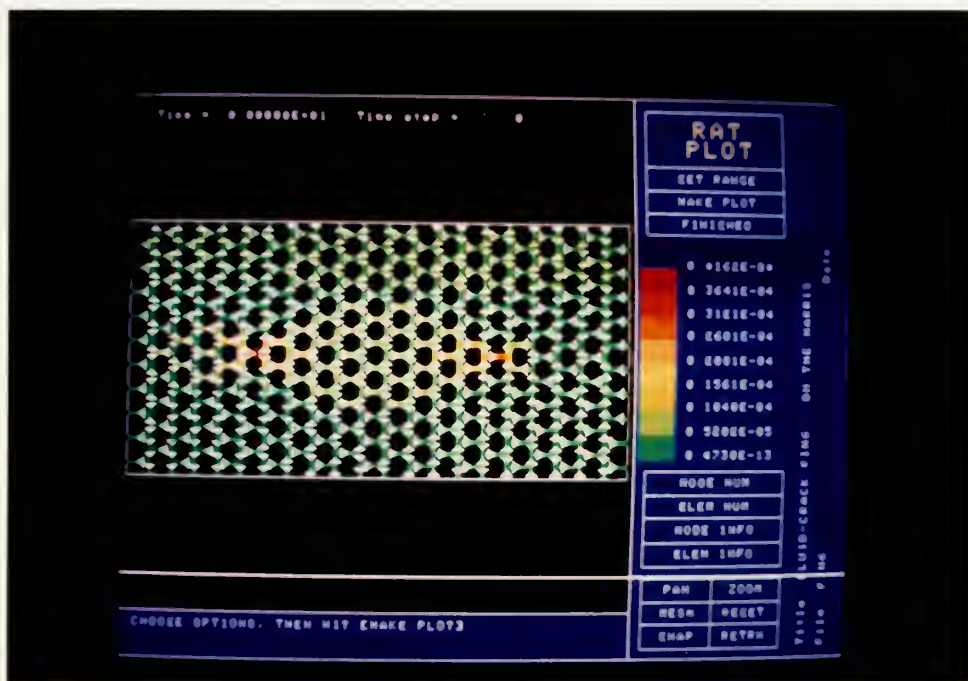


Figure 5.20: Flowrate plot of application problem three

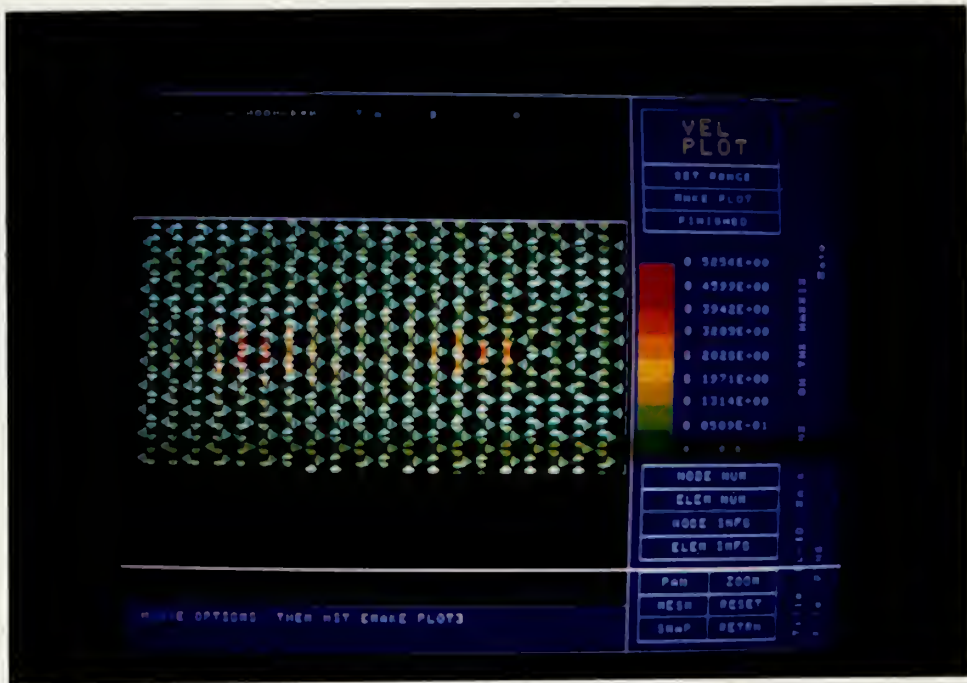


Figure 5.21: Velocity plot of application problem three

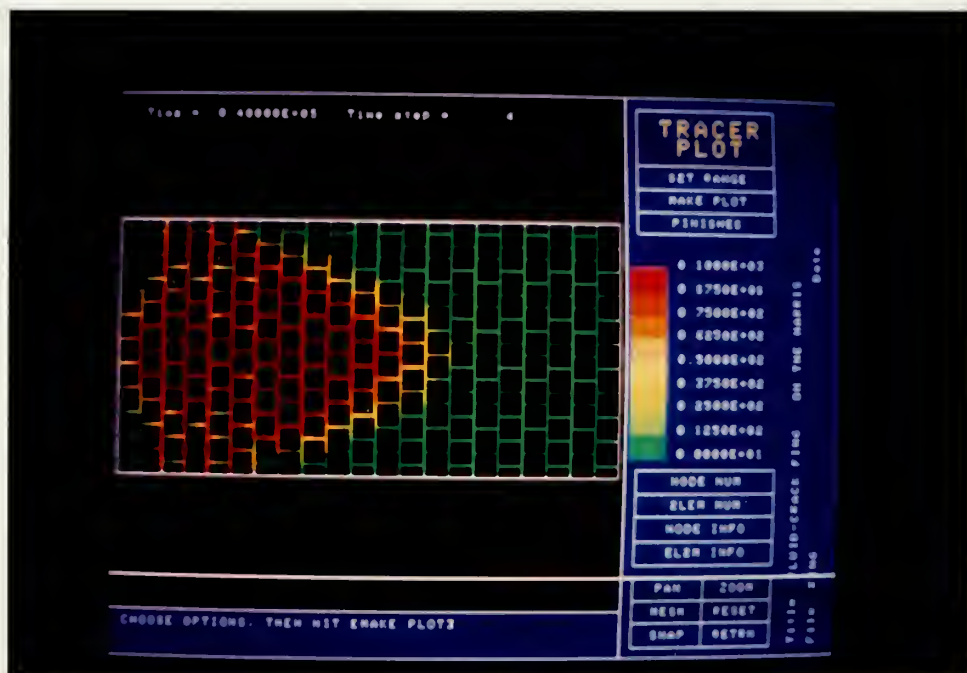


Figure 5.22(a): Tracer plot at 4×10^4 seconds

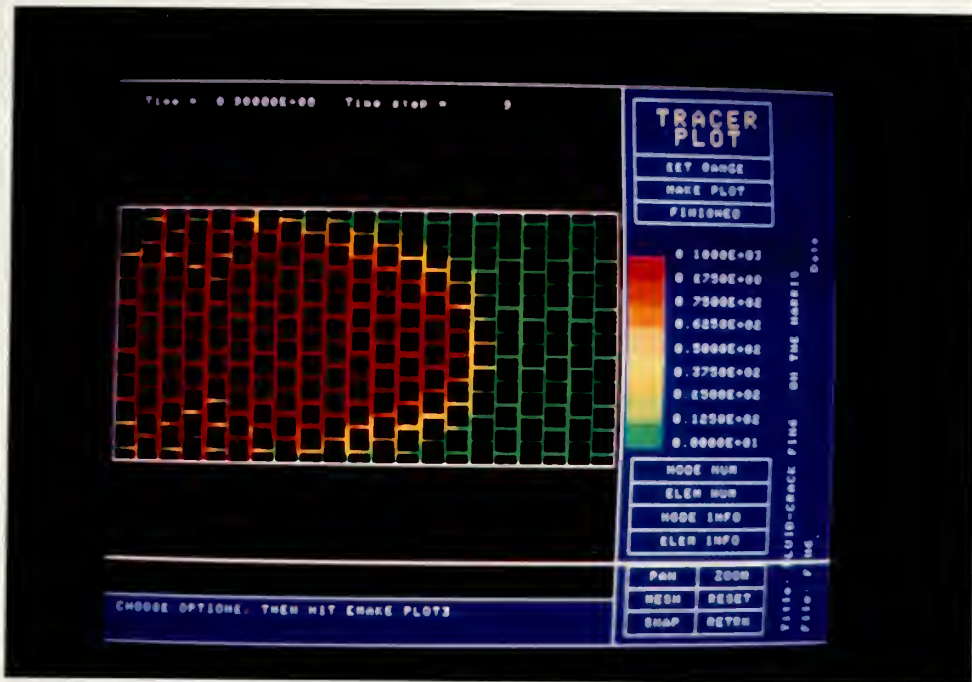


Figure 5.22(b): Tracer plot at 9×10^4 seconds

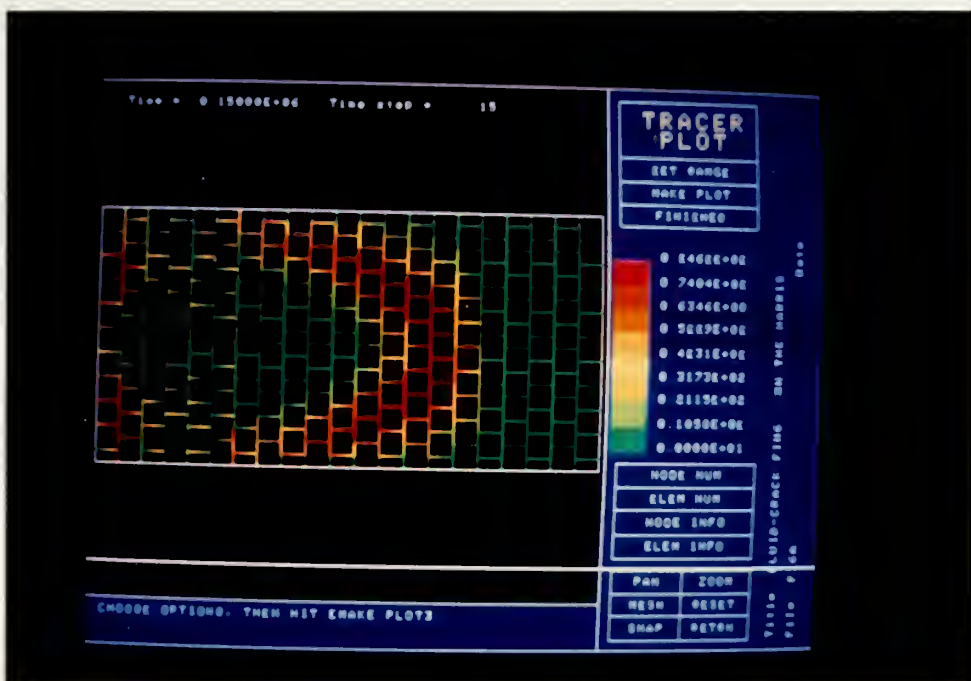


Figure 5.22(c): Tracer plot at 1.5×10^5 seconds

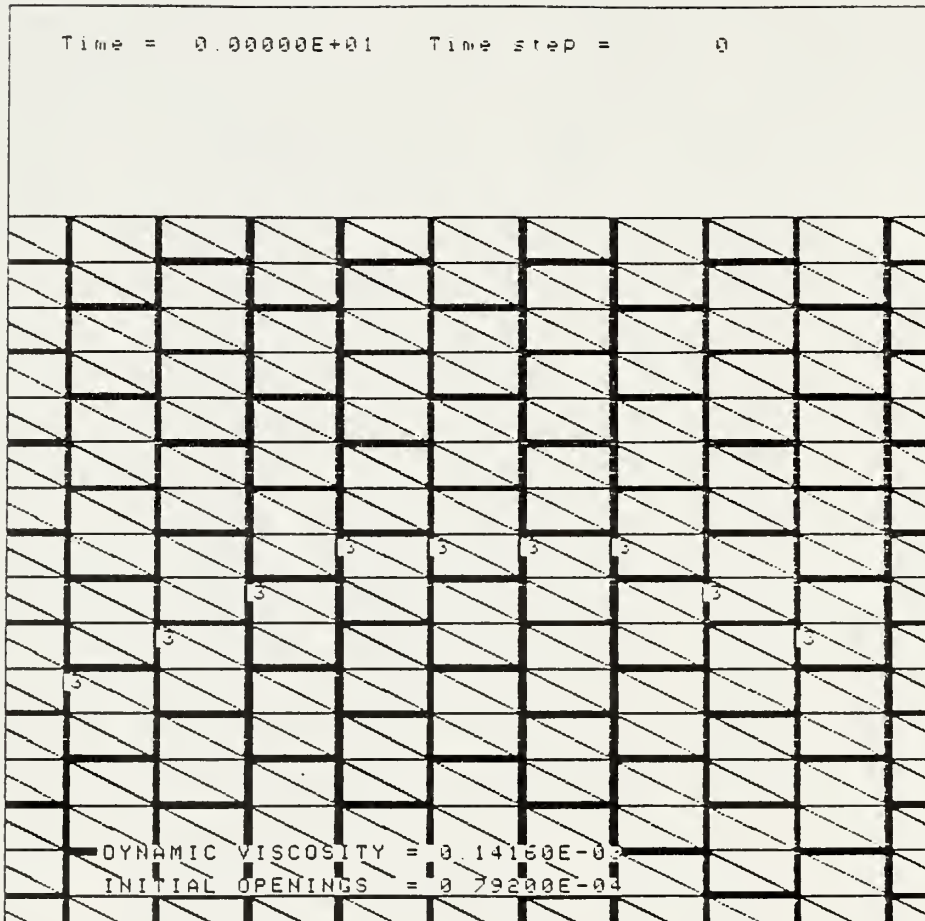


Figure 5.23: Material property of material type three (problem four)

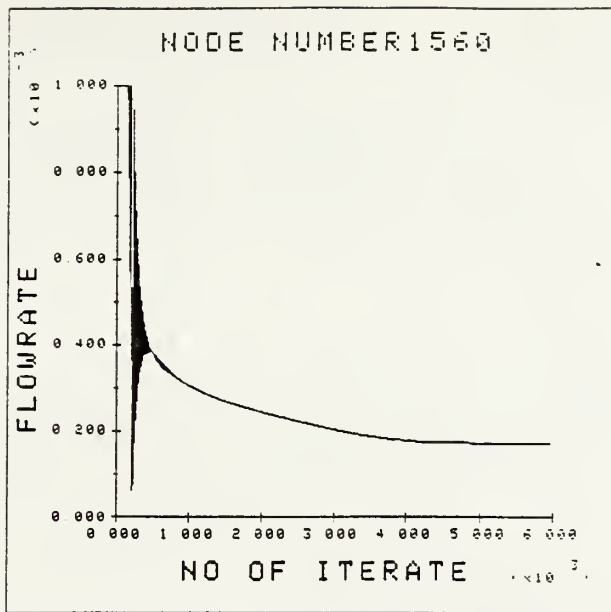


Figure 5.24(a): Input flowrate of application problem four

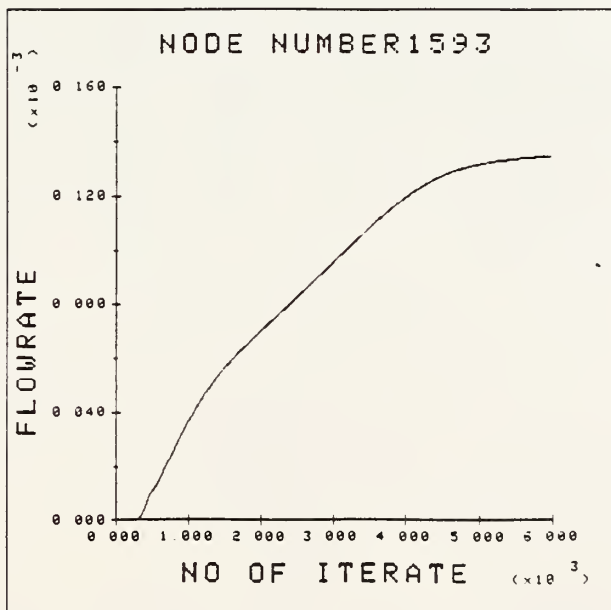


Figure 5.24(b): Output flowrate of application problem four

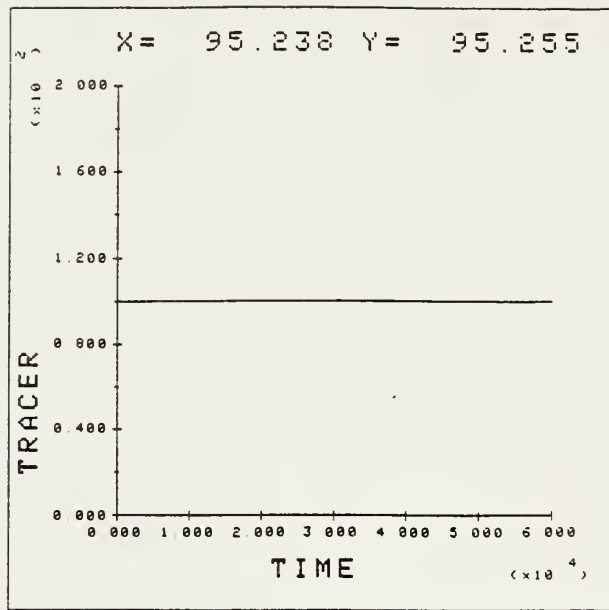


Figure 5.25(a): Tracer at input node (problem four)

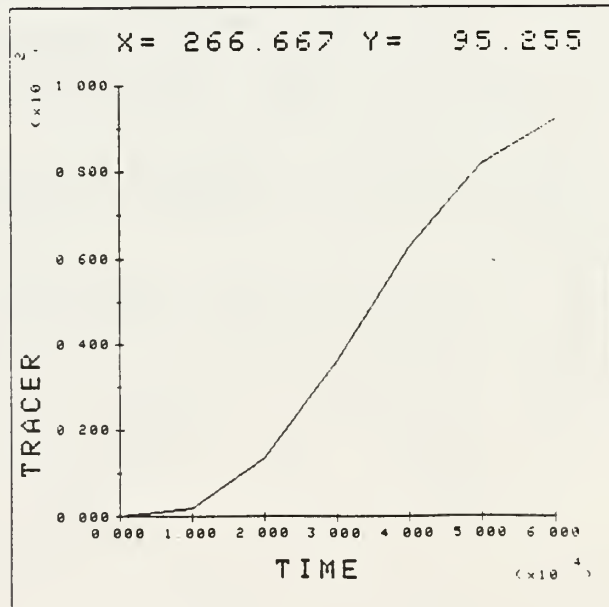


Figure 5.25(b): Tracer at middle of crack (problem four)

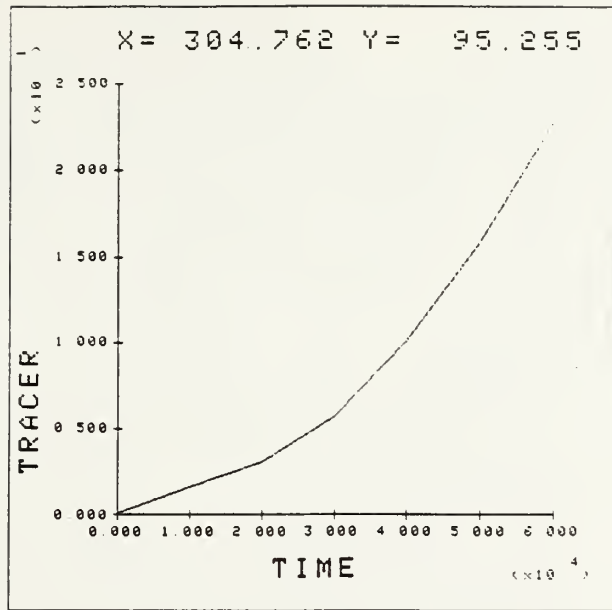


Figure 5.25(c): Tracer at output place (problem four)

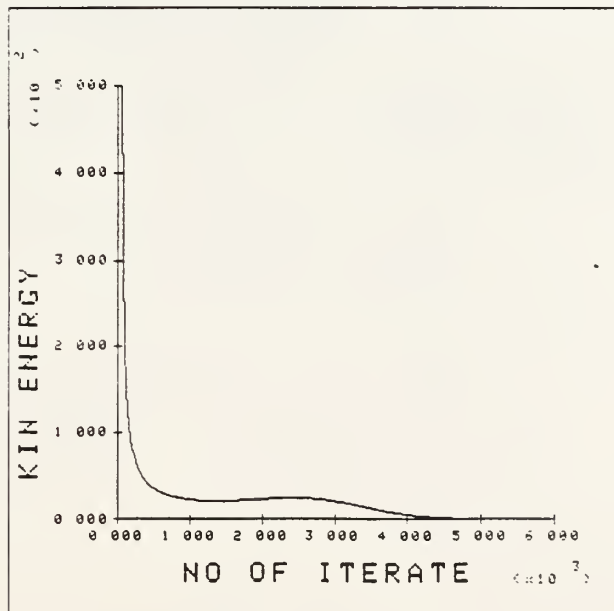


Figure 5.26: Kinetic energy vs No of iteration plot

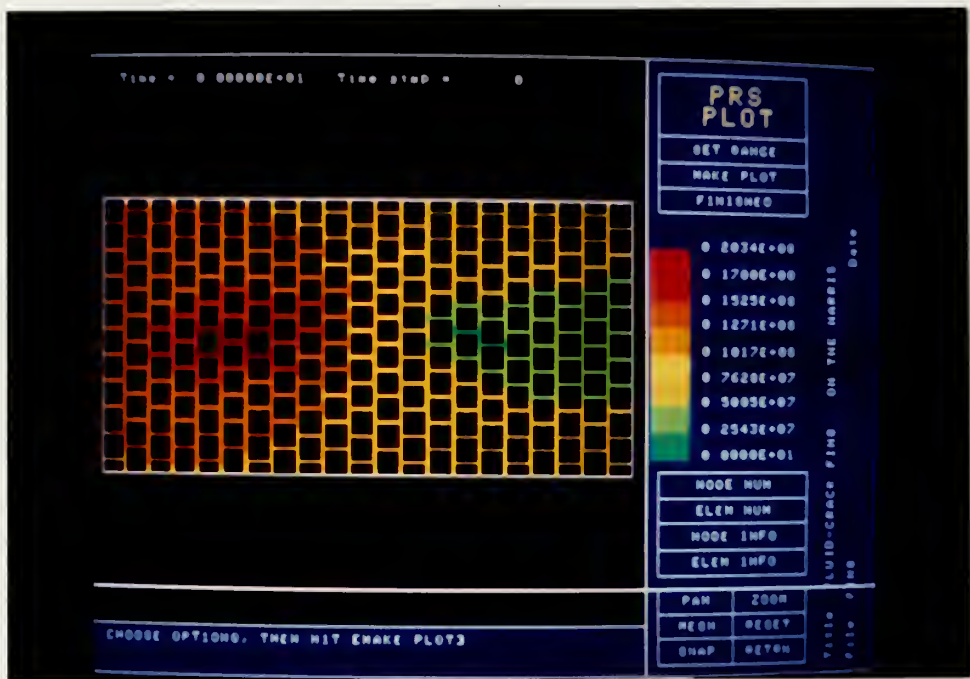


Figure 5.27: Pressure plot of application problem four

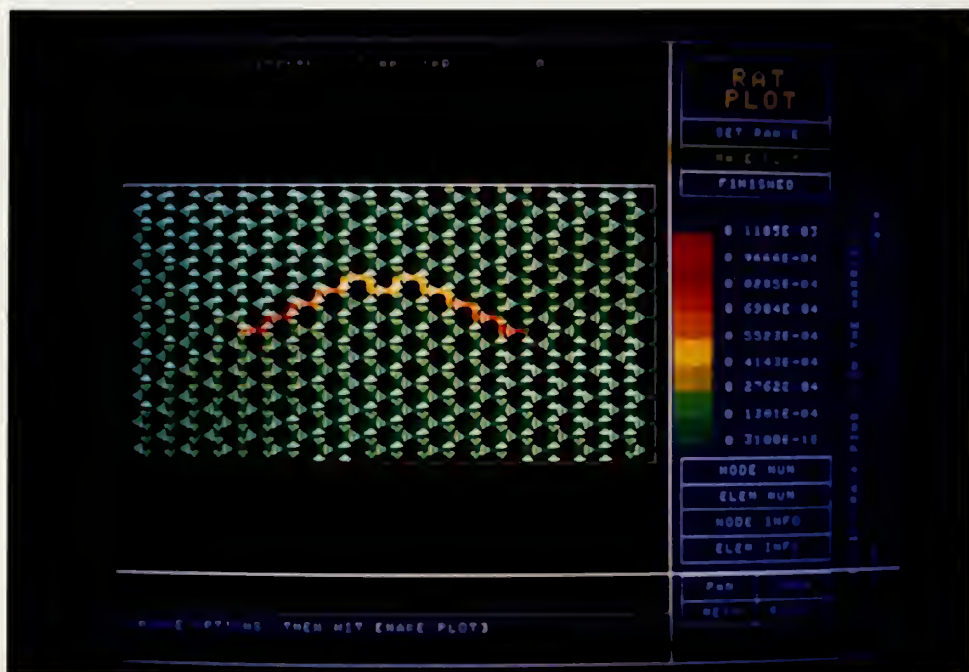


Figure 5.28: Flowrate plot of application problem four

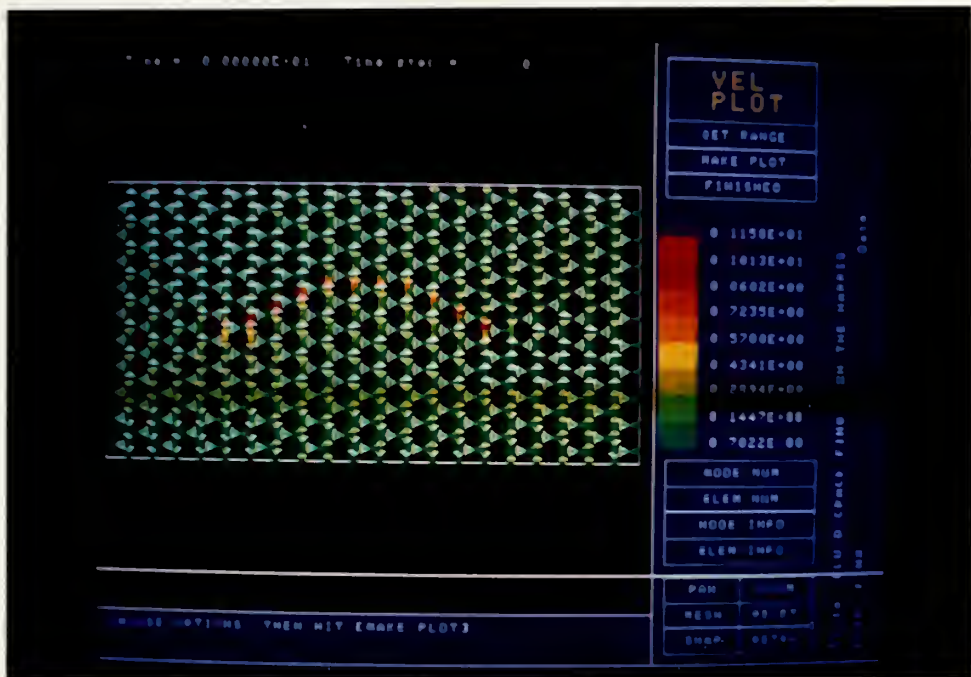


Figure 5.29: Velocity plot of application problem four

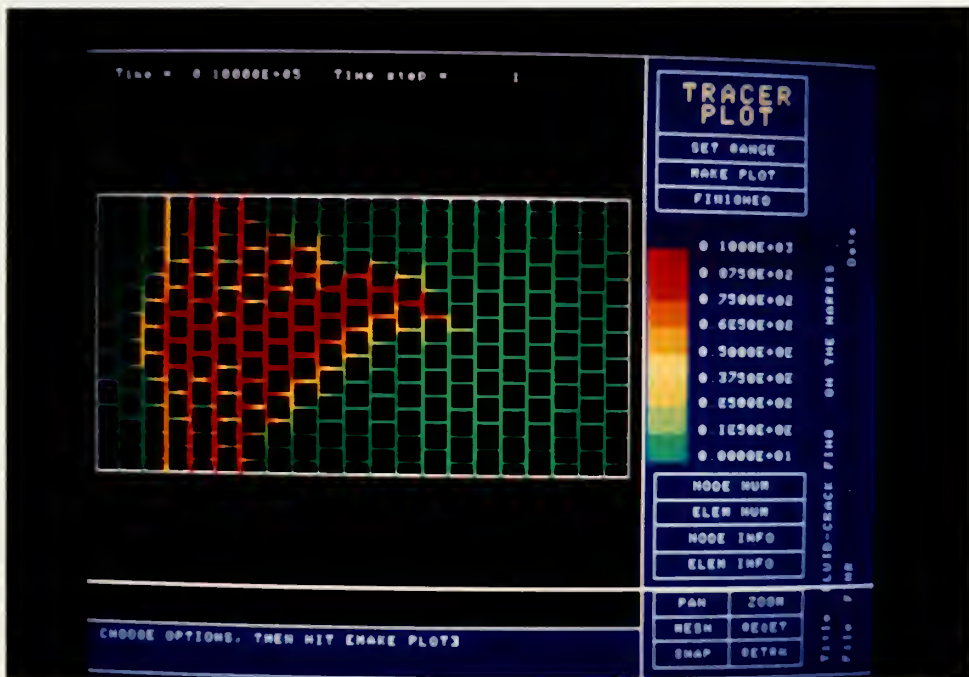


Figure 5.30(a): Tracer plot at 1×10^4 seconds

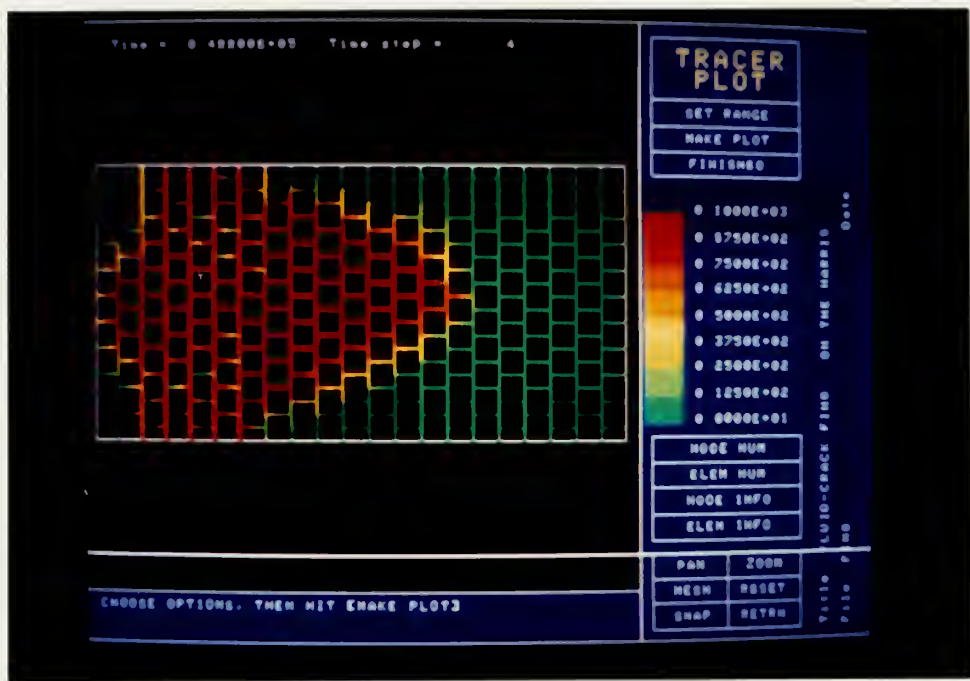


Figure 5.30(b): Tracer plot at 4×10^4 seconds

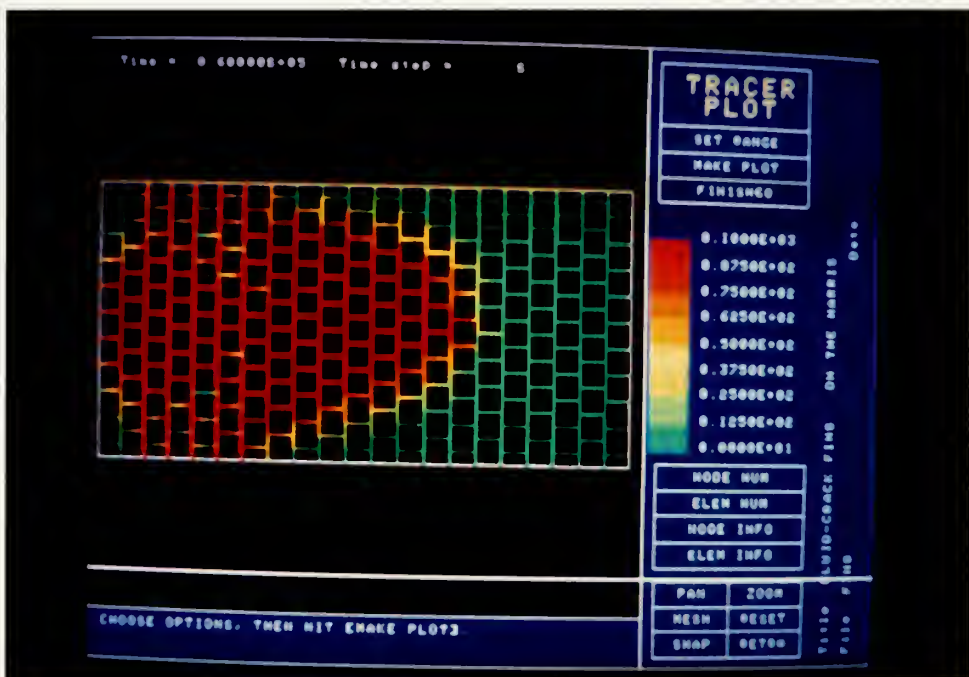


Figure 5.30(c): Tracer plot at 6×10^4 seconds

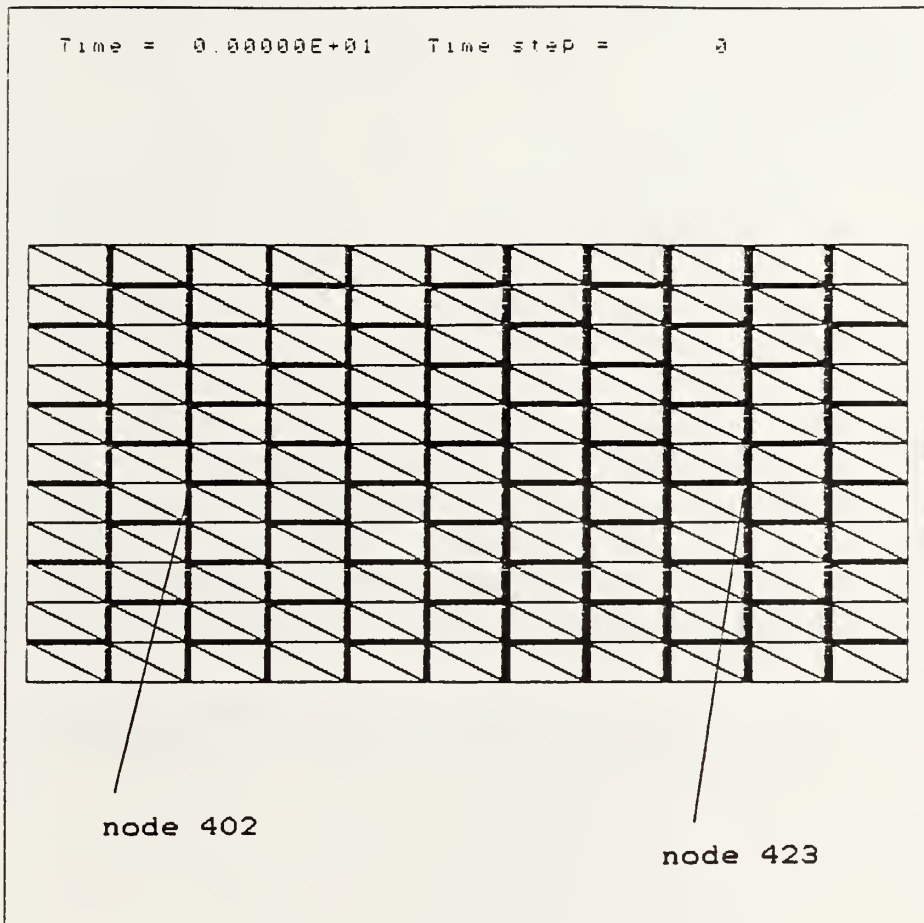


Figure 5.31: Application problem five

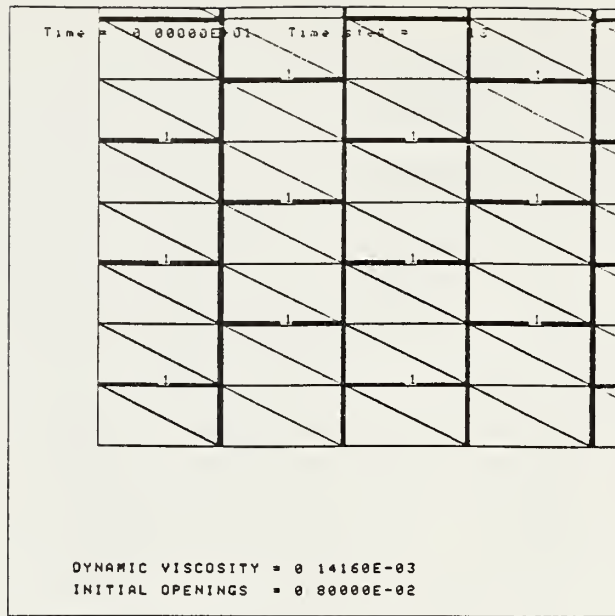


Figure 5.32(a): Material property of material type one

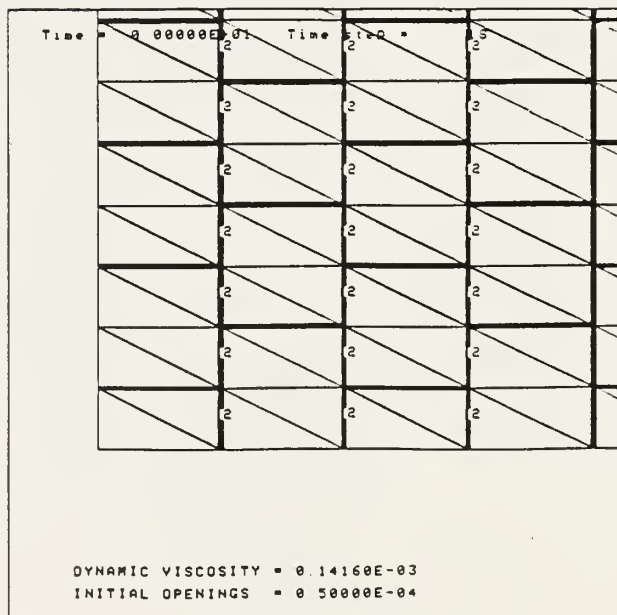


Figure 5.32(b): Material property of material type two

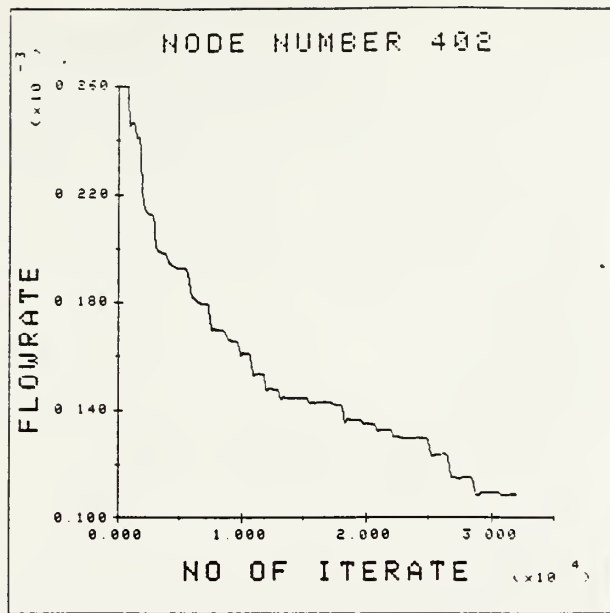


Figure 5.33(a): Input flowrate of application problem five

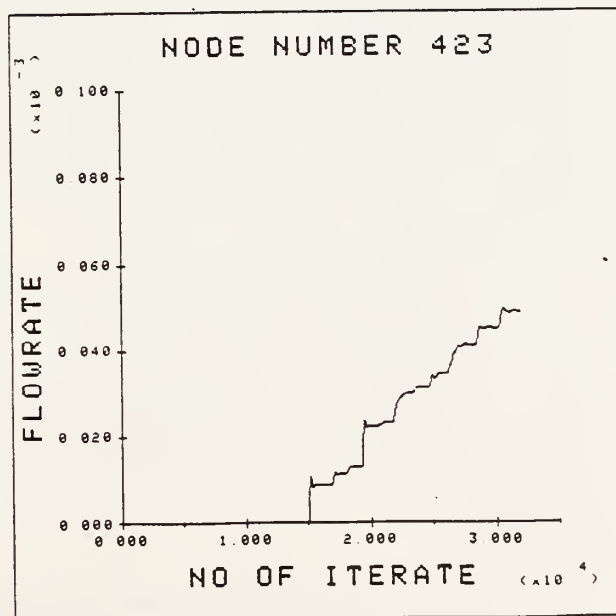


Figure 5.33(b): Output flowrate of application problem five

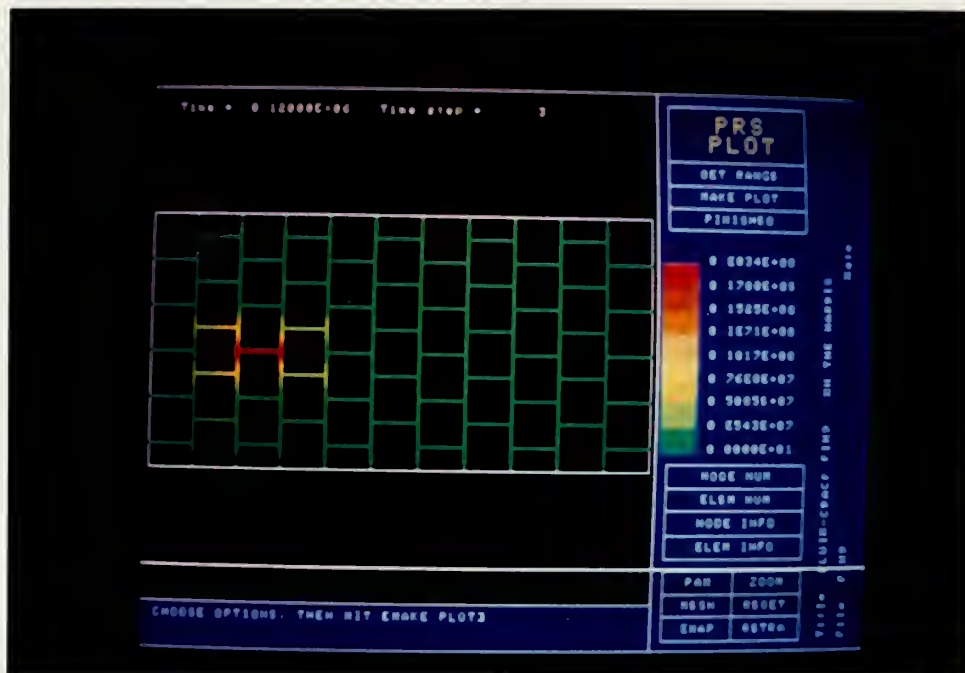


Figure 5.34(a): Pressure plot at 4×10^4 seconds



Figure 5.34(b): Flowrate plot at 4×10^4 seconds

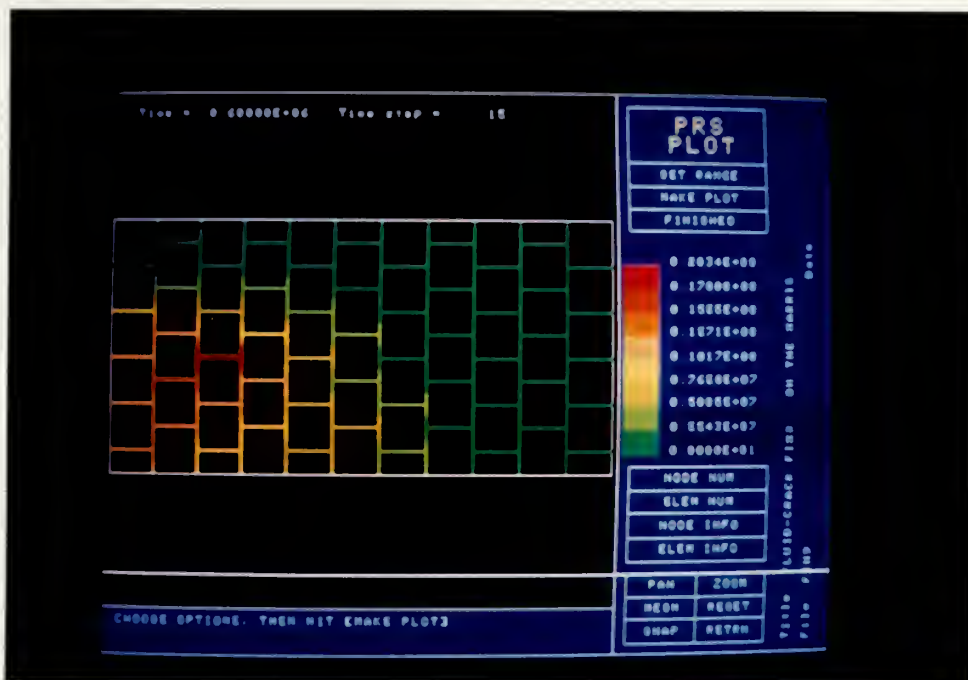


Figure 5.35(a): Pressure plot at 6×10^5 seconds

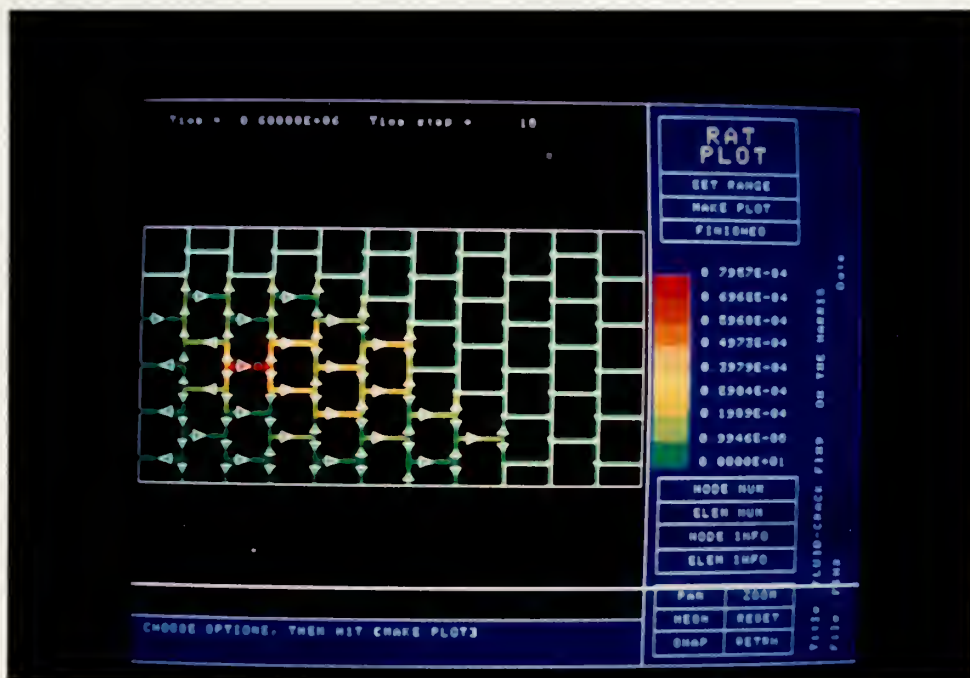


Figure 5.35(b): Flowrate plot at 6×10^5 seconds



Figure 5.36(a): Pressure plot at 1.2×10^7 seconds

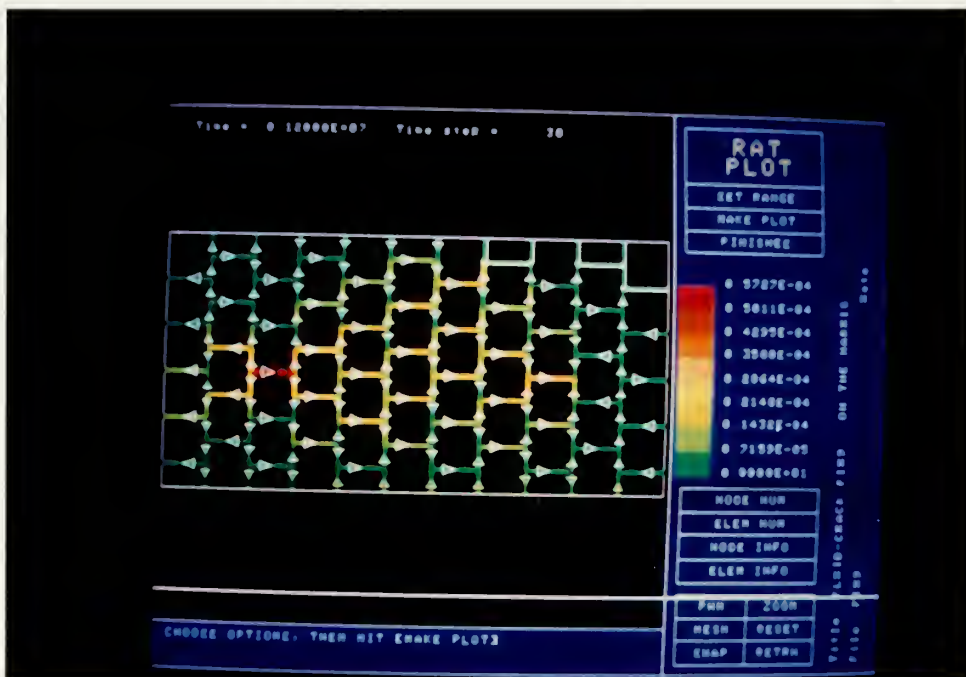


Figure 5.36(b): Flowrate plot at 1.2×10^7 seconds

CHAPTER VI

CONCLUSIONS

In this thesis, we have developed a finite element model of fluid flow in fractured rock. The flow paths in the rock are modeled discretely using one dimensional finite elements combined in a network. Special features include the capability to model the filling of empty joints, simulate far field leakage using a nonlinear pressure/flowrate relation, and model the injection of a tracer and its distribution through the system. Interactive computer graphics allows the user to easily specify the problem and review the results. Dynamic relaxation is used to obtain a solution. This robust scheme will be used when the fluid model is coupled to a deformable rock model and the solution becomes nonlinear.

The verification examples presented in chapter IV are idealistic. They demonstrate most features of the model.

The application problems show the pressure and fluid flowrate distributions for fluid being pumped in one well at high pressure and removed from another well at low pressure. Application problems one, two, and three show the significance of the far field boundary conditions. Significant leakage occurs if the zero pressure condition is specified.

In problem four we examined the effect of a lower resistance bridge between the input and output wells. This is an attempt to simulate a more realistic situation, where there is a dominant flow path between wells in addition to many other flow paths. Flow did

indeed follow the lower resistance path, as shown by both the flowrate and tracer calculations. The tracer signal was received at the output much sooner. Smoothing of the signal occurs both because of dilution with water in the fractures and due to mixing from the different flow paths.

In problem five we demonstrated the filling of open joints. The analysis showed the progressive filling and activation of elements between the input and output.

All the application calculations were approximate solutions in support of the Hot Dry Rock geothermal energy project. The accuracy of prediction depends largely upon the amount of correct geological information available. The controlling factor of fluid flow is the magnitude of the aperture, and since flowrate depends on $(a)^3$, a slight change in aperture can easily dominate any other change in the geometry of the flow field. In general the information such as fracture aperture, wall roughness and far field conditions are little known.

The finite element model developed in this study is quite versatile, and can be coupled to the deformation of the rock blocks easily. This coupled code will make it possible to predict the manner in which joint openings change during Hot Dry Rock experiments. After coupling the fluid and structural models, the next step will be to couple heat transfer to the solution. The final model will aid the engineer in developing a clearer picture of flow behavior in the HDR reservoir.

References

Brown, Don, 1988, Los Alamos National Laboratory, New Mexico, personal communication.

Brown, Stephen R., 1987, "Fluid Flow through Rock Joints: The effect of surface roughness," Journal of Geophysical Research Vol. 92, No. B2, pp. 1337-1347.

Day, A.S., 1965, "An introduction to dynamic relaxation," Engineer, Vol. 219, pp. 218-221.

Franke, Paul R., Nunz, Gregory J., 1985, "Recent developments in the Hot Dry Rock geothermal energy program," Los Alamos National Laboratory, Geothermal Resources Council Annual Meeting, Kailua-Kona, Hawaii.

Frieze, P.A., Hobbs, R.E. and Dowling, P.J., 1978, "Application of dynamic relaxation to the large-deflection elasto-plastic analysis of plates," Compu. Struct., Vol. 8, pp. 301-310.

Haar, Lester, Gallagher, John S. and Kell, George S., 1984, "Steam Tables," McGraw-Hill Inter. Book Co.

Hilber, Hans M. and Taylor, Robert L., 1976, "A Finite Element Model of fluid flow in systems of Deformable Fractured Rock," Department of Civil Engineering, Division of Structural Engineering and Structural Mechanics, University of California, Berkeley, California.

de Josselin de Jong, G., 1972 "Dispersion of a point injection in an anisotropic porous medium," unpublished report, New Mexico Tech, pp. 68.

Los Alamos National Laboratory, 1984, "Hot Dry Rock Geothermal Energy Development Program," Annual Report, LA-10661-HDR.

Los Alamos National Laboratory, 1985, "HOT DRY ROCK Geothermal Energy Development Program," Annual Report, LA-11101-HDR.

Louis, C., 1969, "A study of groundwater flow in jointed rock and its influence on the stability of rock masses," Imperial college Rock Mechanics Research Report No. 10.

Noorishad, J., Ayatollahi, M.S., Witherspoon, P.A., 1982, "A Finite-Element Method for Coupled Stress and Fluid Flow Analysis in Fractured Rock Masses," Int. J. Rock Mech. Min. Sci. & Geomech. Abstr. VOL. 19, pp. 185-193.

Palen, Walter A. and Narasimhan, T. N., 1981, "The roles of pore pressure and fluid flow in the hydraulic fracture process," Lawrence Berkeley Laboratory, University of California, Berkeley.

Papadrakakis, M., 1981, "A Method for The Automatic Evaluation of The Dynamic Relaxation Parameters," Computer Method in Applied Mechanics and Engineering, Vol. 25, pp. 35-48.

Pica, A. and Hinton, E., 1980, "Transient and pseudo-transient analysis of Mindlin plates," Int. J. Num. Meth. Eng., Vol. 15, pp. 189-208.

Ryan, Thomas M. and Farmer, Ian W., 1987, "Laboratory determination of fracture permeability," 28th US Symposium on Rock Mechanics, Tucson.

Schwartz', Franklin W. and Smith, Leslie, 1988, "A Continuum Approach For Modeling Mass Transport in Fractured Media," Water Resources Research, March, 1988.

Segerlind, Larry J., 1984, "Applied Finite Element Analysis," P. 27, Second Edition, John Wiley & Sons Co.

Snow, D.T., 1965, "A parallel plate model of fractured permeable media," Ph.D. thesis, University of California, Berkeley, California.

Strang, G., 1976, "Linear Algebra and Its Applications," Academic Press, New York.

Sundaram, P. N., Watkins, D. J., Ralph, W. E., 1987, "Laboratory investigations of coupled stress-deformation-hydraulic flow in a natural rock fracture," 28th US Symposium on Rock Mechanics, Tucson.

Swenson, D. V., 1985, "Modeling Mixed-Mode Crack Propagation Using Finite Elements," Dept. of Structural Engineering Report, Number 85-10, Cornell University, Ithaca, NY.

Underwood, Philip, 1983, "Computational Methods for transient Analysis," Elsevier Science Publishers B. V., pp. 245-265

Wilson, Charles Richard, 1970, "An investigation of laminar flow in fractured porous rocks," Ph.D. dissertation, University of California, Berkeley.

Wilson, C.R. and Witherspoon, P.A., 1970, "An investigation of laminar flow in fractured rocks," Geotechnical report No. 70-6, University of California, Berkeley.

Witherspoon, P.A., Wang, J.S.T., Iwai, K., Gale, J.E., 1980, "Validity of the cubic law for fluid flow in a deformable rock fracture," Water Resources Research, VOL. 16, NO. 6.

99

A FINITE ELEMENT METHOD SOLUTION
FOR FLUID FLOW IN JOINTED ROCK

BY

Shun-Lung Su

B.S., Chun-Yuan University

Taiwan R.O.C., 1983

AN ABSTRACT OF A THESIS

submitted in partial fulfillment of the
requirements for the degree

MASTER OF SCIENCE

Department of Mechanical Engineering

KANSAS STATE UNIVERSITY

Manhattan, Kansas

1988

ABSTRACT

In this thesis, we develop a finite element model of flow in fractured rock masses. The joints are modeled discretely using one dimensional finite elements connected in a network. Because of the robust solution scheme, complicated nonlinear joint networks can be solved. The model includes the filling of empty joints as fluid is pumped through the fracture network. If a joint is not filled, the pressure in the joint is assumed zero and the net flow into the joint is calculated. When a joint fills, the element becomes active and is included in the flow calculation. Far field leakage is simulated using a nonlinear pressure-flowrate relation. The user can also specify arbitrary tracer input and monitor the distribution of the tracer during an analysis.

Example calculations include solutions in support of the Hot Dry Rock geothermal energy project. The solutions show the pressure and fluid velocity distributions for fluid being pumped in one well at high pressure and removed from another well at low pressure. A comparison of solutions with uniform and nonuniform joint openings shows how the fluid follows the low resistance path and how the tracer output signal is smoothed as a result of the different flow path arrival times. The results of this model will aid engineers of Los Alamos to understand more about fluid motion in the Hot Dry Rock reservoir.

